CONCURRENT OPERATION OF WIRELESS POWER TRANSFER BASED CONTACTLESS SLIP RING AND MOTOR DRIVE SYSTEM WITH A SINGLE CONVERTER

A THESIS SUBMITTED TO
THE GRADUATE SCHOOL OF NATURAL AND APPLIED SCIENCES
OF
MIDDLE EAST TECHNICAL UNIVERSITY

BY

ENES AYAZ

IN PARTIAL FULFILLMENT OF THE REQUIREMENTS
FOR
THE DEGREE OF MASTER OF SCIENCE
IN
ELECTRICAL AND ELECTRONICS ENGINEERING

SEPTEMBER 2022

Approval of the thesis:

CONCURRENT OPERATION OF WIRELESS POWER TRANSFER BASED CONTACTLESS SLIP RING AND MOTOR DRIVE SYSTEM WITH A SINGLE CONVERTER

submitted by **ENES AYAZ** in partial fulfillment of the requirements for the degree of **Master of Science in Electrical and Electronics Engineering Department, Middle East Technical University** by,

Prof. Dr. Halil Kalıpçılar
Dean, Graduate School of **Natural and Applied Sciences** _____

Prof. Dr. İlkay Ulusoy
Head of Department, **Electrical and Electronics Engineering** _____

Assoc. Prof. Dr. Ozan Keysan
Supervisor, **Electrical and Electronics Engineering, METU** _____

Examining Committee Members:

Assist. Prof. Dr. Emine Bostancı Özkan
Electrical and Electronics Engineering, METU _____

Assoc. Prof. Dr. Ozan Keysan
Electrical and Electronics Engineering, METU _____

Prof. Dr. Muammer Ermiş
Electrical and Electronics Engineering, METU _____

Assoc. Prof. Dr. Mustafa Mert Ankaralı
Electrical and Electronics Engineering, METU _____

Prof. Dr. Bünyamin Tamyürek
Electrical and Electronics Engineering, Gazi University _____

Date: 02.09.2022

I hereby declare that all information in this document has been obtained and presented in accordance with academic rules and ethical conduct. I also declare that, as required by these rules and conduct, I have fully cited and referenced all material and results that are not original to this work.

Name, Surname: Enes Ayaz

Signature :

ABSTRACT

CONCURRENT OPERATION OF WIRELESS POWER TRANSFER BASED CONTACTLESS SLIP RING AND MOTOR DRIVE SYSTEM WITH A SINGLE CONVERTER

Ayaz, Enes
M.S., Department of Electrical and Electronics Engineering
Supervisor: Assoc. Prof. Dr. Ozan Keysan

September 2022, 125 pages

This thesis presents a novel approach for concurrent power transfer to wired and wireless systems using a single inverter. This proposed approach fits a cost-effective solution to wireless power transfer (WPT) systems used in contactless slip rings (CSR) applications such as sensors, radars, or wind-turbine pitch controls. In conventional systems, there are two separate converters: one is for the motor drive, and the other is for the WPT system. It is proposed that the switching harmonics of the motor drive can also be utilized to excite the WPT system while the low-frequency component can still be used to drive the motor. Thus, the converter of WPT systems is eliminated. In the past, however, conventional Si-based motor drives allow switching frequencies below 20 kHz, making the WPT system bulky. Nowadays, with the development of wide-bandgap devices, the switching frequency has considerably increased up to 100 kHz, making the proposed system a feasible size. However, the independent control of switching and low-frequency components is challenging while utilizing the conventional motor driving PWM techniques. In this study, novel concurrent operation methods are developed. In DC motor drives, the bipolar-PWM with the proposed frequency/duty cycle control is analyzed mathematically, and it is experi-

mentally verified with a series-series (SS) WPT system and a DC motor driven by a GaN-based full-bridge (FB) converter. In AC motor drives, SPWM with the proposed carrier-phase-shift / modulation index control is analyzed mathematically. Firstly, the concurrent operation of the induction motor (IM) and an SS-WPT system for rotating electronic loads is experimentally verified with a GaN-based inverter. Secondly, the field winding of the wound-field synchronous motor is excited by the proposed method. In order to achieve light-weight on the rotor side, a series-none (SN) WPT system is used, and varying carrier-phase-shift is used to reduce the output capacitance.

Keywords: Wireless power transfer, inductive power transfer, motor drive, slip rings, rotating systems, concurrent power transfer, dual-band power transfer, carrier phase shift, field excitation, EVs, wind turbine.

ÖZ

KABLOSUZ GÜÇ AKTARIM TABANLI TEMASSIZ KAYMA HALKASI VE MOTOR SÜRÜCÜ SİSTEMİNİN TEK BİR DÖNÜTÜRÜCÜ İLE EŞ ZAMANLI ÇALIŞMASI

Ayaz, Enes
Yüksek Lisans, Elektrik ve Elektronik Mühendislii Bölümü
Tez Yöneticisi: Doç. Dr. Ozan Keysan

Eylül 2022 , 125 sayfa

Bu tez, tek bir evirici kullanarak kablolu ve kablosuz sistemlere eşzamanlı güç aktarımı için yeni bir yaklaşım sunmaktadır. Önerilen bu yaklaşım, sensor, radar veya rüzgâr türbini hatve kontrolü gibi uygulamalarda kullanılan temassız kayma halkalarının (TKH) kablosuz güç aktarım (KGA) sistemlerine uygun maliyetli bir çözüm sunar. Geleneksel sistemlerde iki ayrı dönüştürücü vardır: biri motor sürücüsü için, diğeri KGA sistemi içindir. Motor sürücüsünün düşük frekanslı bileşenin hala motoru sürmek için kullanırken, anahtarlama harmoniklerinin ise KGA sistemini harekete geçirmek için kullanılabileceği önerilmektedir. Böylece, KGA sistemlerinin dönüştürücüsü ortadan kalkar. Ancak geçmişte, Si-tabanlı geleneksel motor sürücüler 20kHz'in altında anahtarlama frekanslarına kadar izin verdikleri için KGA sistemlerinin boyutları büyük oluyordu. Günümüzde geniş bant aralıklı cihazların geliştirilmesi ile, anahtarlama frekansı 100kHz'e kadar önemli ölçüde artmış ve önerilen sistem uygulanabilir hale gelmiştir. Ancak, anahtarlama bileşeninin bağımsız kontrolü, geleneksel darbeli genişlik modülasyon (DGA) tekniklerini kullanırken zordur.

Bu çalışmada, yeni eş zamanlı operasyon yöntemleri geliştirilmiştir. DC motor sürücülerinde, önerilen frekans/görev çevrimi yöntemi kullanılan çift kutuplu-DGA matematiksel olarak analiz edilir ve yöntem, bir GaN tabanlı tam köprü (TK) dönüştürücü tarafından sürülen bir seri seri (SS) KGA sistemi ile deneysel olarak doğrulanır. AC motor sürücülerinde önerilen taşıyıcı-faz-kayması/modülasyon indeksi yönteminin uygulandığı sinüzoidal-DGA analiz edilmiştir. İlk olarak, asenkron motor (AM) ve bir SS-KGA sisteminin eşzamanlı çalışması, GaN tabanlı bir evirici ile deneysel olarak doğrulanmıştır. İkinci olarak, önerilen sistem, bir senkron makinenin alan sargısının ikazında kullanılır. Rotor tarafında hafiflik elde etmek için bir seri-hiç (SH) KGA sistemi kullanılır ve çıkış kapasitansını azaltmak için değişken taşıyıcı-faz kayması yöntemi kullanılır.

Anahtar Kelimeler: Kablosuz güç aktarımı, endüktif güç aktarımı, motor sürücü, kayma halkaları, dönen sistemler, ezamanlı güç aktarımı, çift-bant güç aktarımı, taşıyıcı faz kayması, alan ikazı, elektrikli araçlar, rüzgar türbini

"Twice two makes four without my will. As if free will meant that! "

Fyodor Dostoevsky

ACKNOWLEDGMENTS

This thesis is dedicated to the people who assist and support me.

Firstly, working under the technical guidance of Dr. Ozan Keysan is an honor for me. He has always been optimistic and could provide motivation to me even in challenging times. The thesis would be impossible without him.

Secondly, I will present eternal thanks for Nail Tosun. He always widened my horizon with his logical and absurd ideas. He is a teacher like Feynman for me, a colleague, a friend, and a family. Moreover, I present unconditional love to our cat, as known as "The Kedi". Without Nail and The Kedi, I could not have overcome difficulties even if these difficulties sometimes stem from them.

Thirdly, I would also like to thank my project partners, Ogün Altun, and Hakan Polat, for their effort and endless support during this thesis. They have considerable contributions to every part of my thesis. They always had amazing ideas to develop new things. Without them, this study would be incomplete. Moreover, I would like to thank Özgür Gülsuna, who always comes up with new ideas. He taught me to work interdisciplinary.

Fourthly, I would like to thank everyone on METU PowerLab. We have a team soul, and they are good friends and colleagues. I believe in everyone will have great success in their life, and it was a great opportunity to work with these precious people.

I am also thankful to TÜBİTAK, the Scientific and Technological Research Council of Turkey, for granting me their M.S. studies scholarship, BİDEB 2210.

Finally and most importantly, I would like to thank my family, who were always there for me in every part of my life. Without them, no thesis is worth finishing.

TABLE OF CONTENTS

APPENDICES

LIST OF TABLES

TABLES

LIST OF FIGURES

FIGURES

CHAPTER 1

INTRODUCTION

Power transfer to rotating frames is required in many industrial applications, such as energizing rotating auxiliary loads (used in spindle motors, radar systems, or sensors) or field excitation of the synchronous motors (used in wind-turbine pitch controls or electric vehicles' traction systems) [7, 8, 9, 10]. However, using direct contact via a wire is not applicable due to the cable entanglement, so revealing a challenge. Industry and literature declare several solutions to this challenge. The first solution is to use slip rings (SRs), made up of conductor rings and carbon brushes rubbed with these rings, as shown in Fig. 1.1.

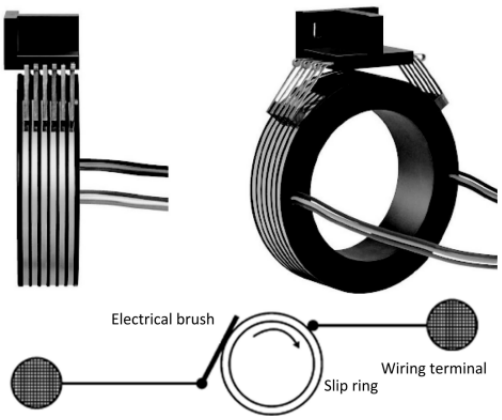

Figure 1.1: A conventional slip ring [1].

Although they are simple, cost-effective, and efficient, they require regular maintenance and have reliability issues due to the mechanical friction causing physical wear [11]. Another solution is to use brushless exciters (BEs), which are synchronous generators with rotating rectifiers, as shown in Fig. 1.2.

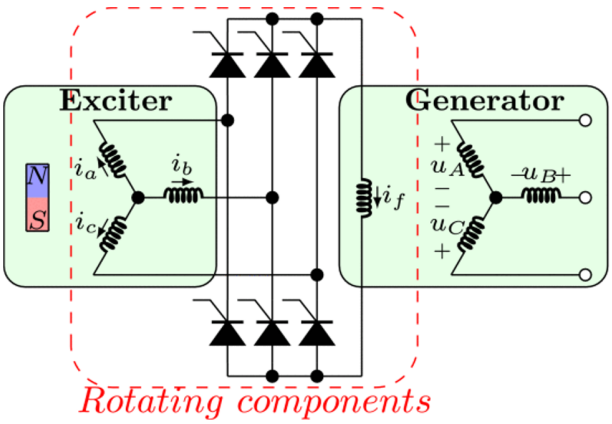

Figure 1.2: A circuit representation of brushless exciter [2].

However, BEs power transfer capability decreases as the speed gets lower. Thus, they are suitable for only constant speed applications such as field excitation of large synchronous generators. Alternative to SRs and BEs, contactless slip rings (CSR) based on wireless power transfer (WPT) systems, which are shown in Fig. 1.3, have become prominent since they provide higher reliability and maintenance-free system. They give flexible transfer distance and higher efficiency. However, they are not cost-effective and simple to employ. Moreover, WPT systems reveal electromagnetic compatibility and interference (EMC/EMI) issues due to leakage of the electromagnetic field. However, the leakage can be minimized, and the effect on the other devices can be restricted by flux guides (via ferrite strips) or magnetic isolations (via aluminum shields). Table 1.1 presents the comparison between these three methods.

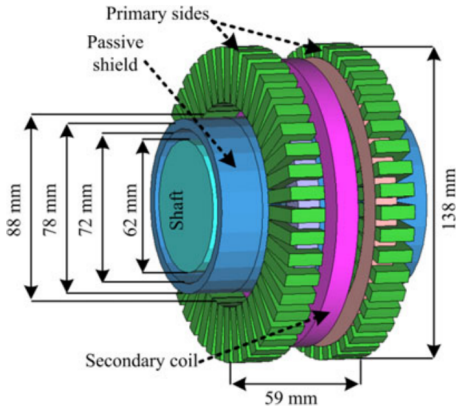

Figure 1.3: An example of contactless slip ring [3].

Table 1.1: Comparison of The Systems Transferring Power to Rotating Frames

	Slip Rings	**Brushless Exciters**	**Contactless Slip Rings**
Reliability	-[12]	+[8]	+
Maintenance	- -[13]	+	+
Simplicity	+	+	- -
Speed Independency	+	- -	+
Cost-Effectivity	+	+	- -
Efficiency	+	- -	+
EMC/EMI	+	+	-

To sum up, slip rings are slightly unreliable and require regular maintenance, which increases the operation cost. Brushless exciters solve these problems, so they are reliable and maintenance-free. However, their efficiency is worse than slip rings, and their power transfer depends on the rotation speed. Besides, they increase the weight and volume of the overall system, which can be critical in some applications such as spindle motors. Moreover, extra inductance and resistance of the BEs create a lag to control, which is significant for some applications such as field excitation. WPT-based CSRs are superior performance properties compared to SRs and BEs, but they are expensive and complex due to the requirement of active converters and controller units. Besides, they can require flux guides or magnetic isolations to avoid EMC/EMI issues.

1.1 Review of Wireless Power Transfer Systems

The wireless power transfer (WPT) system was first revealed in 1886 by the Hertz experiment, generating and harvesting electromagnetic microwaves. Then, Nikola Tesla invented an inductive power transfer (IPT) system where the circuit diagram is shown in Fig. 1.4.

The system works like a step-up transformer that generates high voltage output. The spark gap is used to create high-frequency pulsating voltage; then, the voltage is

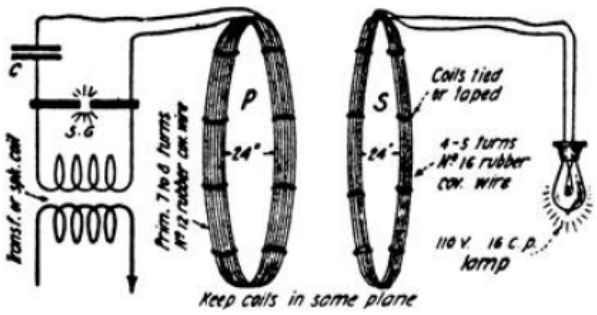

Figure 1.4: Tesla's wireless power transfer system [4].

filtered by a series capacitor. Thus, high-frequency high-voltage power is transferred wireless by coupled coils.

WPT technologies have been stagnant due to their lower efficiencies and high-frequency requirements that have made them unfeasible in the past. After a long time, WPT systems have been popular again thanks to the development of high-power, high-frequency semiconductor devices and the increase in computational power of micro-controllers. MIT researchers conducted the first study, showing that 60 W power could be transmitted over 2 meters using the same working principles as Nikola Tesla proposed [14]. Numerous studies have been performed in many applications such as biomedical, EV, and energy harvesting thanks to their advantages, such as a space-free and cordless system operating in harsh environments like dusty and moist [15, 16, 17, 18]. Although there are different WPT methods, such as capacitive power transfer (CPT), WPT in radio frequency (RF), and WPT in ultrasound, the most common method is inductive power transfer (IPT), which provides a higher power with a flexible range of transfer distance and high-efficiency [19]. The comparison between these methods is presented in Table 1.2.

Table 1.2: Comparison of WPT Methods

	Inductive Power Transfer	**Capacitive Power Transfer**	**WPT in Radio Frequecy**
Transfer Type	Varying MF	Varying EF	Varying EF & MF
Power ratings	+	-	-
Frequencies	-	+	+
Efficiency	+	+	-
Distance	+	-	+

MF : Magnetic field, EF : Electric field.

IPT systems generally consist of DC-AC converters, compensation circuits, transmitter (Tx) and receiver (Rx) coils, and AC-DC rectifiers. The block diagram of a simple IPT system is shown in Fig. 1.5.

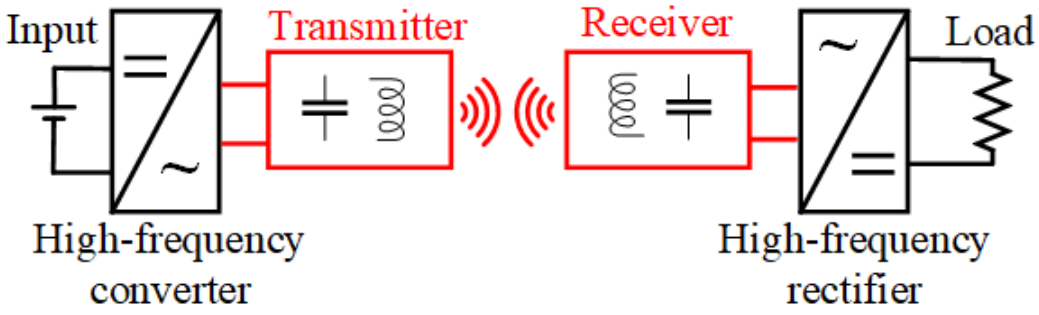

Figure 1.5: The general block diagram of WPT systems.

1.2 The Proposed System and Motivation

WPT-based CSRs have been in place of conventional slip rings[20, 21, 22, 23, 24, 25] thanks to their advantages mentioned before. They are used in many industrial applications such as radar, sealing rollers, and field excitations. The common trait of these applications is that they have a motor drive system, as shown in Fig. 1.6, which rotates the load.

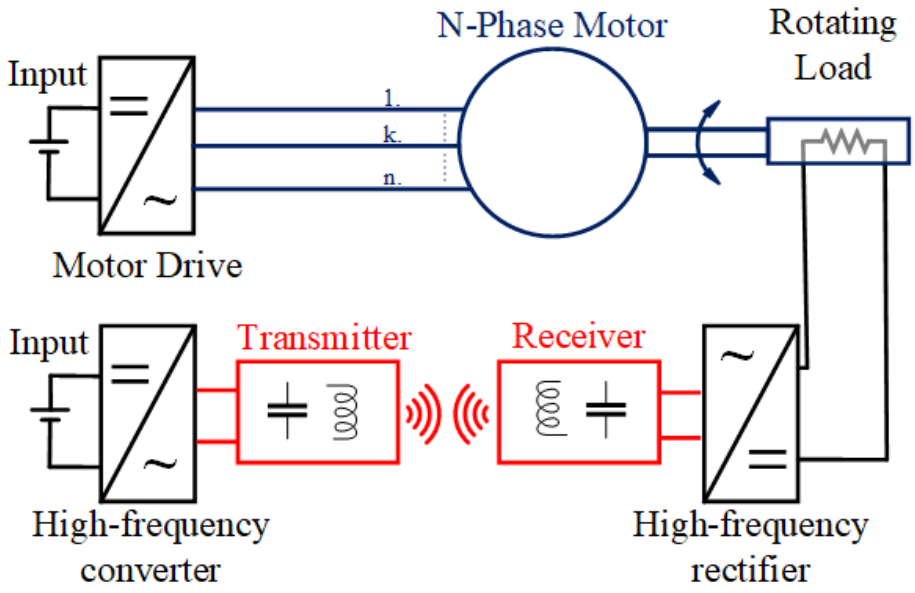

Figure 1.6: The representation of a conventional WPT-based CSR system.

Conventional systems consist of two separate converters: one to drive the motor and one to excite the Tx coil. The CSR systems increase reliability and efficiency and decrease maintenance requirements compared to their competitor but increase cost and complexity due to this high-frequency converter. In these systems, already existing motor drive generates high-frequency switching voltage harmonics, but motor winding filters out these high-frequency components, so these harmonics attenuate in motor currents. In the proposed system, the Tx coil utilizes these high-frequency voltage harmonics to transfer power to the Rx coil, while the low-frequency currents can still be used to generate torque in the motor. Thus, a separate WPT converter is no longer required, and the motor drives can be used without increasing the power ratings since the WPT system's power ratings are smaller than the motor drive system.

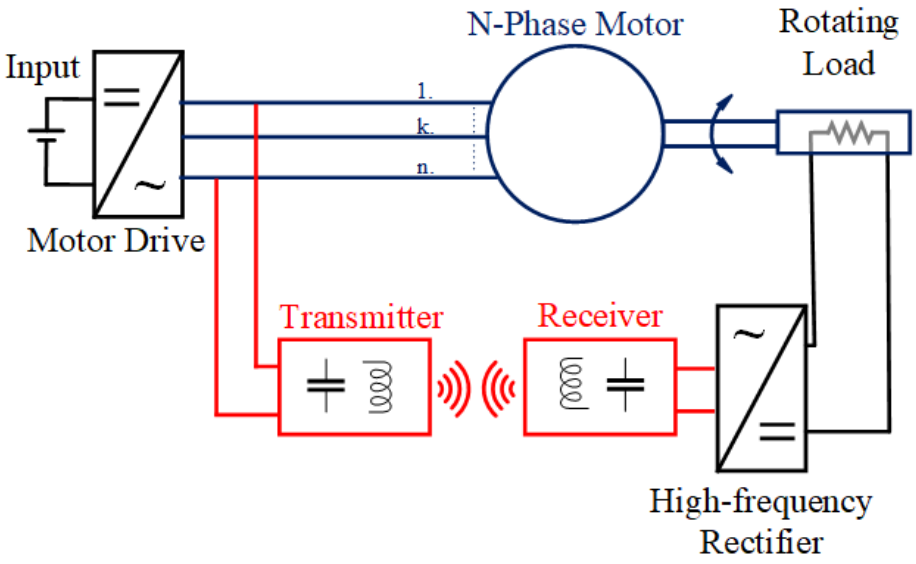

Figure 1.7: The block diagram of the proposed WPT-based CSR system.

The proposed system is represented in Fig. 1.7. The advantages and disadvantages are discussed in Table 1.3. The proposed system meets the requirements and solves the complexity and cost problems of the conventional systems that use two converters: One for the motor driver and one for the WPT system. Furthermore, eliminating one of the converters increases reliability and decreases the maintenance requirements.

Table 1.3: Comparison of Various Systems Transferring Power to Rotating Frames

	Conventional CSR Systems	**The Proposed CSR System**
Reliability	+	+*
Maintenance	+	+*
Simplicity	-	+
Cost Effective	-	+
Efficiency	+	+

* introduces an additional small advantage.

1.3 Research Motivation

This thesis aims to design a simple and cost-efficient contactless slip ring based on a wireless power transfer system, which can be directly implemented with conventional motor drives. Either the proposed system fits to energize rotating auxiliary loads such as sensors, radars, and IoT devices, or it can be utilized to excite the field windings of synchronous motors such that used in pitch control of wind turbines or EV applications. Unlike conventional WPT-based CSRs, excitation of Tx coil varies with motor operations since they use the same converter concurrently. Therefore, the design and control of the proposed CSR are challenging. The first goal of the research is to create a mathematical design methodology so that continuous power transfer of WPT-based CSRs can be achieved under any motor operation. Novel methods for DC and AC motor drives are given, and verified experimentally. The second goal is to control the WPT-based CSR and motor separately, although they share the same converter. Frequency and carrier-phase-shift control methods are proposed, which do not affect the motor operation and control the CSR power. Thus, the motor can be controlled by conventional modulation techniques. The final goal is to upscale the proposed system and create practical applications. The field of wound rotor synchronous motors in electric vehicle tractions or wind-turbine pitch control can be energized via the proposed CSR system. Since field excitation requires a low-frequency ripple-free output current of the proposed system, a real-time carrier-phase shift calculation algorithm is developed to diminish sidebands and attain just the switching harmonic. There is a discussion of the cost, complexity, and volume of the proposed system for further improvements and the feasibility of industrial production.

1.4 The Outline of the Thesis

Chapter 2 presents the basics of a wireless power transfer system. The mathematical derivation of WPT parameters is examined. The compensation circuits are compared under application specifications. The selected series-series compensation topology is analyzed using the first harmonic approach, and its characteristic at the resonant frequency is calculated. The selection of the design parameters is discussed concerning the bifurcation phenomenon, and the soft switching conditions are investigated. Finally, multi-frequency IPT systems in the literature are examined to employ within the proposed CSR system.

Chapter 3 shows the theory of the proposed CSR. Firstly, conventional DC motor drives are investigated, and their control and PWM techniques are delivered. The proposed frequency control to decouple the control of the motor and the WPT system is introduced. Then, similarly, AC motor drives are investigated, and a carrier-phase-shift control is proposed. Finally, the feasibility of the proposed system with wide-bandgap semiconductors is discussed.

In Chapter 4, as a proof of concept, a DC motor drive and separately excited DC motor are utilized to validate the proposed CSR. The design methodology concerning the motor drive parameters is presented, and the coil design procedure is presented. The system is modeled, and the iso-power lines are achieved for frequency and duty cycle. Then, the system is experimentally established to validate the concurrent operation. The loss and transient load changes are also examined, and the soft-switching conditions are discussed. Finally, the capacitor stress is investigated to test the system's feasibility for conventional drives.

In Chapter 5, as a proof of concept, an AC motor drive is utilized to validate the proposed CSR. Firstly, the proposed carrier-phase-shift method with SPWM is validated experimentally. Then, an induction machine and a rotating electrical load are concurrently driven by the motor drive. The design methodology is presented concerning the system parameters.

Chapter 6 introduces a practical application to excite the field windings of a synchronous motor using the proposed CSR system. A new algorithm is developed, computing in real-time and eliminating the low-frequency ripples stemming from the sidebands. A series-none WPT system is designed to achieve a rotation-lightweight system. The system is validated experimentally, and the field current with a reduced low-frequency ripple is obtained.

In Chapter 7, the proposed system is summarized, and the advantages-disadvantages are examined. The proposed system is compared with the literature. The contribution of this study is briefly explained, and possible future works are discussed.

CHAPTER 2

OPERATING PRINCIPLES OF WIRELESS POWER TRANSFER SYSTEMS

The inductive power transfer (IPT) system is suitable for CSR's wireless power transfer system for its power and transfer distance capability [26]. Therefore, in this thesis, the IPT system is examined. The operation theory of an IPT system is given, and the compensation type is selected. The bifurcation phenomenon and soft switching conditions are analyzed considering the characteristic circuit parameters such as coupling and quality factors. Finally, multi-frequency IPT systems in the literature are delivered to implement with the proposed CSR.

2.1 Inductive Power Transfer Systems

Inductive power transfer (IPT) systems have a similar operation principle to other isolated power converters where the electrical power is transferred via magnetic induction. They are composed of a converter, compensation circuits, transmitter (Tx)-receiver-Rx coils, and rectifier, as shown in Fig. 2.1 [27].

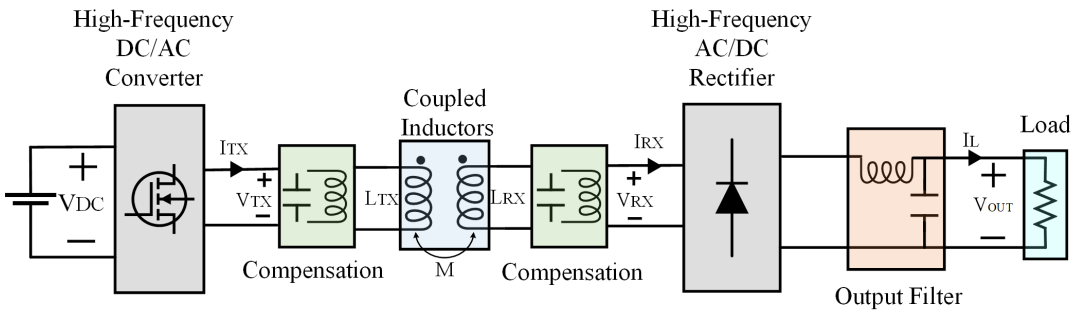

Figure 2.1: The basic representation of IPT systems.

The DC/AC converter generates a high-frequency AC voltage, which creates varying magnetic flux at the Tx coil, obeying Ampere's law. According to Faraday's law, the varying magnetic flux generates an induced voltage at the Rx coil, which is then rectified to achieve DC output voltage.

The magnetic fluxes produced by Tx and Rx coils are not perfectly coupled. The fluxes can be divided into two main parts leakage and magnetizing. The flux linked in Rx can be calculated as given in (2.1)

$$\Phi_{T-Rx} = \Phi_{L-Rx} + \Phi_{M-Rx} + \Phi_{M-Tx} \tag{2.1}$$

where Φ_{L-Rx} is leakage flux of Rx coil, Φ_{M-Rx} is magnetizing flux generated by Rx coil, and Φ_{M-Tx} is magnetizing flux generated by Tx coil. Then, it can be extended as (2.2)

$$\Phi_{T-Rx} = N_{Rx}P_M I_{Rx} + N_{Tx}P_M I_{Tx} + N_{Rx}P_{L-Rx}I_{Rx} \tag{2.2}$$

where P_M and P_{L-Rx} are magnetizing and leakage permanences, and I_{Tx} and I_{Rx} are currents of Tx and Rx coils. The total linked flux is calculated by multiplying the turn ratio and the linked flux, presented in (2.3).

$$\begin{aligned} \lambda = N_{Rx}\Phi_{T-Rx} &= N_{Rx}N_{Rx}P_M I_{Rx} + N_{Rx}N_{Tx}P_M I_{Tx} + N_{Rx}N_{Rx}P_{L-Rx}I_{Rx} \\ &= (L_{M-Rx} + L_{L-Rx})I_{Rx} + MI_{Tx} \\ &= L_{Rx}I_{Rx} + MI_{Tx} \end{aligned} \tag{2.3}$$

where L_{Rx} is the self-inductance of Rx coil and M is the mutual inductance between Tx and Rx coil. The induced voltage of the Rx coil can be calculated as given in (2.4), assuming the system is linear.

$$\begin{aligned} \epsilon &= \frac{d(\lambda)}{dt} \\ &= \frac{d(L_{Rx}I_{Rx} + MI_{Tx})}{dt} \end{aligned} \tag{2.4}$$

Then, the induced voltage of the Rx coil generated by the Tx coil can be formulated as in (2.5).

$$\epsilon = \frac{d(MI_{Tx})}{dt} \tag{2.5}$$

The formulation is converted to the phasor domain as given in (2.6).

$$\epsilon = j\omega MI_{Tx} \tag{2.6}$$

Therefore, the induced voltage is proportional to mutual inductance, operating frequency, and magnitude of Tx current. However, the power factor of IPT systems is lower due to high leakage inductance from inherently loose couplings, as can be found by comparing (2.4) and (2.5).

2.2 Compensation Topologies of IPT Systems

A common problem for IPT systems is the high leakage inductance which decreases the power factor of the system. When the transfer distance is increased, the leakage inductance becomes dominant, considerably decreasing the system's efficiency. Besides, the system requires higher VA ratings to transfer the same power in a higher leakage inductance. Higher VA ratings also increase the cost and volume of the system. In order to mitigate this problem, compensation circuits are used [28]. They compensate for the leakage inductance and approach to the unity power factor, resulting in higher efficiency and lower VA ratings.

Basically, a compensation circuit is a capacitor that can be connected in parallel or in series with coils. The transmitter, receiver, or both sides can be compensated. Generally, the Tx-side is compensated concerning the overall inductance of the system, including the reflected impedance from the Rx-side. In addition, the Rx side is compensated for the Rx side inductance only. There are four commonly used two-element compensation topologies, which are series-series (SS), series-parallel (SP), parallel-series (PS), and parallel-parallel (PP), as shown in Fig. (2.2) [29]. They are composed of series or parallel capacitors connected to both the Tx and the Rx sides.

In addition to these topologies, single-side compensation or hybrid compensations with capacitors and inductors such as LLCL, LCL, and LCC exist [30, 31]. Each compensation method has advantages and drawbacks, so compensation selection depends on the system requirements and applications. Primary series connection is used with voltage source inputs, whereas primary parallel requires a current source input [32]. Similarly, the output of the receiver parallel system acts like a current source, while the output of the receiver series system behaves like a voltage source[33].

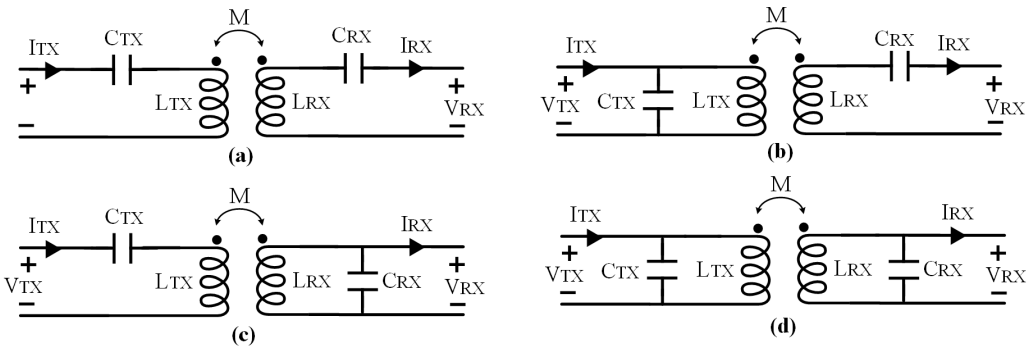

Figure 2.2: The circuit representation of basic two-element compensation methods.

Here, analyses and comparisons of these basic topologies will be presented. Firstly, the receiver capacitor is selected to compensate for the inductance of the receiver side, calculated as given in (2.7).

$$C_{Rx} = \frac{1}{\omega_r L_{Rx}} \tag{2.7}$$

However, the transmitter capacitor should compensate for the input inductances, where the input impedances (with reflected components) are given in (2.8).

$$Z_{in} = Z_{TX} + \frac{\omega_r^2 k^2 L_{Tx} L_{Rx}}{Z_{Rx}} \tag{2.8}$$

Z_{Tx} and Z_{Rx} are calculated considering the compensation types. For series compensation, they are calculated as given in (2.9), whereas they are calculated as given in (2.10) for parallel compensation.

$$\begin{aligned} Z_{Tx} &= j\omega L_{Tx} + \frac{1}{j\omega C_{Tx}} \\ Z_{Rx} &= j\omega L_{Rx} + \frac{1}{j\omega C_{Rx} + R_L} \end{aligned} \tag{2.9}$$

$$\begin{aligned} Z_{Tx} &= \frac{1}{j\omega C_{Tx}} \,||\, j\omega L_{Tx} \\ Z_{Rx} &= j\omega L_{Rx} + (\frac{1}{j\omega C_{Rx}} \,||\, R_L) \end{aligned} \tag{2.10}$$

Therefore, the transmitter capacitance is calculated as given in (2.11 to 2.14), where ω_r is the resonant frequency in radians per second.

$$C_{Tx} = \frac{1}{\omega_r^2 L_{Tx}} \tag{2.11}$$

$$C_{Tx} = \frac{1}{\omega_r^2 (L_{Tx}(1-k^2))} \tag{2.12}$$

$$C_{Tx} = \frac{1}{\omega_r^2 (L_{Tx} + \frac{\omega_r^2 k^4 L_{Rx}^2 L_{Tx}}{R_L})} \tag{2.13}$$

$$C_{Tx} = \frac{1}{\omega_r^2 (L_{Tx}(1-k^2)) + (\frac{R_L^2 k^4 L_{Tx}}{1-k^2})} \tag{2.14}$$

As comparison, SS topology gives a coupling and loading independent resonant frequency since their capacitance values are calculated only by the self-inductance of the Tx and Rx coil [34]. SP topology gives a loading independent resonant frequency, but the coupling changes its resonant frequency. Both coupling and loading affect the resonant frequency of PS and PP compensated topologies. Thus, SS topology is the most preferred topology. However, SS topology also has a few drawbacks. Their capacitor sizes are larger than the one used in other topologies since all the Tx and Rx current pass through the capacitors. Moreover, it does not allow zero-load operation at the resonant frequency and will draw short-circuit current under no-load conditions. The input impedance of the no-load condition (including internal resistance of the inductance) can be calculated as presented in (2.15).

$$\begin{aligned} Z_{in} &= j\omega L_{Tx} + \frac{1}{j\omega C_{Tx}} + r_{Tx} + \frac{\omega^2 k^2 L_{Tx} L_{Rx}}{j\omega L_{Rx} + \frac{1}{j\omega C_{Rx}} + r_{Rx} + R_L} \\ Z_{in}{}^{(\omega \longrightarrow \omega_r)}_{(R_L \longrightarrow 0)} &= r_{Tx} + \frac{\omega_r^2 k^2 L_{Tx} L_{Rx}}{r_{Rx}} \end{aligned} \tag{2.15}$$

In this thesis, SS-IPT topology is preferred since it fits CSR applications due to their coupling and loading independent resonant frequency. The remaining analyses will be made for the SS-IPT system.

2.3 SS-IPT Systems

The circuit diagram of a SS-IPT system is presented in Fig. 2.3. The converter generates a pulsating output voltage. Since compensation capacitors create a resonant structure, it allows only the fundamental frequency to pass. So, the currents of Tx and Rx are purely sinusoidal, and the first harmonic approaches (FHA) can be used to model and design the system [35].

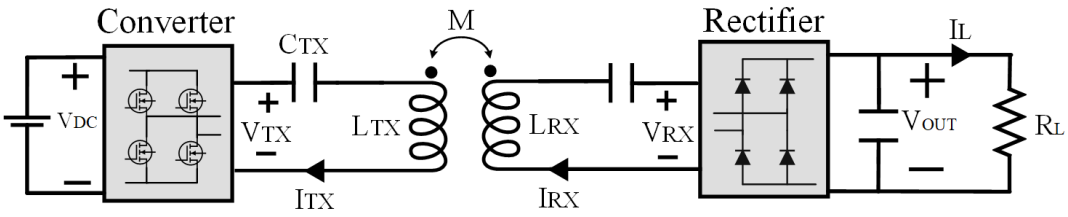

Figure 2.3: The circuit representation of conventional SS-IPT systems.

The FHA model is represented in Fig. 2.4.

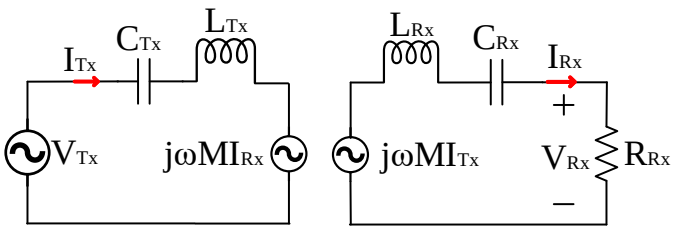

Figure 2.4: The circuit diagram of an SS-IPT system with first harmonic approach.

The Rx-side resistance (R_{Rx}) is the reflected resistance from the rectifier. Since the Rx current is sinusoidal, the reflected resistance is calculated as given in (2.16).

$$R_{Rx} = \frac{8}{\pi^2} R_L \tag{2.16}$$

The line impedance (series connected inductance and capacitance) behaves like a short circuit at the resonant frequency. Then V_{Rx} is equal to the induced voltage from

the transmitter side, as given in (2.17).

$$V_{Rx} = j\omega M I_{Tx} \tag{2.17}$$

To find I_{Tx}, the R_{Rx} is reflected to the Tx-side as presented in (2.18).

$$R_{ref} = \frac{\omega_r^2 M^2}{R_{Rx}} \tag{2.18}$$

Then, I_{Tx} is found by (2.19), and so the voltage gain is calculated as given in (2.20) using (2.17).

$$\begin{aligned} I_{Tx} &= \frac{V_{Tx}}{R_{Rref}} \\ &= \frac{V_{Tx} R_{Rx}}{\omega_r^2 M^2} \end{aligned} \tag{2.19}$$

$$\begin{aligned} A_{WPT} &= \frac{V_{Rx}}{V_{Tx}} \\ &= \frac{R_{Rx}}{\omega_r^2 M} \end{aligned} \tag{2.20}$$

The gain at the resonant frequency is proportional to load resistance and inversely proportional to the mutual inductance. Besides, the gain decreases moving away from the resonant frequency due to the band-pass structure [36]. However, depending upon the circuit parameters, the single peak band-pass characteristic may alter to a double peak structure. The phenomenon is called bifurcation and depends on the system coupling and quality factors [37]. A single-peak and double-peak structures are presented in Fig. 2.5. The single-peak structure is significant in controlling the output power by frequency since it allows the linear control region to decrease power monotonously after the resonant frequency. In a double-peak structure, the system does not have a monotonously increasing or decreasing power after the resonant frequency, which makes frequency control difficult.

Moreover, the system behaves like a capacitive at frequencies below the resonant frequency, whereas it acts like an inductive at frequencies above the resonant frequency. However, the bifurcation phenomenon changes the input current phase characteristic, and there are three transitions between the capacitive and inductive regions, as shown in Fig. 2.6. The inductive and capacitive regions affect the soft-switching conditions, and guaranteeing inductive operations increasing the overall efficiency.

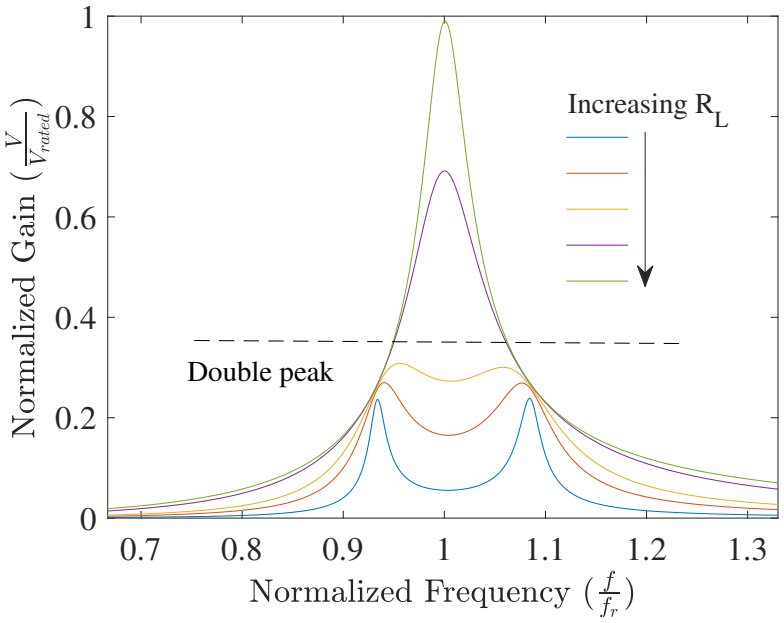

Figure 2.5: The gain response for various load resistances.

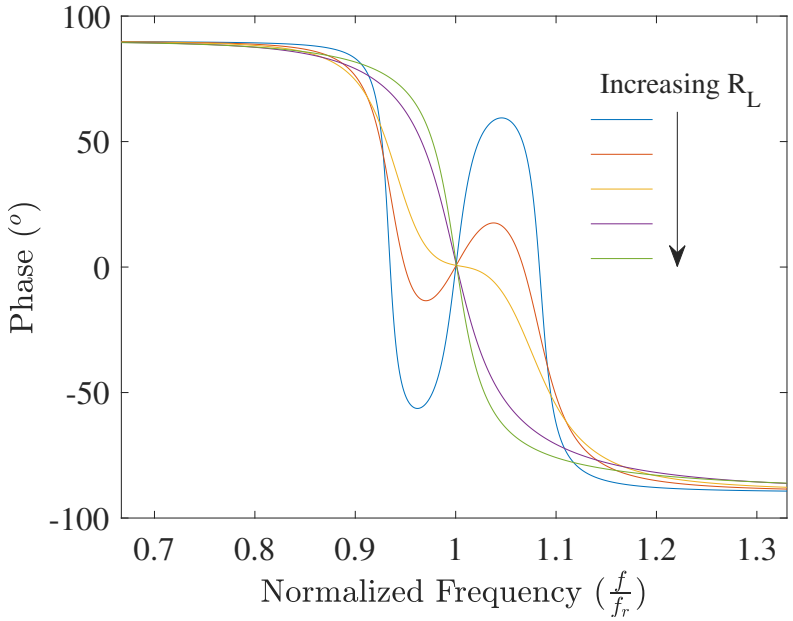

Figure 2.6: The phase response for various load resistances.

2.4 The Bifurcation Phenomenon

In the design stage, the coupling and the quality factor determine whether the system enters the bifurcation. The quality factor is defined as the ratio of reactive and real power, calculated as given in (2.21).

$$Q = \frac{P_{reactive}}{P_{real}} \tag{2.21}$$

In the double compensated systems, there are two quality factor definitions for the transmitter and receiver side, respectively, as calculated in (2.22).

$$\begin{aligned} Q_{Tx} &= \frac{\omega_r L_{Tx}}{\frac{\omega_r^2 M^2}{R_{Rx}}} \\ Q_{Rx} &= \frac{\omega_r L_{Rx}}{R_{Rx}} \end{aligned} \tag{2.22}$$

The Q_{Tx} can be simplified as a function of Q_{Rx} and k, as given in (2.23).

$$Q_{Tx} = \frac{1}{k^2 Q_{Rx}} \tag{2.23}$$

Therefore, coupling and receiver quality factors can represent the overall system characteristics. If the voltage gain-frequency response is plotted in Fig. 2.7 for different Q_{Rx} and k, it is observed that the bifurcation phenomena occur depending upon the relationship between them.

For a constant value of Q_{Rx}, the system enters bifurcation after some coupling value called the critical coupling. In [38] the k_c is formulated as given in (2.24).

$$k_c = \frac{1}{Q_{Rx}} \sqrt{1 - \frac{1}{4Q_{Rx}^2}} \tag{2.24}$$

In the design stage, k should be selected concerning this critical coupling to avoid bifurcation, which makes the control difficult and decreases efficiency.

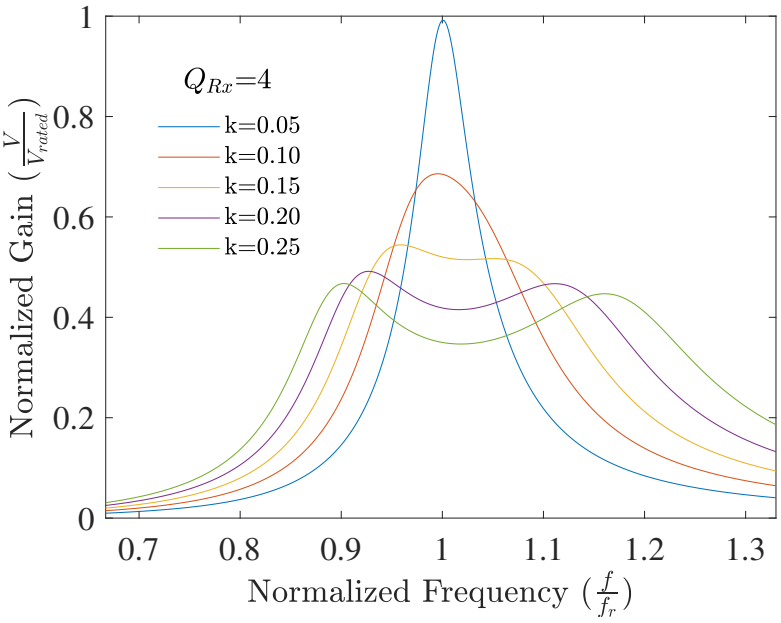

(a)

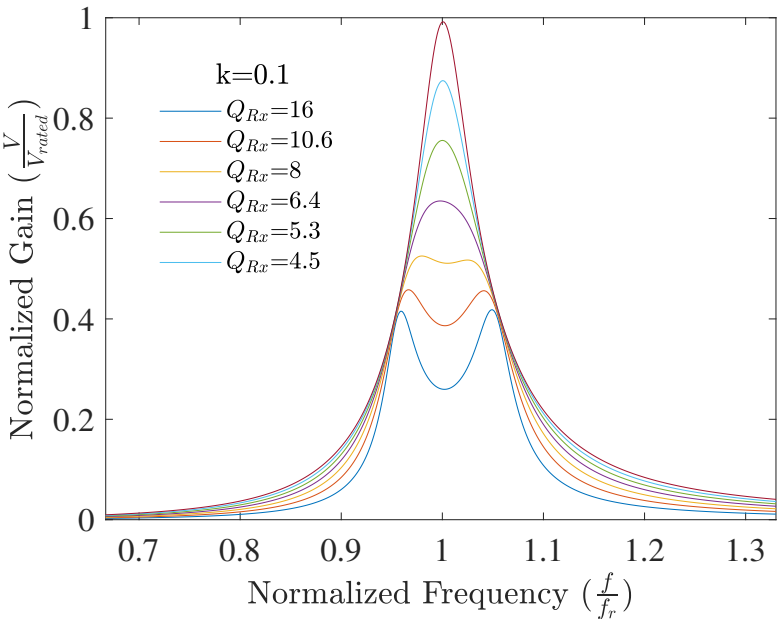

(b)

Figure 2.7: The gain responses. a) For various quality factors b) For various couplings.

2.5 Soft-Switching Conditions

The loss sources of the IPT system can be divided into two main parts: coil losses and semiconductor losses. In order to reduce coil losses, the copper area is increased, and litz wires are also used to avoid eddy and proximity losses [39]. For semiconductor losses, conduction losses and switching losses of power switches of the DC/AC converter and rectifier exist. The switching loss is dominant compared to conduction loss since the operating frequency of the IPT system is increased to reduce coil sizes. However, thanks to the resonant structure, the system can make zero voltage or zero current switching (ZVS or ZCS), considerably reducing switching losses. The ZVS and ZCS conditions depend on the operation region of IPT (inductive and capacitive region).

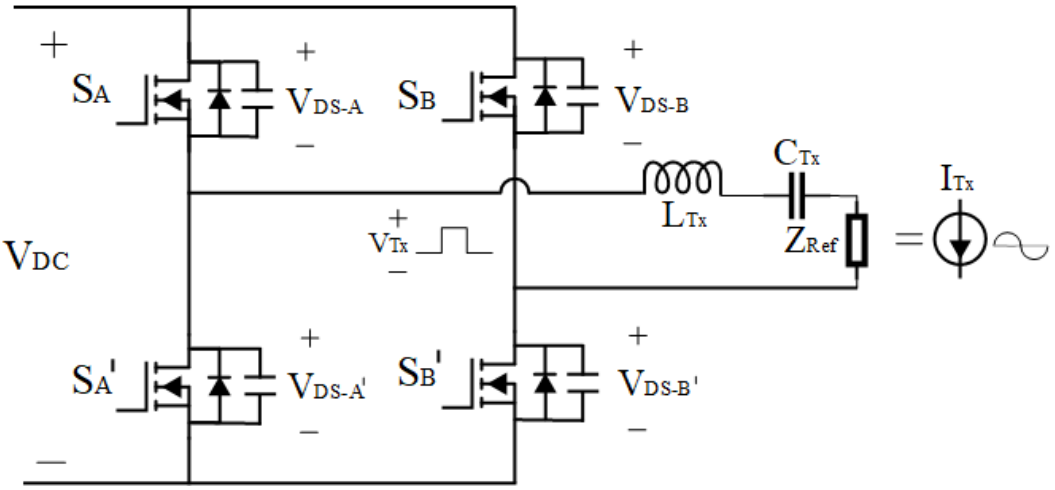

Figure 2.8: A full-bridge converter with a series-series IPT system.

A full-bridge converter is presented in Fig. 2.8. The Tx current (I_{Tx}) is purely sinusoidal, and it leads or lags the voltage (V_{Tx}) regarding the operation region.

2.5.1 Capacitive Region

Below the resonant frequency, the IPT system acts like a capacitive load if it is not in bifurcation. The capacitive load causes the current leads, and so the power factor is leading. Drain-source, gate-source voltages of S_A, and the load current are plotted for this operation region in Fig. 2.9. In this condition, the switches make a hard

switching during turn-on. Due to the switching losses mainly stemming from the turn-on transition, the switching losses are dominant in the capacitive region.

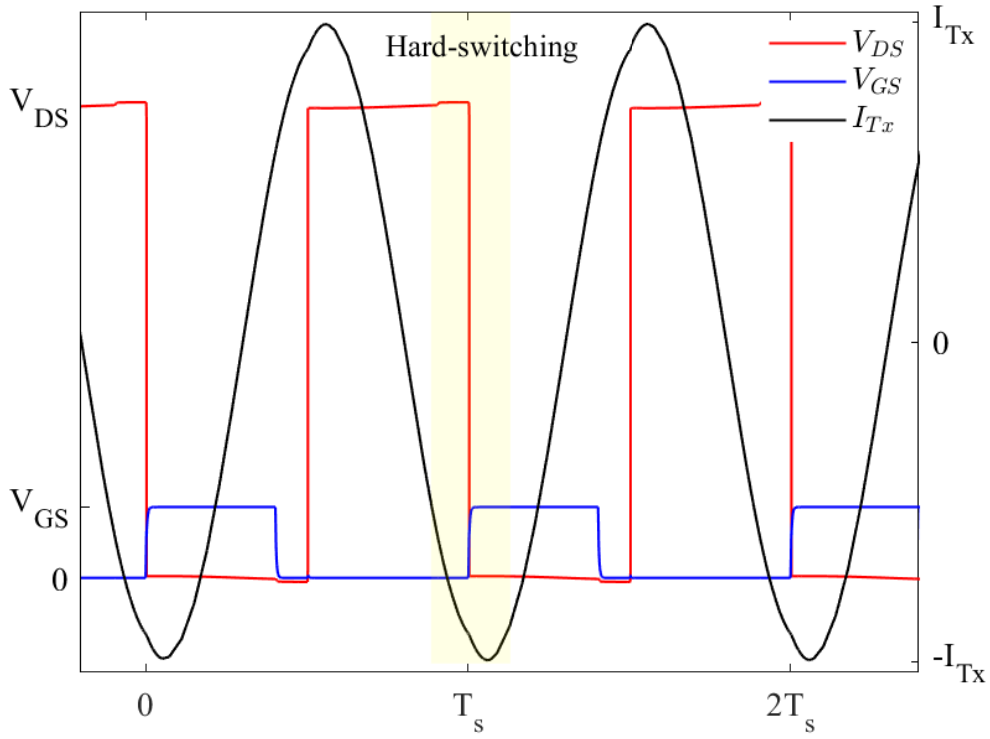

Figure 2.9: The current and voltage waveforms of a FB converter in capacitive region.

2.5.2 Inductive Region

Above the resonant frequency, the IPT system acts like an inductive load if it is not in bifurcation. The inductive load causes the current lags, so the power factor lags. Before the gate signals are high, dead time (blanking time) exists to avoid short circuit the DC-link. During the dead time period, the output capacitance of the switches discharges by the load current, so the switches make ZVS at the turn-on. A drain-source, gate-source voltages of S'_A, and the load current is plotted for this operation region in Fig. 2.10.

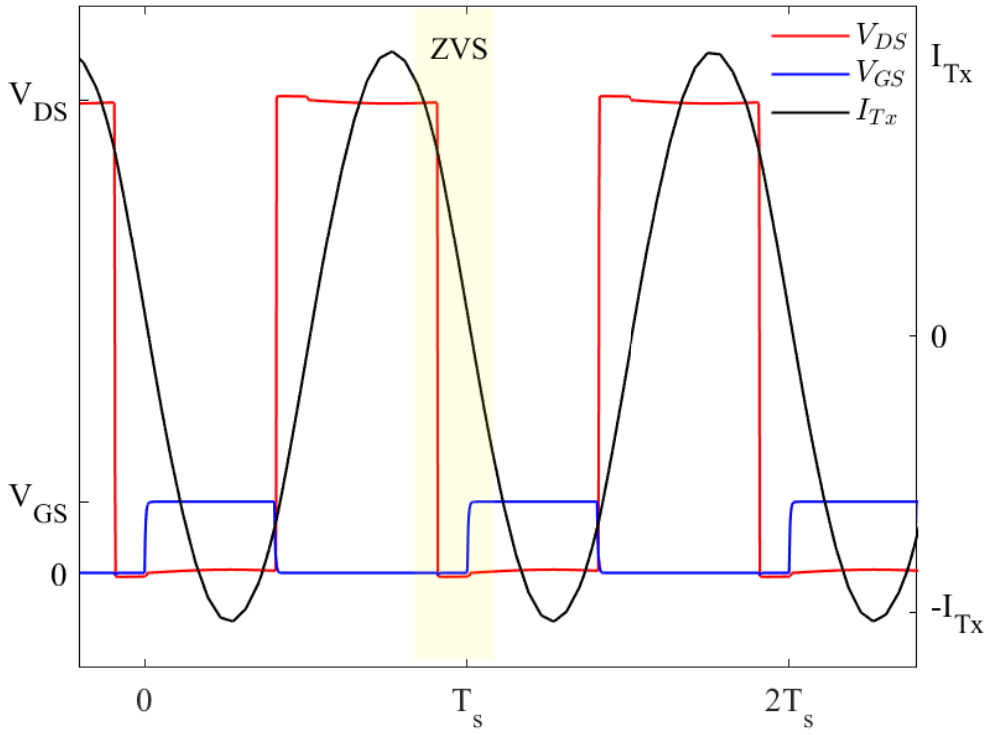

Figure 2.10: The current and voltage waveforms of a FB converter in the inductive region.

2.6 Multi-Frequency IPT Systems and The Proposed CSR Method

Thus far, conventional IPT systems have been examined. Conventional IPT systems use a single frequency to transfer power, even though the high-frequency converter generates a pulsating square wave. However, recent studies have addressed the multi-frequency power transfer to decrease the switching numbers or increase the utilization of DC-link voltage. As the proposed CSR system is concurrently excited by the converter of the motor drive that energizes the motor, the multi-frequency approaches in the WPT literature should be investigated to develop the system. In [40], a single inverter is used with multi-resonant circuits amplifying the square wave's fundamental and third harmonic. The third harmonic component increases the transmitted power without increasing the VA rating of the semiconductor devices. However, it is not possible to independently regulate the third harmonic component in such a system. In [41], a dual-band WPT system is introduced to make Tx compatible with

two different WPT standards. However, two separate sets of coils and drivers are used, allowing design flexibility but increasing system complexity and cost. In [42], a single-inverter-based dual-frequency WPT system is proposed using the programmed PWM method. The system can regulate the output voltage for multiple receivers. The programmed PWM adjust the operating frequency of one of the WPT system to the switching frequency to minimize the switching losses. Nevertheless, the programmed PWM is computationally complex since it requires switching angle calculation using offline algorithms. Hence, such a method is not feasible to employ in dynamic systems. In [43], multi-frequencies are achieved by comparing superimposed sinusoidal reference signals with the high-frequency triangle carrier signals. In addition, a phase shift can be given between superimposed reference signals to increase the utilization rate of the DC-link voltage [44]. Yet, in these methods, the switching frequency is higher than the operating frequencies of the WPT system, which increases switching losses. Apart from the aforementioned studies, multi-frequency systems can also be implemented to combine wireless and wired power transfer concurrently since they could co-exist in dynamic applications [45, 46].

One of these applications is a contactless slip ring (CSR). In the proposed system, the CSR is excited by the converter of a motor drive. Thus, eliminating the extra CSR converter reduces the system's cost and complexity. However, the conventional motor drive method should be applied rather than the mentioned multi-frequency approaches while implementing the proposed CSR since driving a motor requires fast and dynamic controls. Therefore, this study aims to develop a new multi-frequency motor and WPT system using conventional motor drive methods.

CHAPTER 3

THEORY OF THE PROPOSED CONCURRENT WIRELESS POWER TRANSFER AND MOTOR DRIVE SYSTEM

In this chapter, the multi-frequency approach explained in the previous chapter will be expanded into a system that is able to transfer concurrent wired and wireless power. The proposed system fits contactless slip ring (CSR) applications, and the required multi-frequency converter is achieved just with the existing motor drives. However, the conventional modulation techniques to drive the motor should be used since the motor requires dynamic control and fast response. Moreover, achieving continuous/-constant power transfer with the proposed CSR under modulation techniques used in conventional motor drives is challenging. In this study, control methods that can be applied for both DC and AC motors are asserted to transfer concurrent wired and wireless power with conventional modulation techniques.

This chapter introduces the proposed methods and systematically investigates the theory of their operation. The rest of the chapter is organized as follows. Firstly, the proposed CSR is compared with conventional ones. Secondly, conventional motor drives are presented, and the voltage source converters are examined. Thirdly, DC motor drives are reviewed, where their speed/torque control and applied modulation techniques are analyzed. In addition, the proposed control method, which concurrently drives the motor and excites the proposed CSR, is introduced. Fourthly, AC motor drives are surveyed similarly to DC motor drives. Fifthly, the other current PWM techniques are discussed to implement the proposed CSR. Finally, practical considerations of implementing the proposed system with conventional drives are examined, and the importance of wide-bandgap switches is explored.

3.1 The Proposed Contactless Slip Ring System

A conventional CSR is shown in Fig. 3.1.a, which consists of two separate converters to drive the motor and excite the WPT system. The already existing motor drive in these systems generates high-frequency switching voltage harmonics, which are not desired, and attenuated in the motor phase currents due to large motor phase inductances.

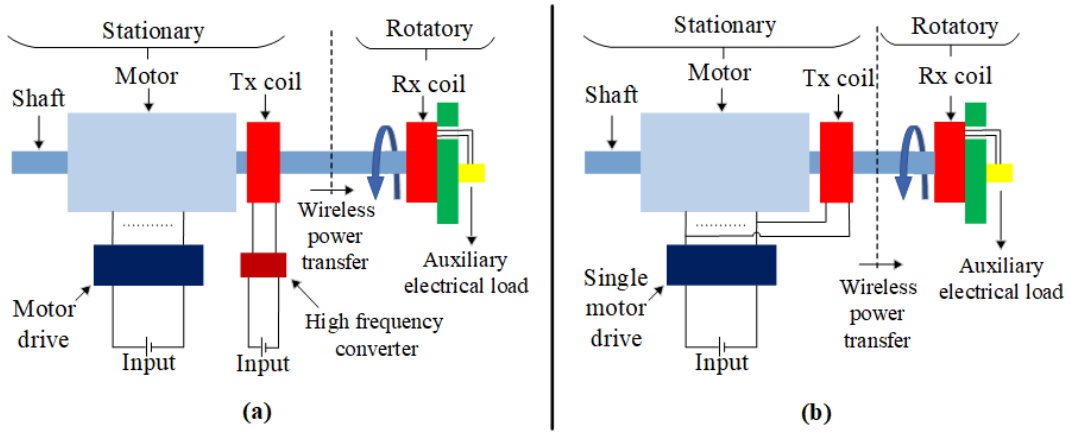

Figure 3.1: An example representation of CSRs based on WPT systems. a) A conventional system. b) The proposed system.

In the proposed system, the Tx coil utilizes these high-frequency voltage harmonics to transfer power to the Rx coil on the rotating frame, while the low-frequency modulated current is still used to drive the motor. Therefore, the converter of the motor drive is used as the single converter by the proposed multi-frequency approaches. Thus, a separate high-frequency converter of the WPT system is no longer required, reducing cost and complexity. The proposed system, as shown in Fig. 3.1.b, can be used to energize auxiliary loads in the rotating frame for industrial applications such as IoT devices, surveillance cameras, robotic actuators, radars, sensors, etc., or to excite the field windings of the synchronous motors [8, 9, 7, 47, 48, 10]. Since the power ratings of these loads are lower than the power ratings of the motor, it is possible to use just the existing conventional motor drive, which will be discussed in the coming parts, without any extra hardware.

3.2 Motor Drives

Motor drives are frequently used in industry, such as robotic arms and conveyor belts, in the consumer products, such as electric vehicles (EVs), and in renewable energy sources, such as wind turbines [49, 50, 51]. They can be used to drive both DC and AC motors. DC motor drives adjust the DC voltage/current to control the speed and torque of motors. Unlike DC motor drives, AC motor drives also adjust the frequency to control the speed of motors; thus, AC motor drives are also named variable frequency drives (VFDs). Motor drives generally comprise a measurement unit, controller, and DC/DC or DC/AC converter, as shown in Fig. 3.2.

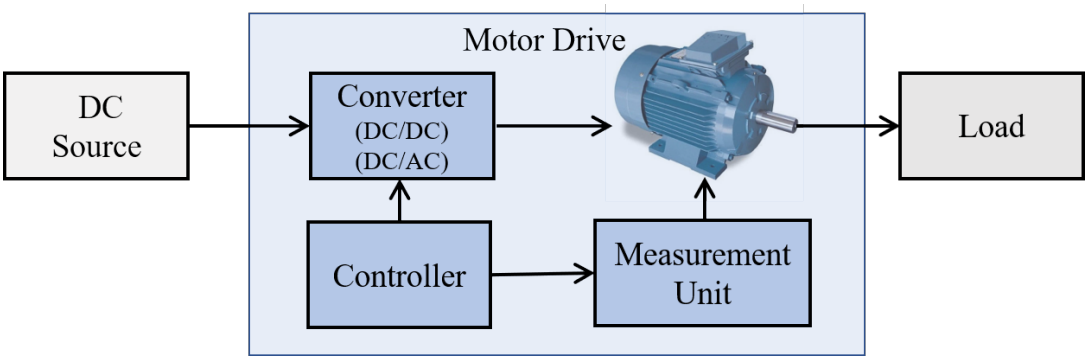

Figure 3.2: Block diagram of a conventional motor drive system.

The converter of the motor drives can be a current source converter (CSC) or a voltage source converter (VSC). Whereas VSCs commonly use MOSFETs and IGBTs where unidirectional voltage is blocked, CSCs use diodes and thyristors where unidirectional current passes. Under constant input voltage, VSCs generate a pulsating output voltage independent of loading. On the contrary, under constant input current, CSCs generate a pulsating output current independent of loading. The majority of motor drives use VSCs due to the natural unidirectional voltage blocking capability of typical switches[52]. Therefore, in this study, VSC-based motor drives are utilized to address general usage. Since VSC-based motor drives provide an independent output voltage from the loading of the motor, the proposed CSR (a WPT system) should be connected parallel to the motor.

3.3 DC Motor Drives

There are two main parts in DC motors: field and armature. The field is on the stationary frame, while the armature is on the rotating frame. In industry, separately excited DC motors, where the field and armature windings are independently fed, are commonly used since they provide sensitive speed and torque control compared to other DC motors such as series, shunt, and compound [53]. Therefore, the proposed CSR method will be investigated for implementation with separately excited DC machines, and their control will be analyzed. Instead of separately-excited DC motors, a permanent magnet (PM) DC motor can also be used, which behaves like a constant current fed field winding. Also, the methodology can be easily applied to other types of DC machines.

3.3.1 Speed and Torque Control

The equivalent circuit schematic of a separately excited-DC machine is presented in Fig. 3.3.

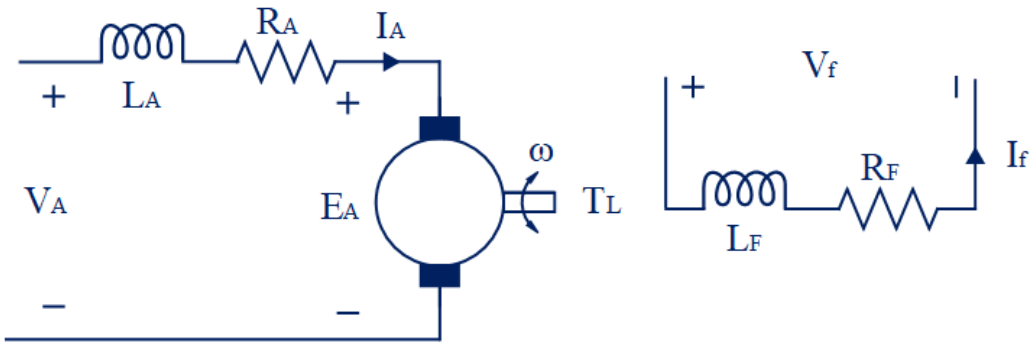

Figure 3.3: The electrical equivalent circuit schematic of the separately excited DC motor.

The induced emf on the armature (E_A) is proportional to speed, as in (3.1), where K_A is the motor back-emf constant.

$$E_A = K_A \omega \tag{3.1}$$

The torque is proportional to the current, as calculated in (3.2).

$$T = K_A I_A \tag{3.2}$$

Therefore, to achieve the desired speed and torque references, I_A and E_A should be controlled. The control is provided with armature voltage under constant field excitation that implies constant K_A. In addition, the field current, and therefore K_A, can be adjusted to increase speed performance. The control block diagram of a conventional DC motor drive is shown in Fig. 3.4.

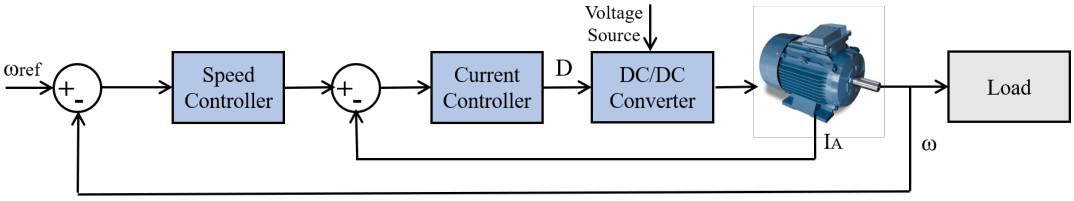

Figure 3.4: The control diagram of conventional DC motor drives.

3.3.2 The Proposed Modulation Technique

In the last part, the required armature voltage of the motor was found according to desired speed and torque. This voltage can be generated using a full-bridge VSC, shown in Fig. 3.5. The converter is driven by a bipolar-PWM, as given in Fig. 3.6, which yields an output voltage (V_o) having DC but also high-frequency switching harmonics. In this modulation technique, S_A and S'_B (hence S_B and S'_A) have the same switching patterns. The switching function of the bipolar-PWM is presented in (3.3), composed of switching frequency (f_s), and duty cycle (D). The harmonic distribution of V_o is plotted in Fig. 3.7.

$$S(t) = \mathrm{D} + \sum_{\mathrm{k}=1}^{\infty} \frac{2}{\mathrm{k}\pi} \sin(\mathrm{k}\pi\mathrm{D})\cos(2\pi\mathrm{k}\mathrm{f_s}\mathrm{t}) \tag{3.3}$$

While a positive DC output voltage is achieved for duty cycle (D) values greater than 0.5, a negative DC output voltage is achieved for D values less than 0.5. At $D = 0.5$, the DC output becomes zero, meaning that the power transferred to the motor is zero. Thus, variable positive and negative DC output voltage is produced by changing the duty cycle.

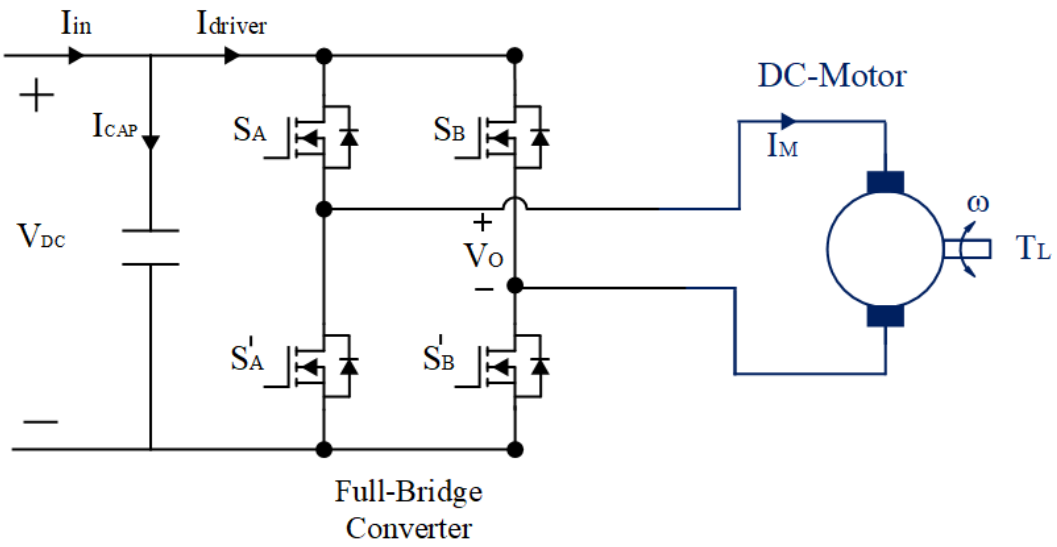

Figure 3.5: The circuit diagram of a full-bridge VSC based DC motor drive.

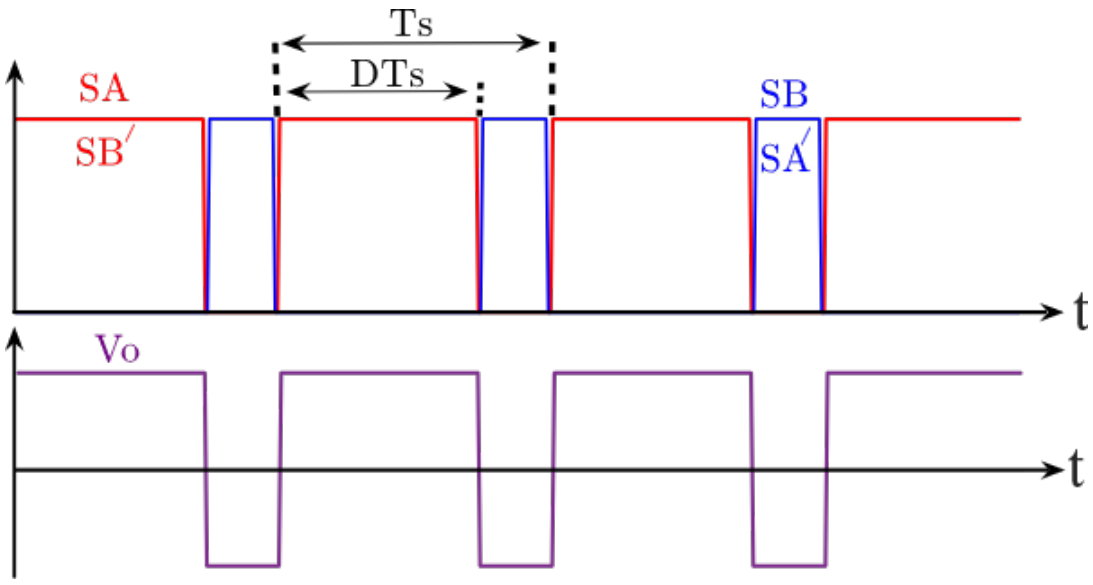

Figure 3.6: The switching signals and output voltage of the full-bridge VSC.

3.3.3 Control Methodology of The Proposed CSR System

In the proposed system, the CSR is connected in parallel to the DC motor as presented in Fig. 3.8, and a full-bridge VSC, which bipolar PWM drives, is used. The resonant frequency of the WPT system should be selected close to the switching frequency so that the harmonics can excite the WPT system.

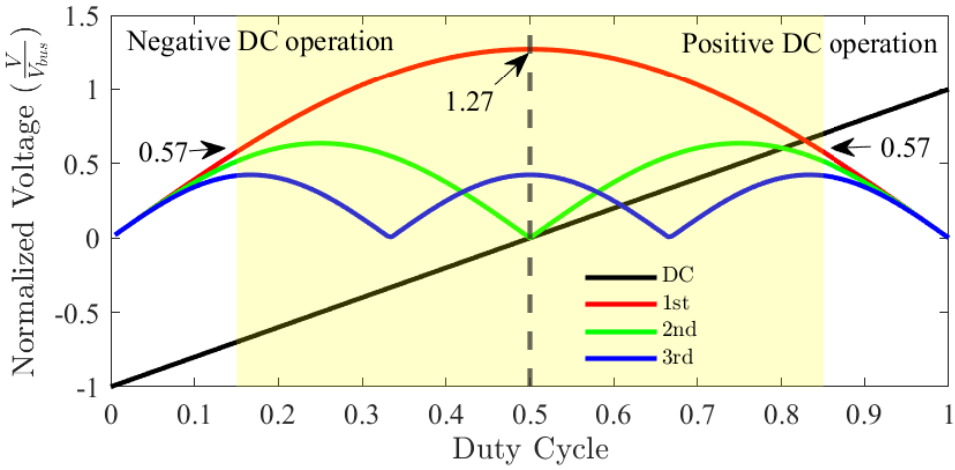

Figure 3.7: The harmonic distribution of the converter's output voltage, which are obtained by analytically employing the switching function in the FB converter.

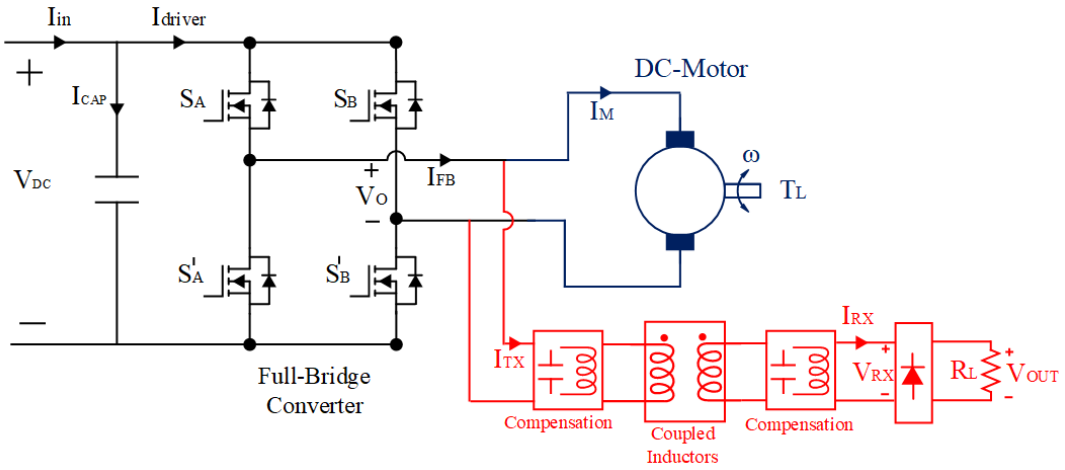

Figure 3.8: Circuit diagram of the proposed concurrent motor drive and WPT system with a single converter.

However, the magnitude of these harmonics varies with the duty cycle, as can be seen in Fig. 3.7, so two main problems are revealed. The first problem is the diminishing switching harmonics at duty cycles close to 0 or 1. The problem can be solved by restricting the duty cycles so continuous/constant power can be cultivated by the proposed CSR. For example, the duty cycle can be confined between 0.15 and 0.85. This restriction reduces the DC-link utilization for the motor operation, but a similar restriction already exists in conventional drives due to the dead times of the switch-

ing. The second problem is to control the proposed CSR's power under dynamically varying duty cycles. This problem can be solved with two different methods. The first one is to add post-regulation with an active converter to the receiver side rather than using a passive full-bridge diode rectifier, but it increases the cost, complexity, and weight of the rotating side. The second method is to detune the switching frequency, commonly used in regular WPT systems. Since the motor winding attenuates the high-frequency harmonics in motor current, the variable switching frequency does not affect the motor operation. Thus, the variable switching frequency can be applied to the motor drives to control the CSR's power.

Consequently, the overall control diagram for the proposed CSR is given in Fig. 3.9. The motor controller decides on the duty cycle, considering the desired speed and torque references. Then, the controller of the CSR adjusts the switching frequency to reach the desired CSR's output power under these different motor operations.

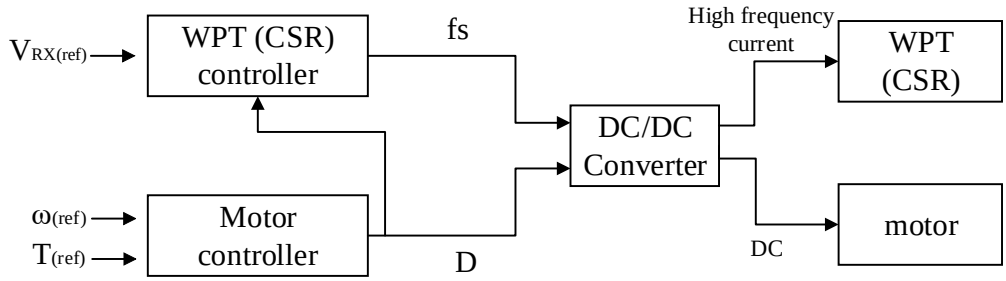

Figure 3.9: The block diagram of the control method of the proposed system.

A steady-state expected voltage and current waveforms for an operation point are presented in Fig. 3.10 where the gate signals of the top switches of each leg (S_A and S_B) are shown. The switching pattern generates a pulsating output voltage (V_o), with DC and switching components. The motor current (I_M) is mainly DC with small current ripples. The Tx current (I_{TX}) is sinusoidal, assuming that the WPT system has a high-quality factor. The FB converter current (I_{FB}) is the sum of I_M and I_{TX}. However, I_{FB} is dominated by I_M since the CSR is used for auxiliary systems with smaller power ratings than the motor.

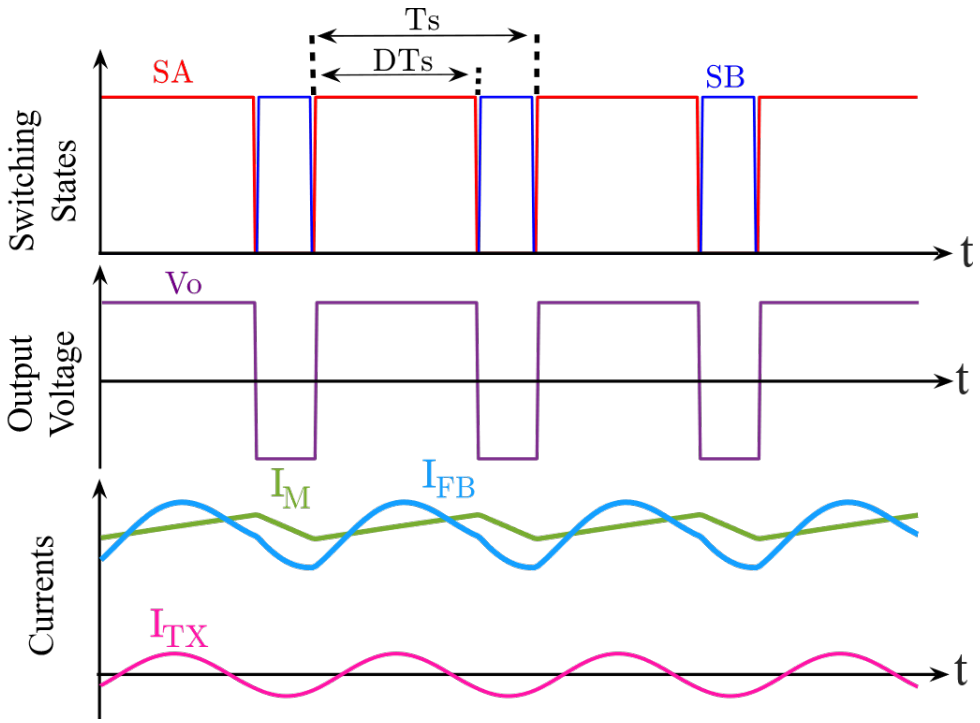

Figure 3.10: Asymmetrical PWM signals and its corresponding voltage and current waveforms. SA: Gate-source signal of switch S_A, SB: Gate-source signal of switch S_B, D: Duty cycle, Ts: Switching period, I_M: Motor current, I_{FB}: Converter current, I_{Tx}: Transmitter current.

3.4 AC Motor Drives

There are two main parts in AC machines: field and armature. According to the AC machines type, the method of field excitation changes. For induction machines (IMs), the field on the rotor is fed by induction; thus, external excitation is not required. Their armature on the stator is fed with AC voltages, and the rotating magnetic field, generated by the armature current, induces a voltage on the field windings. So, IMs have a simple structure without brushes or permanent magnets on the rotating frame, making them robust [54]. Accordingly, the control of IMs is achieved using AC excitation with variable frequency and magnitude to just the armature windings. In synchronous machines (SMs), the field winding on the rotor is excited by DC voltage (or permanent magnets can be used to excite), while the armature winding on the stator is fed with AC voltage. Unlike IMs, the control of SMs can be achieved by armature control (AC voltages with variable frequency, angle, and magnitude) or field

control (with DC voltage/current). However, the field control does not regulate the speed of the motor, and it is usually used to increase high-speed performance [55]. Consequently, AC motor drives are supposed to generate variable frequency output voltages, which feed the armatures of AC machines. There are other types of AC machines, but in this study, SMs and IMs are investigated to implement the proposed CSR, and it can also be easily implemented in other AC machines.

3.4.1 Speed and Torque Control

The speed of the stator excitation is called synchronous speed. IMs do not operate at synchronous speed, so the rotor mechanical speed should differ from the synchronous speed to achieve net torque.

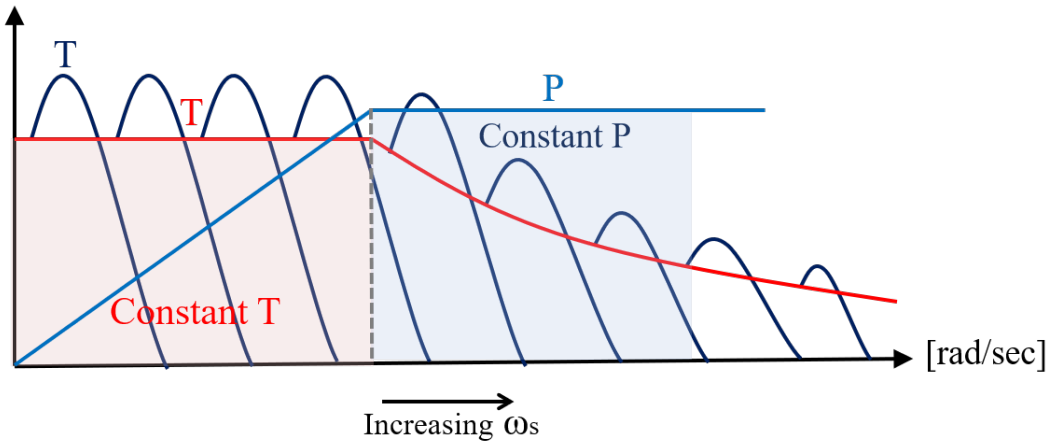

Figure 3.11: Torque-speed characteristic of IMs. (ω_s is synchronous speed, P and T are power and torque.)

The difference between the rotor and synchronous speed per unit is called slip. This slip is required in order to excite the field winding by induction. The torque-speed characteristic of IMs and their electrical equivalent circuit is shown in Fig. 3.11 and Fig. 3.12.

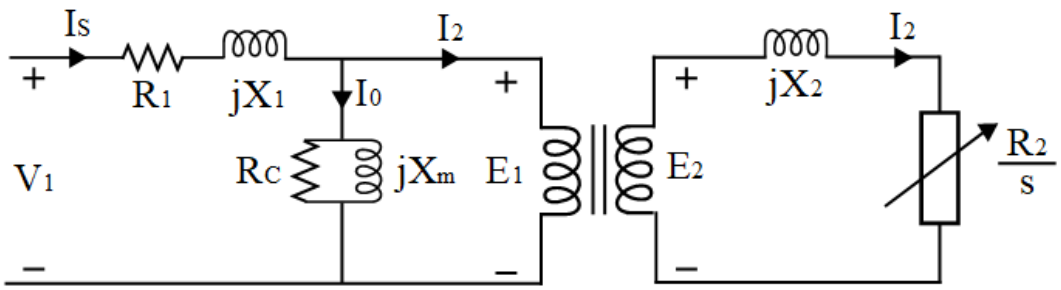

Figure 3.12: The electrical equivalent circuit representation of IMs.

The generated torque can be calculated as given in (3.4), where R_2^r and X_2^r is reflected resistance and impedance.

$$T = \frac{3V_1^2}{(R_1 + \frac{R_2^r}{s})^2 + (X_1 + X_2^r)^2} \frac{R_2^r}{s\omega_s} \tag{3.4}$$

The rotor speed is calculated using s and ω_S as given in (3.5).

$$\omega_r = (1 - s)\omega_s \tag{3.5}$$

On the contrary, SMs operate at synchronous speed. Therefore, the mechanical speed is directly controlled by the electrical frequency. The torque is controlled by the armature current, which is adjusted via the applied armature voltage. Moreover, the field current can be controlled to obtain high-speed performance. The torque-speed characteristic of SMs and their electrical equivalent circuit is shown in Fig. 3.13 and Fig. 3.14. The induced emf on the AC motor is proportional to the speed of the motor, calculated as in (3.6), where K is the motor back-emf constant that depends on the field excitation.

$$E_A = K\omega_s \tag{3.6}$$

The armature current in the phasor domain is calculated as given in (3.7).

$$\overrightarrow{I_a} = \frac{\overrightarrow{V_t} - \overrightarrow{E_A}}{R_a + jX_s} \tag{3.7}$$

The motor operates at synchronous speed, and its torque is calculated as given in (3.8).

$$T_e = 3\frac{\overrightarrow{E_f}\overrightarrow{I_a}}{\omega_s} \tag{3.8}$$

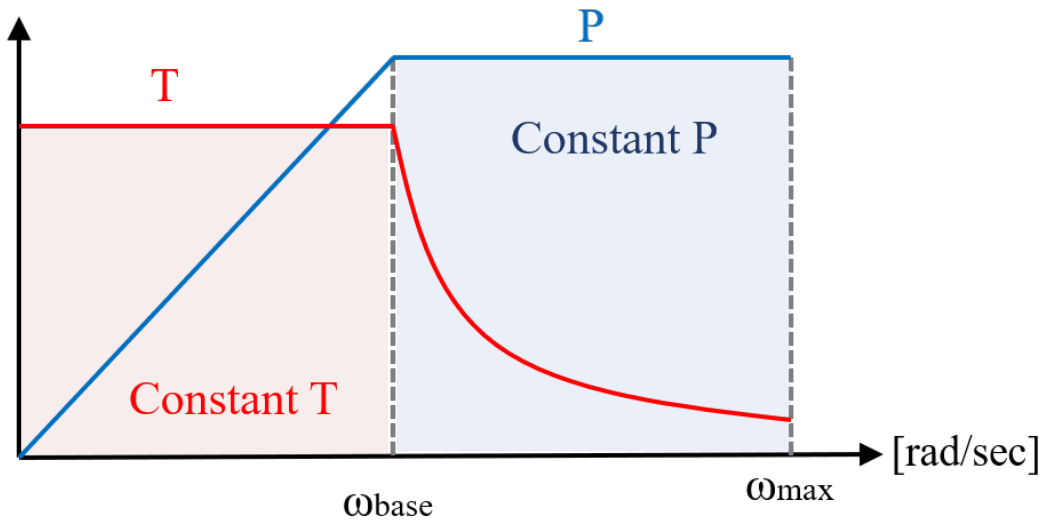

Figure 3.13: Torque-speed characteristic of SMs.

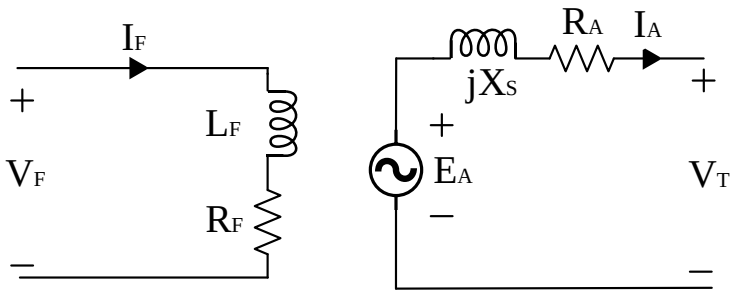

Figure 3.14: The electrical equivalent circuit representation of SMs

Therefore, in order to achieve the desired speed and torque references, the armature voltages should be controlled. The control block diagram of AC machines is presented in Fig. 3.15.

3.4.2 Proposed Modulation Technique

The armature's required voltage (magnitude, frequency, and angle) is found as in the previous part to achieve the desired speed and torque references.

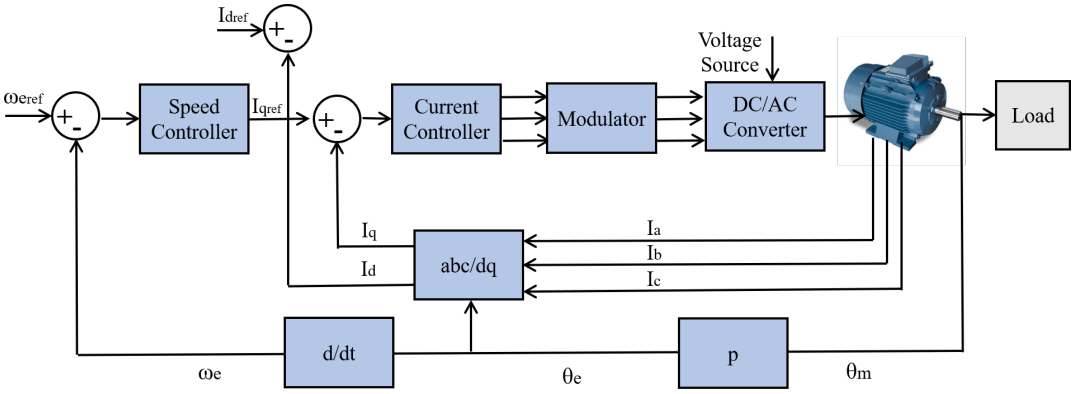

Figure 3.15: Control diagram of SMs.

These voltages can be produced using a 3-phase VSC, shown in Fig. 3.16, using PWM techniques such as sinusoidal-PWM (SPWM), space vector PWM (SVPWM), and discontinuous PWM (DPWM).

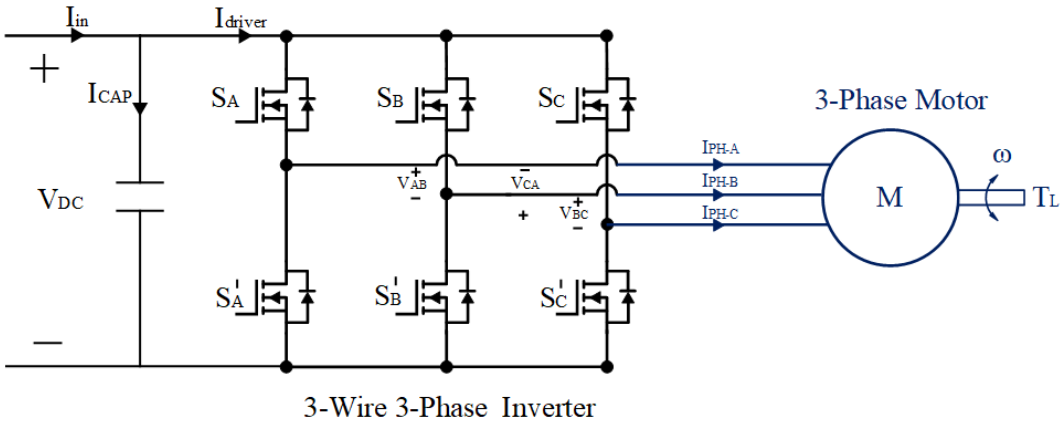

Figure 3.16: Circuit diagram of a 3-phase 3-wire inverter that drives a 3-phase motor.

SPWM, as proof of concept, will be analyzed analytically, but the principles can also be utilized for other modulation techniques. SPWM is established by comparing a high-frequency triangular carrier signal and a fundamental (modulating) signal. This fundamental signal is the reference signal of the motor, and the operating frequency of WPT is cultivated using the first harmonic of the carrier signal.

The analytical model of SPWM can be obtained as given in (3.9), using double Fourier analysis [56].

$$
\begin{aligned}
S = & \frac{1}{2} + \frac{m_a}{2}\cos\Big(\omega_o t + \theta_o\Big) \\
& + \frac{2}{\pi}\sum_{i=1}^{i=\infty} J_o\Big(i\frac{\pi}{2}m_a\Big)\sin\Big(i\frac{\pi}{2}\Big)\cos\Big(i(\omega_c t + \theta_c)\Big) \\
& + \frac{2}{\pi}\sum_{i=1}^{i=\infty}\sum_{k=-\infty}^{k=\infty}\begin{pmatrix} \frac{1}{i}J_k\Big(i\frac{\pi}{2}m_a\Big)\sin\Big((i+k)\frac{pi}{2}\Big) \\ \cos\Big(i(w_c t + \theta_c) + k(w_o t + \theta_o)\Big)\end{pmatrix}
\end{aligned}
\tag{3.9}
$$

There are four main components of the voltage of each leg: DC, fundamental, switching harmonics, and sidebands. The switching harmonics and their sidebands cannot be adjusted independently, and they change along with the modulation index, which linearly controls the magnitude of the fundamental frequency. Moreover, the phase angles of these components vary for each leg of the inverter, and they create positive, negative, or zero sequences, as shown in Table 3.1.

Table 3.1: The Sequences of Fundamental Frequency, Switching, and Its Sideband Harmonics for Inverter Legs

Frequency	**Leg A**	**Leg B**	**Leg C**	**Sequence**
$\mathrm{f_o}$	0^o	120^o	-120^o	Positive
$\mathrm{f_s} - 2\mathrm{f_o}$	0^o	120^o	-120^o	Positive
$\mathrm{f_s}$	0^o	0^o	0^o	Zero
$\mathrm{f_s} + 2\mathrm{f_o}$	0^o	-120^o	120^o	Negative

3.4.2.1 Control Methodology for the Proposed CSR

In the proposed system, a WPT system is connected to a 2-wire of the 3-phase 3-wire motor drive, as given in Fig. 3.17. The normalized line-to-line voltage harmonic distributions are given in Fig. 3.18 for different modulation indexes. Since the switching harmonic is zero-sequence for the conventional SPWM, the harmonic disappears in the line-to-line connection. Therefore, the line-to-line connected WPT system is excited only by the sideband components.

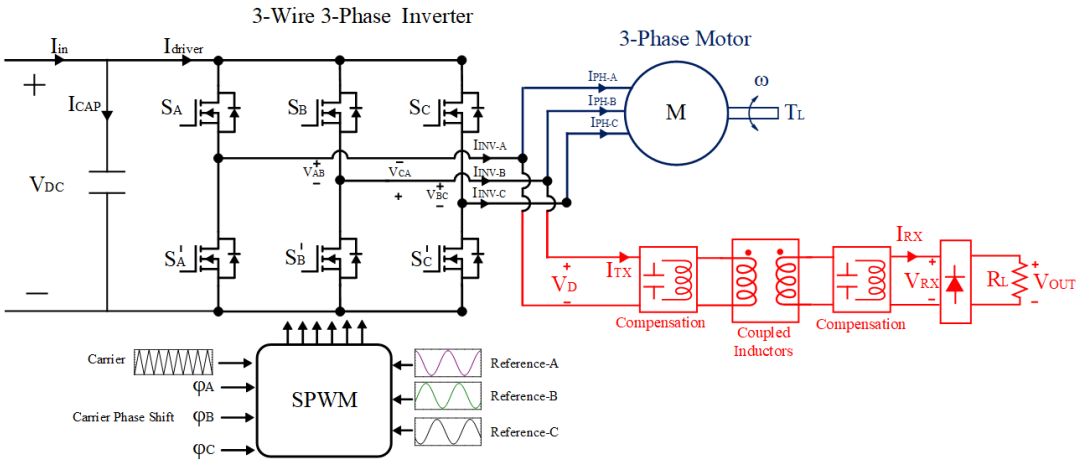

Figure 3.17: The circuit diagram of a single inverter system, which drives concurrently $3W$-3Φ motor and WPT system.

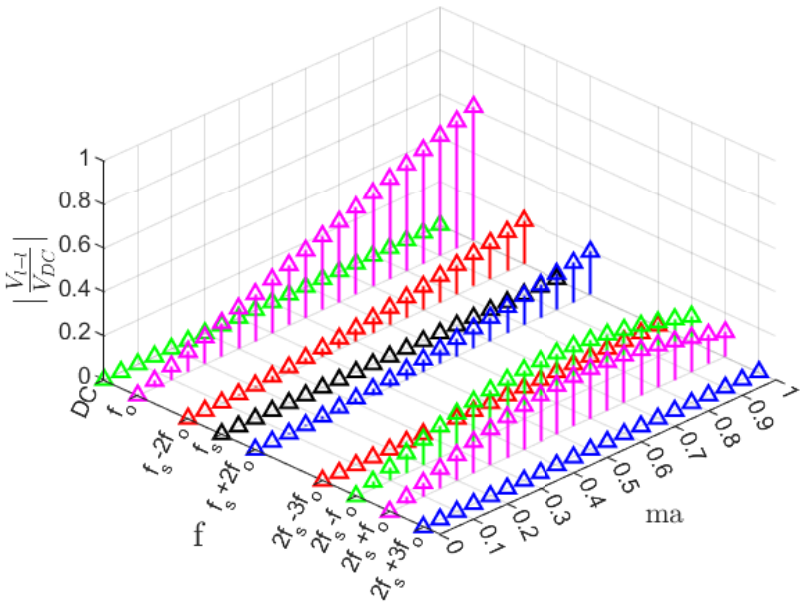

Figure 3.18: The harmonic distribution of a line-to-line voltage among different modulation indices without carrier phase shift.

However, the magnitude of these sideband components changes along with the modulation index, so the CSR can not guarantee continuous/constant power under various motor operations. This problem can be solved in different ways. Firstly, to regulate the WPT system's power, a post-regulation converter can be added to the receiver, but increasing cost and complexity. Secondly, frequency detuning can be applied like

DC motor drives. However, these methods cannot guarantee to transfer of power under each modulation index (m_a) since sideband components converge to zero as m_a comes up to 0. Lastly, it is proposed that this problem can be solved by giving a phase shift between carrier signals of two legs. As can be seen from the double Fourier analysis in (3.9), phase angles of switching frequency and sidebands change as a function of the phase angle of the carrier signal. In this study, for coherency, formulations will be made considering that the WPT system is connected between legs A and B, and a carrier-phase-shift (CPS) is given to leg B, as given in (3.10).

$$Carrier\ phases \begin{cases} \phi_{cA} = 0 \\ \phi_{cB} = \phi_{CPS} \\ \phi_{cC} = 0 \end{cases} \tag{3.10}$$

The magnitudes of switching frequency and sideband harmonics vary as given in (3.11, 3.12, 3.13). Thus, we can adjust the magnitude of each component by choosing a proper CPS.

$$V_{sl}(m_a) = \frac{2}{\pi} J_2\left(m_a \frac{\pi}{2}\right) \sqrt{1 - cos(\phi_{CPS} + 120^o)} \tag{3.11}$$

$$V_{s}(m_a) = \frac{2}{\pi} J_o\left(m_a \frac{\pi}{2}\right) \sqrt{1 - cos(\phi_{CPS})} \tag{3.12}$$

$$V_{sh}(m_a) = \frac{2}{\pi} J_2\left(m_a \frac{\pi}{2}\right) \sqrt{1 - cos(\phi_{CPS} - 120^o)} \tag{3.13}$$

These magnitudes can be plotted for variable carrier phase shifts and modulation indices, as shown in Fig. 3.19.

A challenge is to determine the amount of the CPS, which must guarantee a constant / continuous power transfer for any modulation indices. As shown in Fig. 3.19, while the magnitude of the switching frequency harmonic increases by increasing CPS, the magnitude of the sidebands decreases. Considering the quality factor of the WPT system, the gain of the switching frequency and its sideband harmonics are nearly equal since their frequencies are close enough. Instead of investigating each component in the time domain, we can build an equivalent drive voltage assuming all components to have the same frequency.

The RMS equivalent drive voltage (V_D) can be calculated by using (3.14) since all

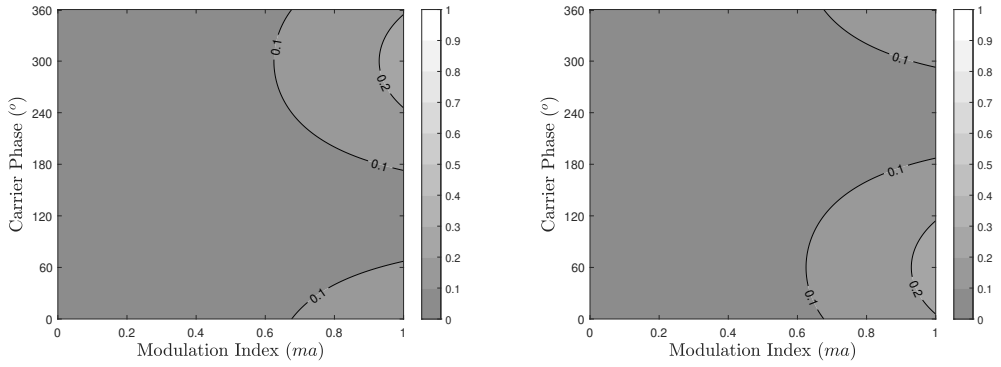

(a)

(b)

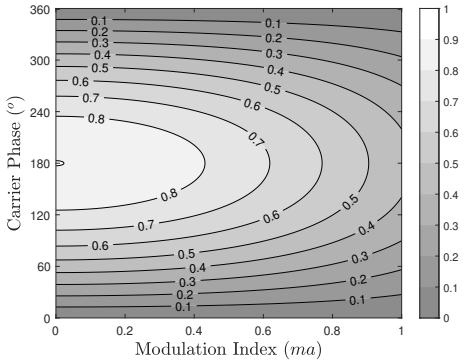

(c)

Figure 3.19: Normalized inverter ouput voltages $|\frac{V_{l-l}}{V_{DC}}|$. (a) Lower sideband of the switching frequency (f_{sl}). (b) Switching frequency (f_s). (c) Higher sideband of the switching frequency (f_{sh}).

these frequencies are orthogonal to each other.

$$V_D = \sqrt{\left(V_{sl}^2 + V_{sw}^2 + V_{sh}^2\right)} \tag{3.14}$$

Using the equivalent center harmonic approach, a normalized V_D is shown for various CPS and modulation indices in Fig. 3.20. As can be seen, for each m_a, we can guarantee the normalized gain between 0.25 and 0.45 by keeping the CPS between 30^o and 60^o. While the CPS is approaching 180^o, the normalized V_D increases.

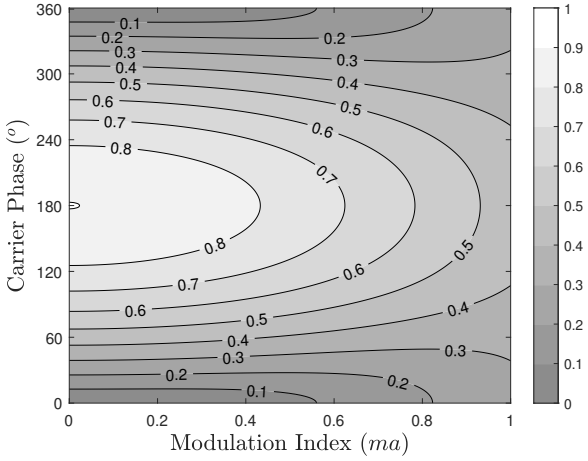

Figure 3.20: Normalized inverter output voltages $|\frac{V_{l-l}}{V_{DC}}|$ using the center harmonic approach.

However, at this point, we cannot fully control the voltage level; for example, the V_D acquired at $m_a = 0$ cannot be reached at $m_a = 1$. Consequently, the control diagram for the proposed system is given in Fig. 3.21. The motor controller decides on the modulation index, considering the desired speed and torque references. Then, the controller of the WPT system adjusts the CPS to achieve the desired CSR output power for these different motor operations.

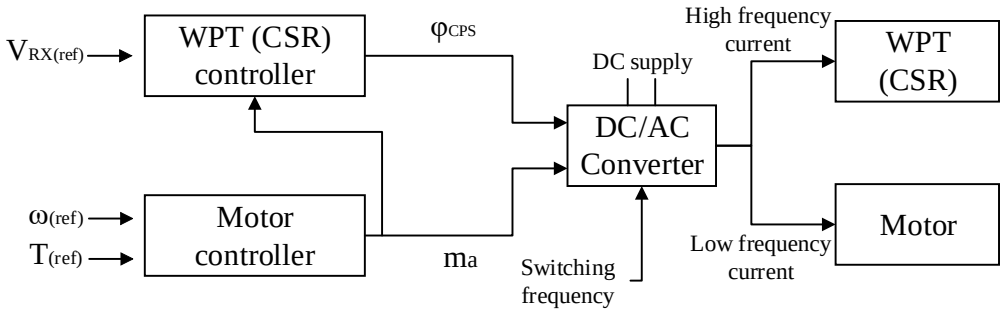

Figure 3.21: The block diagram of the control method of the combined motor and WPT system.

The key voltage and current waveforms without and with CPS are given in Fig. 3.22 and Fig. 3.23, respectively. While the fundamental signal is determined by modulating signals, the switching frequency and its sidebands are controlled by CPS.

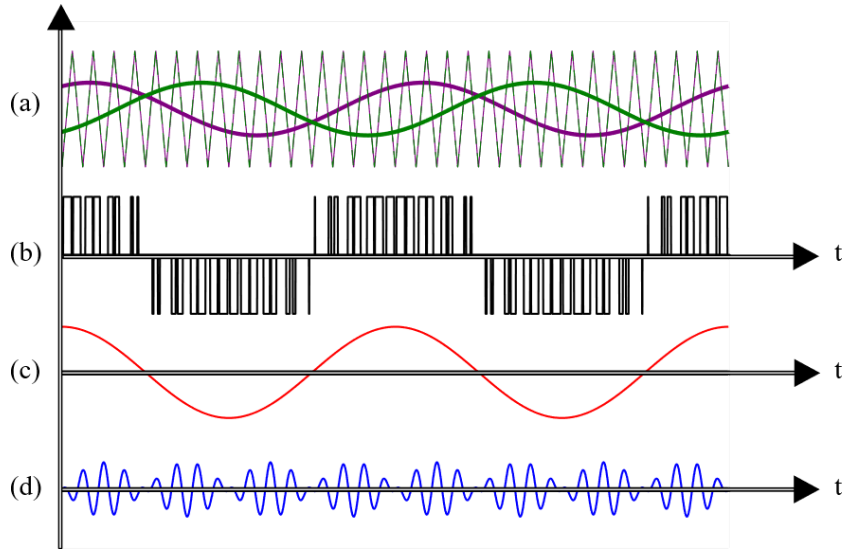

Figure 3.22: Key waveforms without CPS. (a) Ph-A (purple) and Ph-B(green) carrier triangles and sinusoidal references. (b) Line-to-line voltage of ph-A and ph-B (V_{AB}). (c) The waveform of fundamental frequency of (V_{AB}). (d) The waveform of the switching frequency and its sidebands of (V_{AB}).

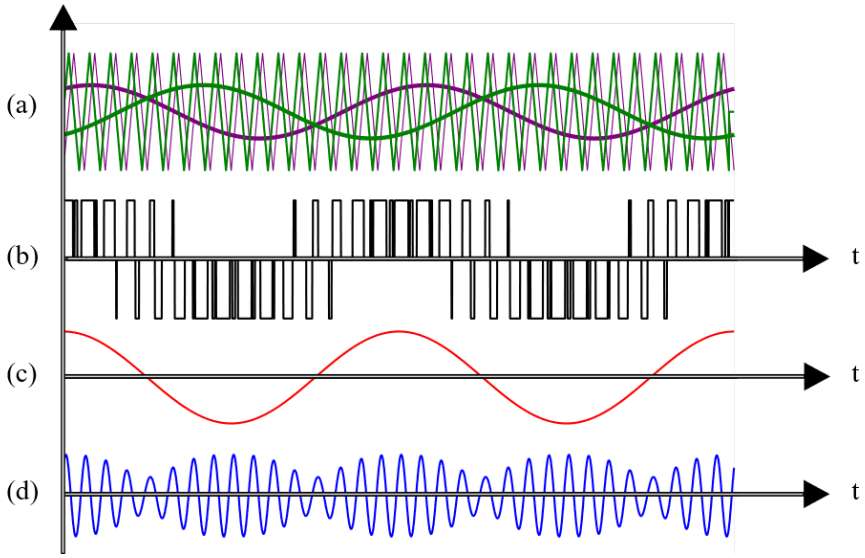

Figure 3.23: Key waveforms with CPS. (a) Ph-A (purple) and Ph-B(green) carrier triangles and sinusoidal references. (b) Line-to-line voltage of ph-A and ph-B (V_{AB}). (c) The waveform of fundamental frequency of (V_{AB}). (d) The waveform of the switching frequency and its sidebands of (V_{AB}).

3.5 Current Modulation Techniques of Conventional Drives

Many modulation techniques are utilized in industrial motor drives. While SPWM, SVPWM, and DPWM are prevalent for AC motor drives, unipolar-PWM and bipolar-PWM are prevailing for DC motor drives. Each modulation technique has its advantages. For example, while SVPWM effectively utilizes the DC link voltage, DPWM provides reduced switching losses [57]. Unipolar PWM has lower switching harmonics than bipolar PWM. Although the proposed system is implemented with bipolar PWM and SPWM, it can also be applied with other modulation techniques.

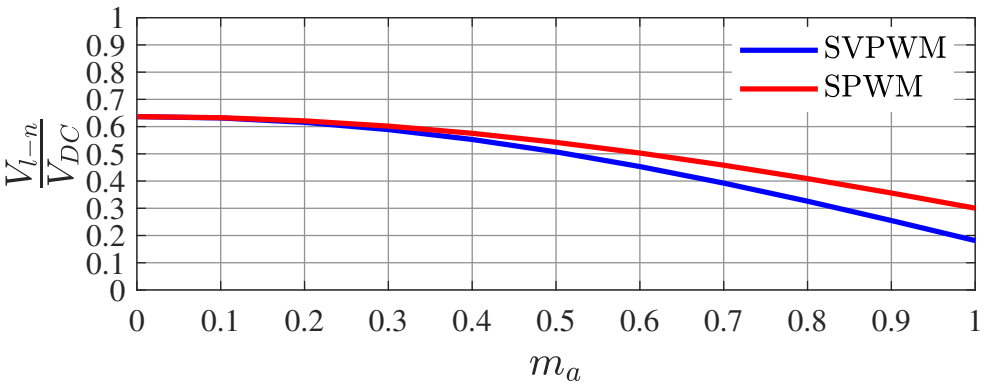

Figure 3.24: The normalized inverter voltage ($\frac{V_{l-n}}{V_{DC}}$) of the switching harmonics over modulation indexes (m_a).

For example, the change in the magnitude of the switching frequency over modulation indices is presented in Fig. 3.24 for SPWM and SVPWM. It is observed that the tendency of the magnitude of the switching harmonic of SVPWM is similar to SPWM, and it can be controlled by the proposed CPS method.

3.6 Practical Considerations

For conventional industrial motor drives, the switching frequency is usually below 20 kHz due to the switching losses of silicon (Si)-based transistors [58]. A WPT system is not feasible in this frequency range since the Tx-Rx coils get bulkier as the frequency is reduced [59]. The relation between the size of the coils and switching frequency is shown in Fig. 3.25. However, recent developments in semiconductor technology pave the way. Silicon Carbide (SiC) or Gallium Nitride (GaN) based motor drives [60, 61] reach higher switching frequencies (up to several hundred kHz), and they still provide high efficiency [62]. The switching frequencies and power capabilities of different semiconductor technology are given in Fig. 3.26.

Consequently, choosing a proper switching frequency is challenging since a high switching frequency increases the converter losses, and a low switching frequency increases the coil size and cost. With the development of wide band-gap devices, a sweet spot could be found, satisfying both requirements: higher efficiency and smaller coil sizes. Thus, it is now possible to utilize the wide band-gap motor drives as a single converter for concurrent operations. In the following chapters, the main considerations and design procedures will be presented in order to implement the proposed CSR with conventional GaN-based motor drives.

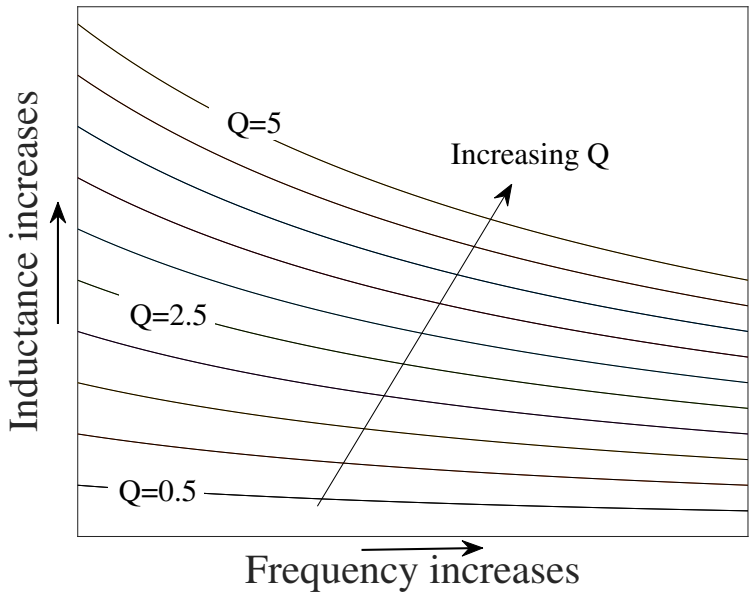

Figure 3.25: The change in Tx/Rx inductances for various switching frequencies and quality factors.

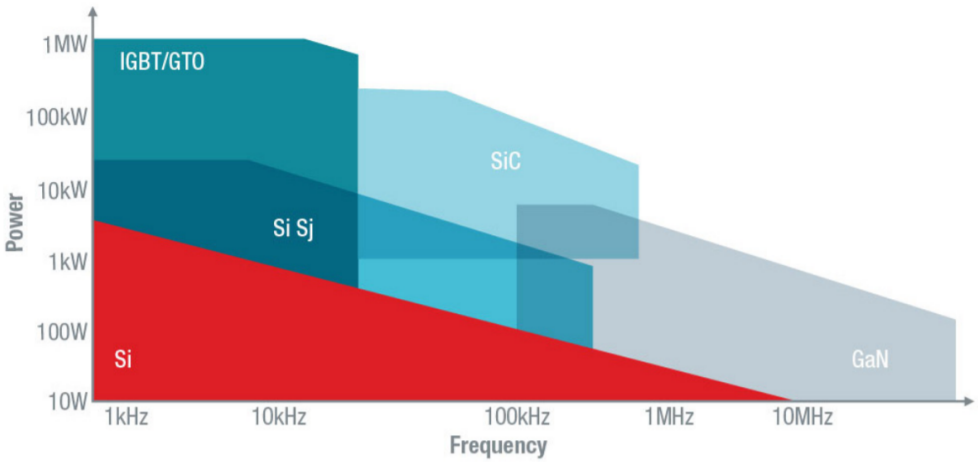

Figure 3.26: Switching frequency and power capabilities of the semiconductors for the converters [5].

CHAPTER 4

THE IMPLEMENTATION OF THE PROPOSED METHOD WITH DC MOTOR DRIVES

This chapter, as a proof-of-concept, investigates implementing the proposed contactless slip ring with a conventional DC motor drive used as a single converter. In the proposed system, reaching a higher switching frequency is significant to achieve a feasible size of the WPT coils, but it increases the drive's switching losses and operating temperature. Therefore, a wide band-gap-based motor drive, rather than its Si-based counterparts, is required to achieve a switching frequency that is a sweet operating point.

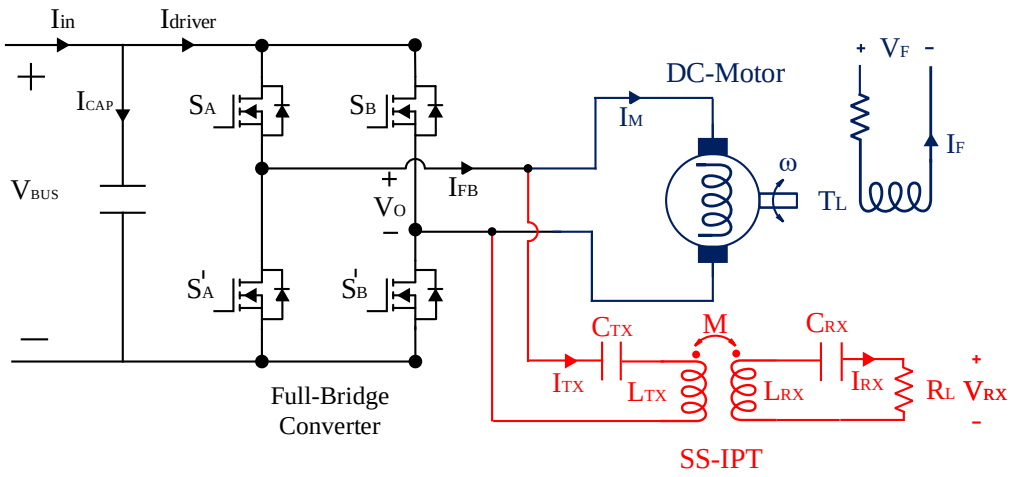

Figure 4.1: Circuit diagram of the proposed CSR system using a conventional motor drive as a single converter to transfer power concurrently.

In this study, a separately excited-DC motor with a GaN-based FB converter is used to implement the proposed CSR method. The electrical equivalent circuit diagram of the system is given in Fig. 4.1. In this motor drive, the bipolar PWM technique is utilized, and no control is applied to the motor's field winding (i.e. running it like a PM DC motor). Moreover, the power of the CSR is independently and concurrently controlled by detuning switching frequency, as mentioned in Chapter III.

4.1 System Design

In the setup, the DC-Bus voltage is selected as 100 V, where the DC motor's rated power reaches 500 W. The motor and drive parameters are presented in Table 4.1. In the next section, the WPT system will be designed systematically to drive the motor and the WPT system simultaneously.

Table 4.1: The Parameters of The Experimental Setup

The Rated Voltages and Powers	
Input Voltage (V_{BUS})	$100\ \mathrm{V_{DC}}$
IPT Output Voltage (V_{RX})	$20\ \mathrm{V_{RMS}}$
Motor Output Power (P_M)	500 W
IPT Output Power (P_o)	50 W

The Motor Parameters	
Armature resistance (R_a)	$2\ \Omega$
Armature inductance (L_a)	$7\ \mathrm{mH}$
Motor electrical time constant (T_s)	$3.5\ \mathrm{ms}$

The Drive Parameters	
Duty cycle(D)	$0.15 - 0.85$
Switching frequency (f_s)	$< 100\ \mathrm{kHz}$
Switching period (T_s)	$> 10\ \mu\mathrm{s}$

4.1.1 Motor Drive System

The motor drive consists of a GaN-based full-bridge converter, where this converter is described with details in [63]. The drive parameters are given in Table 4.1, and the experimental setup is shown in Fig. 5.7.

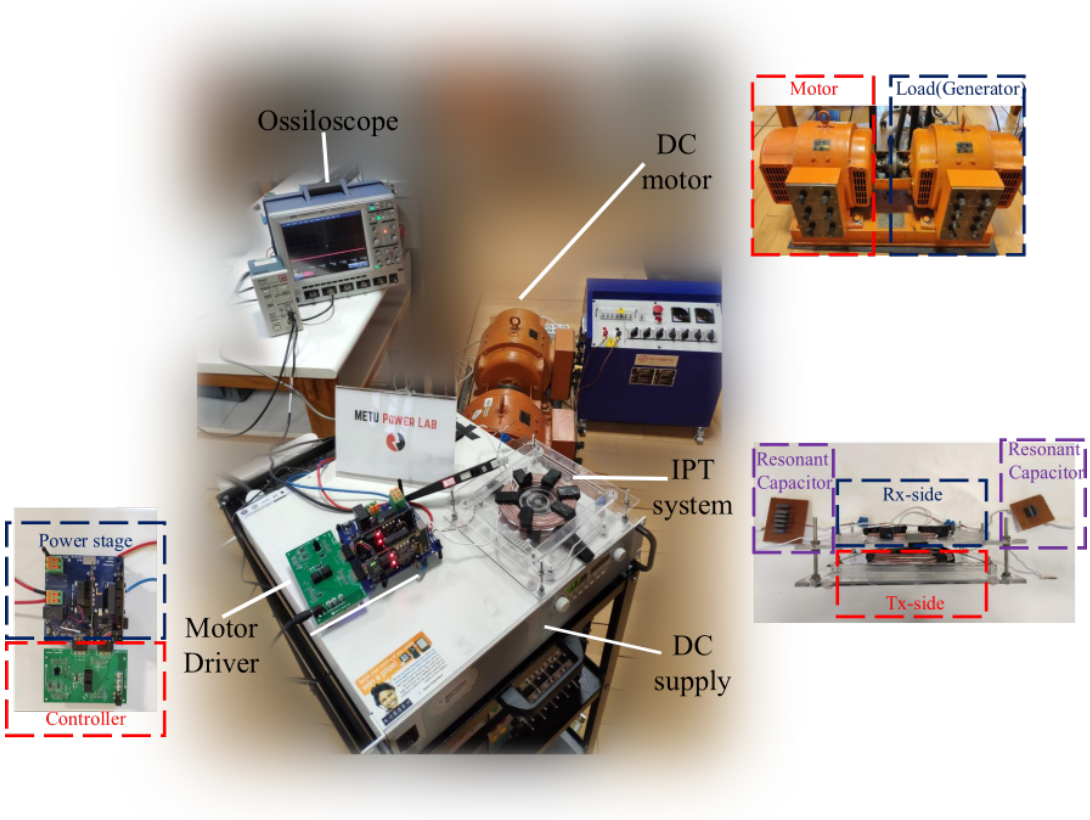

Figure 4.2: The illustration of experimental setup.

Although the motor drive allows a switching frequency up to 100 kHz, some considerations specify the lower and upper boundary of the switching frequency. In the aspect of motor drive, a higher switching frequency increases the drive losses, reducing the drive's lifetime, and a lower switching frequency increases the ripples of the motor current, which makes motor control challenging. In the aspect of the WPT system, increasing the switching frequency reduces the coil sizes but increases the coil losses. Therefore, a sweet operation point should be found that gives reasonable losses and feasible coil sizes.

4.1.2 The Design of Wireless Power Transfer System for the Proposed CSR

The rated output power of the WPT system is chosen as 50 W with 20 V output voltage under the given specifications in Table 4.1. Firstly, the topology is selected as a series-series IPT (SS-IPT) system, which allows a resonant frequency independent of loading and coupling. Since the motor and the WPT system share a single converter, a constant resonant frequency makes the control straightforward. For SS-IPT topology, in the bifurcation-free operation, the maximum gain is achieved at the resonant frequency. Then, the gain can be adjusted (decreased) by frequency detuning. Therefore, the resonant frequency is selected as 65 kHz, and the switching frequency can be increased up to 100 kHz to decrease the output power by frequency detuning.

In traditional WPT systems, a Tx coil is excited by a square wave voltage (D=0.5) produced using a full-bridge converter. The WPT system with chosen SS topology behaves like a band-pass filter and only allows the fundamental frequency of the square wave voltage to pass. Therefore, the excitation voltage of the Tx coil is calculated as in (4.1).

$$V_{o,1^{st}}(rms) = \frac{4}{\sqrt{2}\pi} V_{Bus} \tag{4.1}$$

However, in the proposed system, a single converter concurrently drives the motor and excites the Tx coil. In order to control the motor speed and torque, the duty cycle of bipolar-PWM varies. This duty cycle variation also results in the magnitude of the change in the fundamental frequency of the square wave; therefore, the excitation voltage of the Tx coil changes. The excitation voltage can be calculated by the Fourier series and formulated by the duty cycle as in (4.2).

$$V_{o,1^{st}}(rms) = \frac{4}{\sqrt{2}\pi} V_{Bus} sin(\pi D) \tag{4.2}$$

The WPT system should supply the desired output voltage under each duty cycle between 0.15 and 0.85 in the setup. In these duty cycles range, the first harmonic component of V_o varies between $40\ \mathrm{V_{RMS}}$ and $90\ \mathrm{V_{RMS}}$. Therefore, the design of the WPT system should be capable of delivering rated power over this wide range of input voltage. A systematic design will be performed for the minimum input voltage since the frequency detuning provides the ability to decrease power for higher input voltages [38].

Firstly, the Rx inductance can be calculated by using (4.3) where ω_o is the resonant frequency in radian per second, and Q_{RX} is the quality factor, R_L is the load resistance.

$$\mathrm{L_{RX}} = \frac{\mathrm{Q_{RX}R_L}}{\omega_\mathrm{o}} \tag{4.3}$$

Q_{RX} should be between 2-10 as a rule of thumb [38, 64]. The higher Q_{RX} increases the size of the Rx coil but decreases the size of the Tx coil. Moreover, the mutual inductance can be calculated using (4.4) where $V_{o,1^{st}}$ is the first switching harmonic component of V_o.

$$\mathrm{M} = \frac{\mathrm{V_{RX}V_{o,1^{st}}}}{\mathrm{P_o}\omega_\mathrm{o}} \tag{4.4}$$

The inductance of the Tx coil can be found using (4.5). The coupling coefficient (k) varies between 0 and 1.

$$\mathrm{L_{TX}} = \frac{\mathrm{V^2_{o,1^{st}}}}{\mathrm{k^2}\omega_\mathrm{o}^2\mathrm{Q_{RX}}} \tag{4.5}$$

Finally, the capacitance values can be achieved using (4.6).

$$\mathrm{C_{TX,RX}} = \frac{1}{\mathrm{L_{TX,RX}}}\omega_\mathrm{o}^2 \tag{4.6}$$

The selection of k and Q_{RX} changes the gain characteristics of the WPT system. In regular WPT systems, the Tx and Rx coils are usually loosely coupled since lower k avoids bifurcation and guarantees zero voltage switching (ZVS) above the resonant frequency. However, in the proposed system, the WPT system is used to energize auxiliary loads; therefore, the motor current is dominant in the converter current. Thus, ZVS may already not be achieved even if the system is not in bifurcation and operates above the resonant frequency (The ZVS conditions will be analyzed later in the chapter). Hence, a bifurcation-free design is not aimed, and k should be increased to reduce the Tx coil inductance and size, as shown in Fig. 4.3.a Besides, the variations of Tx and Rx inductances as a function of Q_{RX} are shown in Fig. 4.3.b. Higher Q_{RX} increases the inductance of the Rx coil and decreases the inductance of Tx coil for a constant k. However, Q_{RX} and k also affect the gain-frequency characteristics, as shown in Fig. 4.3.c. Considering all the above, Q_{RX} and k are selected as 2.6 and 0.40 in the finalized design, which parameters are presented in Table 4.2.

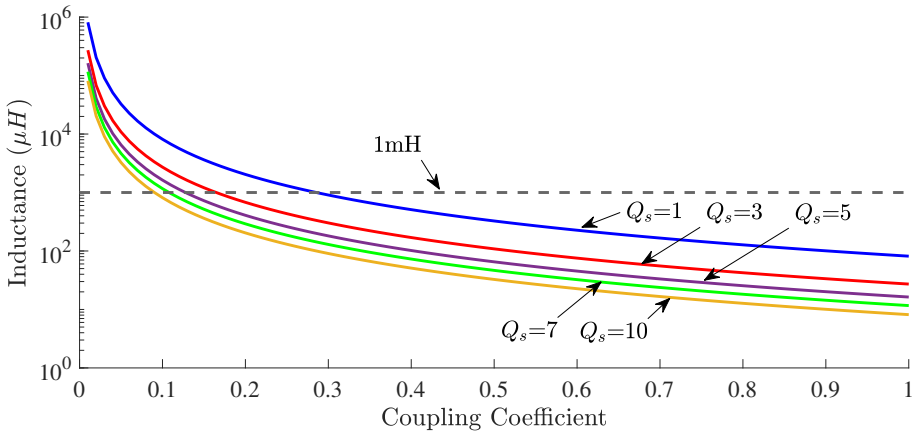

(a) The inductance of the Tx coil as a function of k.

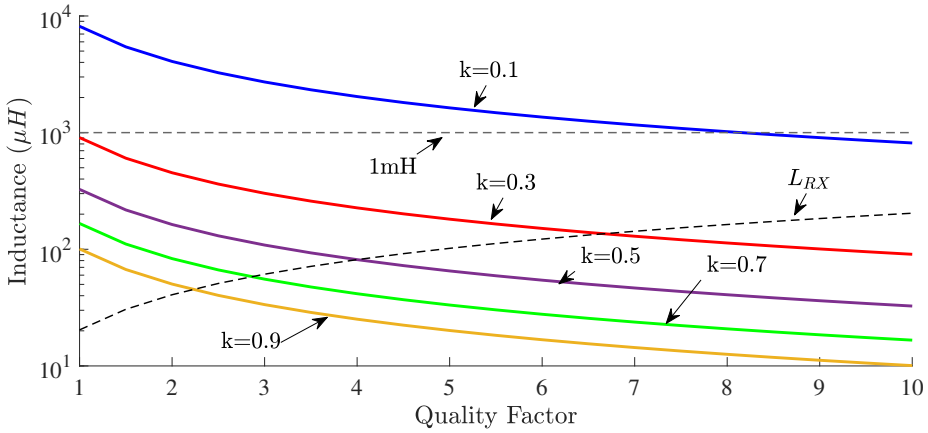

(b) The inductance of the Tx and Rx coils as a function of Q_{RX}.

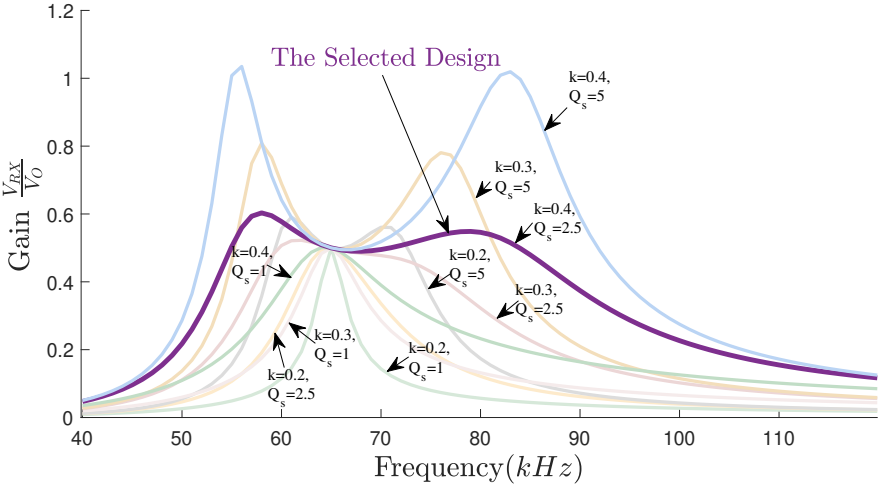

(c) The gain-frequency characteristic of several k and Q_{RX}.

Figure 4.3: Effect of the design parameters on Tx coil, Rx coil and gain of the WPT system.

Table 4.2: Parameters of the WPT System.

Receiver quality factor (Q_{RX})	2.6
Resonant frequency (f_0)	65 kHz
Coupling factor (k)	0.40
Load resistance (R_L)	8 Ω
Receiver coil inductance (L_{RX})	51 μH
Mutual inductance (M)	41 μH
Transmitter coil inductance (L_{TX})	205 μH
Receiver resonant capacitance (C_{TX})	115 nF
Transmitter resonant capacitance (C_{RX})	29 nF
Voltage gain at f_o	0.5

4.2 Coil Design

Although regular WPT systems use various coil shapes such as DD pads, DD-Q pads [65, 66, 67, 68], coils having rotational symmetry are preffered in CSR applications [23, 24, 69]. Thus, the coupling change in a full rotation, which may decrease the system's efficiency, can be minimized. In general, for CSR applications, there are two main coil shapes: coaxial and face-to-face [6, 70], which are shown in Fig. 4.4.

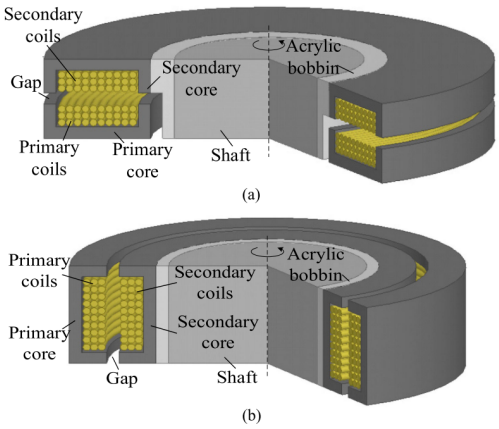

Figure 4.4: Coil shapes [6]. (a) Face-to-face coils. (b) Coaxial coils.

Both coils can be mounted around the shaft of the motor. Due to the magnetic flux leakage, eddy losses exist on the shaft, made of electrically conductive material. Therefore, ferrite strips are placed around the coils to decrease the leakage flux and increase the couplings between Tx/Rx coils. However, in the proposed system, the amount of the ferrite strips can be reduced to decrease the weight of the rotating frame since the magnetic field is low, and the eddy losses on the shaft can be ignored. On the one hand, in coaxial coils, the arrangement of the airgap is challenging. The air gap cannot be changed after the manufacturing process; thus, tuning the coupling is difficult. On the other hand, in face-to-face coils, the air gap can be adjusted after the manufacturing process, implying that the coupling can be fine-tuned. In this study, it is preferred a face-to-face circular coil shape thanks to its airgap flexibility and easy manufacturing. The finite element (FE) simulations are presented in Fig. 4.5. The coils' diameters, turns, and airgap are also given in Table 4.3.

Table 4.3: The simulated results and found parameters of face-to-face Tx/Rx coils.

Tx-coil inner diameter	52 mm
Tx-coil outer diameter	110.6 mm
Tx number of layer	3
Tx conductor diameter	2 mm
Tx-coil total turns/turns per layer	44/15
Rx-coil inner diameter	80 mm
Rx-coil outer diameter	148 mm
Rx conductor diameter	2 mm
Rx-Coil total turns/turns per layer	17/17
Airgap	20 mm
Tx-coil inductance	204 μH
Rx-coil inductance	52 μH
Mutual inductance	41 μH

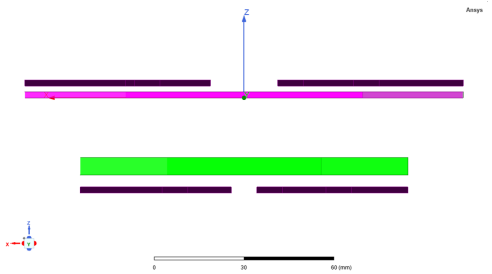

(a) The sideview of the designed face-to-face IPT coils.

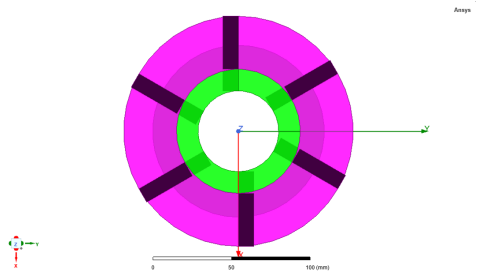

(b) The topview of the designed face-to-face IPT coils.

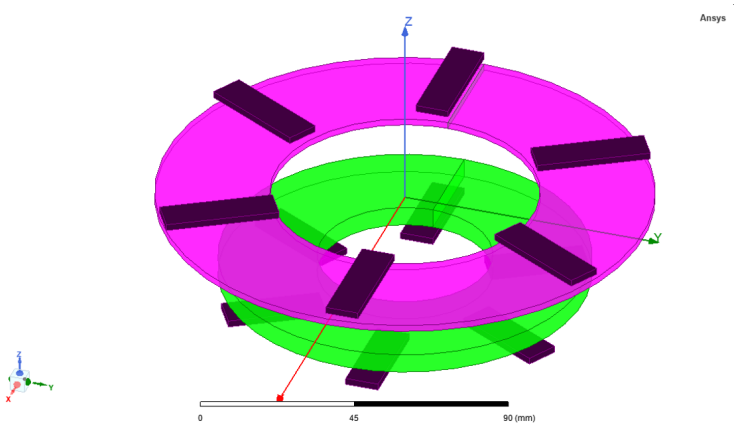

(c) The isometric view of the designed face-to-face IPT coils.

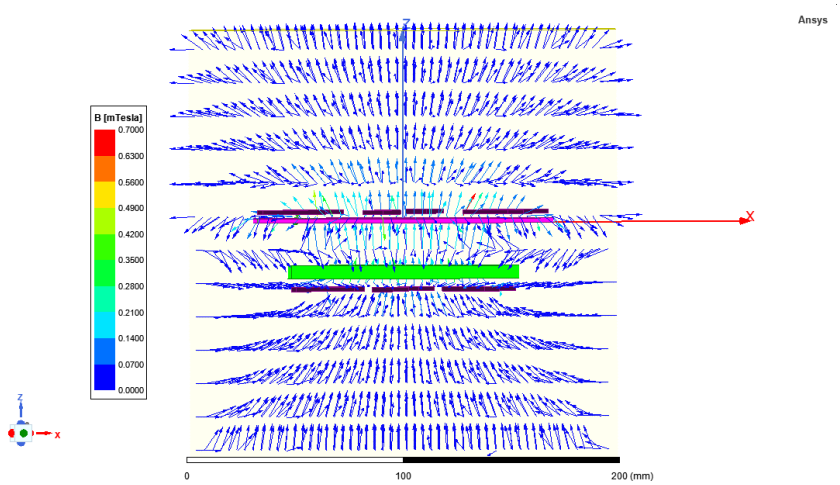

(d) The magnetic flux density vectors.

Figure 4.5: The FE model of the designed WPT coils. Green-coloured and pink-colored coils belong to the Tx and Rx, respectively. Ferrite strips are black.

4.3 Impedance Modelling and Decoupled Control of The Combined Motor and WPT system

The impedance modeling of the proposed CSR technique is shown in Fig. 4.6. The converter is modeled as a pulsating voltage source, and lumped parameters are used to model the WPT system and the motor.

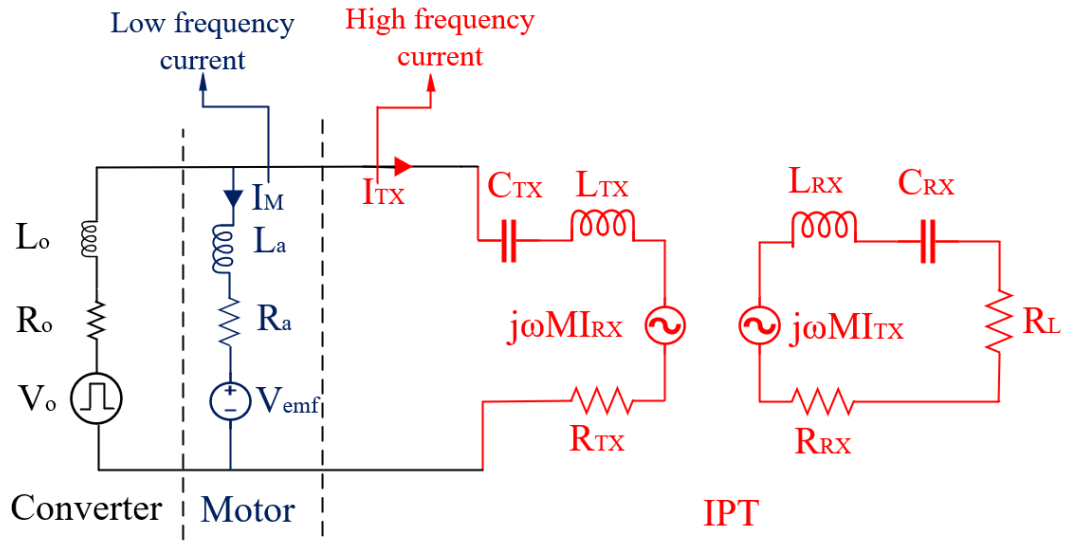

Figure 4.6: The impedance model of the proposed CSR system.

Input impedances of the motor and the WPT system are formulated as in (4.7) and (4.8). Then, the calculated impedances for the exemplified setup are plotted in Fig. 4.7.

$$Z_{in-M} = j\omega L_a + R_a \tag{4.7}$$

$$\begin{aligned} Z_{in-IPT} =& j\omega L_{TX} + \frac{1}{j\omega C_{TX}} + R_{TX} \\ &+ \frac{\omega^2 M^2}{j\omega L_{RX} + \frac{1}{j\omega C_{RX}} + R_L + R_{RX}} \end{aligned} \tag{4.8}$$

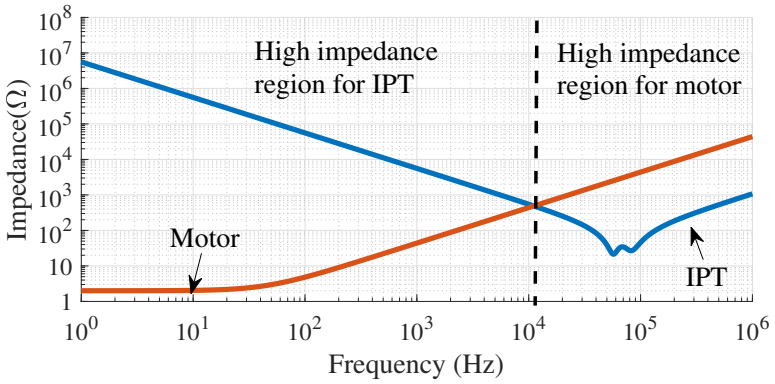

Figure 4.7: Frequency response of the motor windings and the WPT coils.

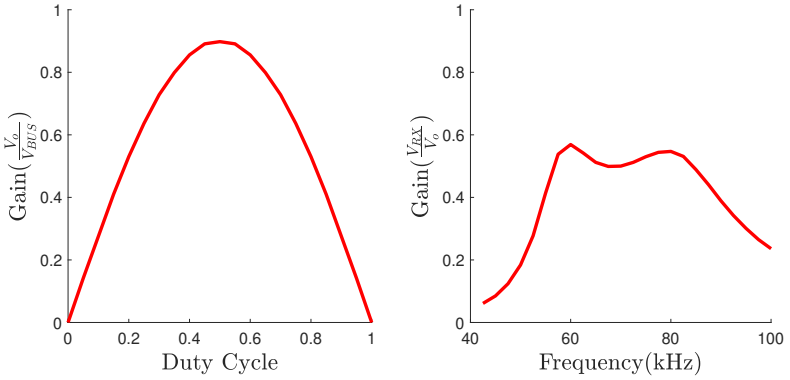

(a) Duty cycle-gain characteristic of IPT at 80 kHz.

(b) Frequency-gain characteristic of WPT ($D = 0.5$).

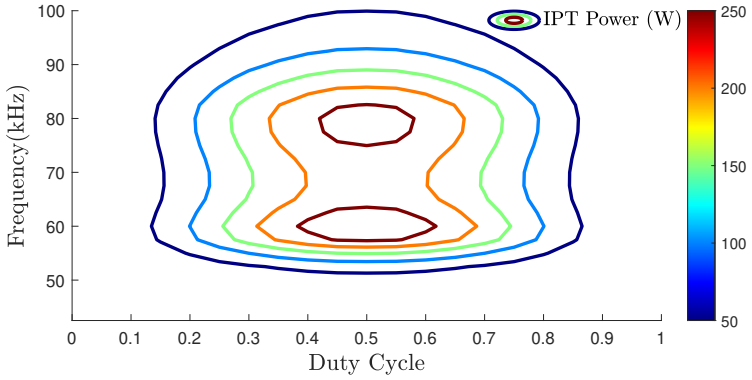

(c) The iso-power lines of WPT through duty cycle and frequency.

Figure 4.8: Simulation results of WPT voltage gain and power as a function of duty cycle and frequency.

V_o is a square wave consisting of voltage components of DC and switching harmonics. On the one hand, the WPT system behaves like band-pass filters, where only frequencies near the switching frequency pass and other components attenuate. On the other hand, the motor is like a low-pass filter; thus, the switching harmonics are filtered out, and only DC passes. Consequently, while the motor operates at DC, the WPT operates at the switching frequency. Thus, controls of the motor and the WPT system can be decoupled as they behave like high-impedance loads at each other's operating frequencies.

The switching frequency only affects the ripples of the motor's current, and the DC component is adjusted by varying the duty cycle. However, this varying duty cycle also changes the magnitude of the switching harmonics' component, so the WPT system's output voltage alters, as shown in Fig. 4.8.a. For this reason, the output voltage should be adjusted by switching frequency to supply constant/continuous power, and the frequency response of the WPT system is shown in Fig. 4.8.b The WPT system's output power is plotted for different duty cycles and switching frequencies in Fig. 4.8.c. Accordingly, the output power can be kept constant by appropriately controlling the switching frequency under any motor operations (or duty cycles).

4.4 Experimental Results

The setup is established to validate the proposed system, as shown before in Fig. 5.7. A separately excited DC motor is driven by a GaN-based full-bridge converter, which concurrently excites the WPT system.

4.4.1 The WPT System Validation

Tx-Rx coils were wound, and measured inductances are given in Table 4.4. The system's gain-frequency and gain-duty cycle characteristics were compared with simulation results. In Fig. 4.9, the experimental results are coherent with the simulation results.

Table 4.4: Parameters of the SS-IPT System

	Design values	Measured values
Transmitter inductance	204μH	205μH
Receiver inductance	52μH	51μH
Mutual inductance	41μH	40μH

4.4.2 Stand-alone and Concurrent Operation of the Motor and the WPT System

Firstly, only the WPT system was connected to the converter. The operation point is selected as f_{sw} = 81.3 kHz and D=0.85 to transfer 54 W with 20.8 V. V_{RX}, V_o, I_{TX} are shown in Fig. 4.10.a Secondly, only the motor was connected to the converter with the same duty cycle and switching frequency. The converter delivers 480 W to the motor. The V_o and I_M are presented in Fig. 4.10.b. Finally, they both were connected to the converter to show their concurrent operation. V_{RX}, I_M, V_o, and I_{TX} are given in Fig. 4.10.c. Accordingly, it was observed that the motor and WPT system concurrently operate without disturbing each other.

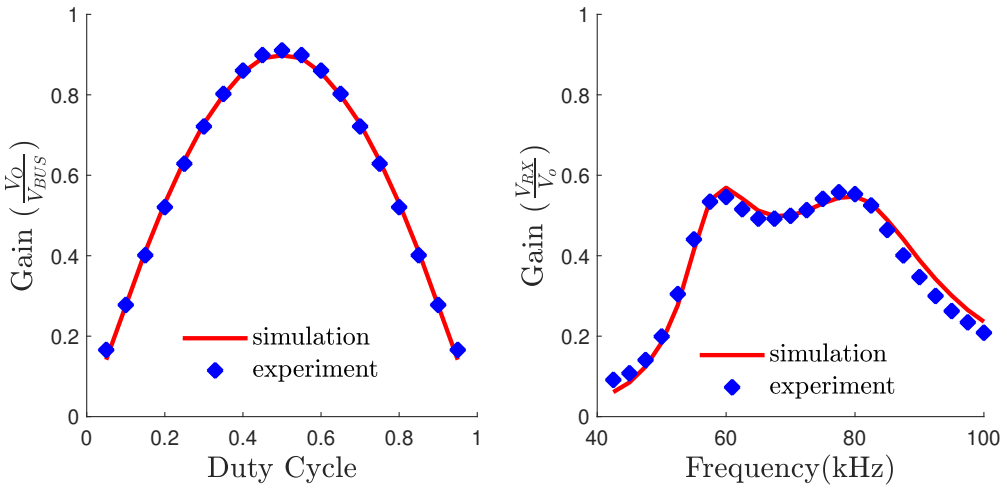

(a) Duty cycle-gain characteristic of WPT at 80 kHz. (b) Frequency-gain characteristic of WPT ($D = 0.5$).

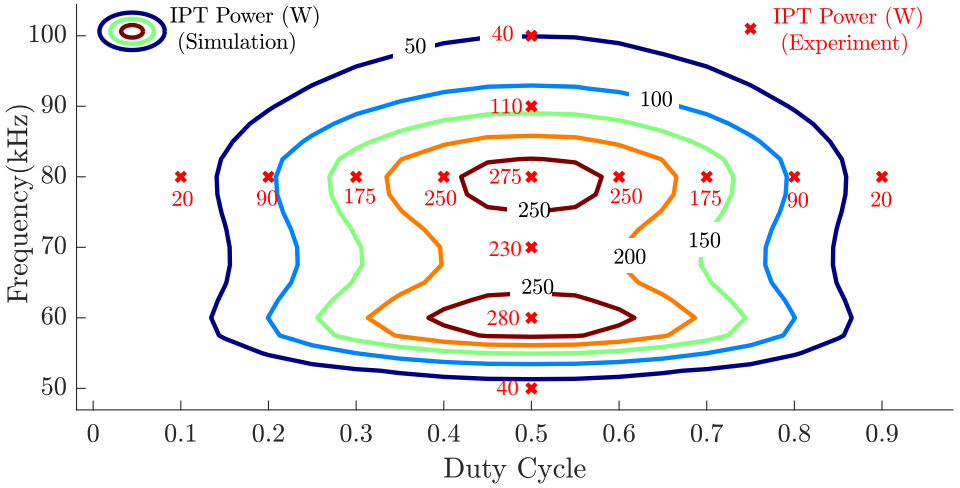

(c) The iso-power lines of WPT system output power along with the duty cycle and the switching frequency.

Figure 4.9: Simulation and experimental results of WPT voltage gain and power as a function of the duty cycle and the switching frequency.

4.4.3 Loss and Efficiency Measurements

Since the motor drive is used as a single converter, the high-frequency current of the WPT system creates additional losses, which may cause thermal stress on the drive. Thus, the effect of the proposed system on drive losses needs to be examined, but it is challenging to measure the additional loss components with electrical methods.

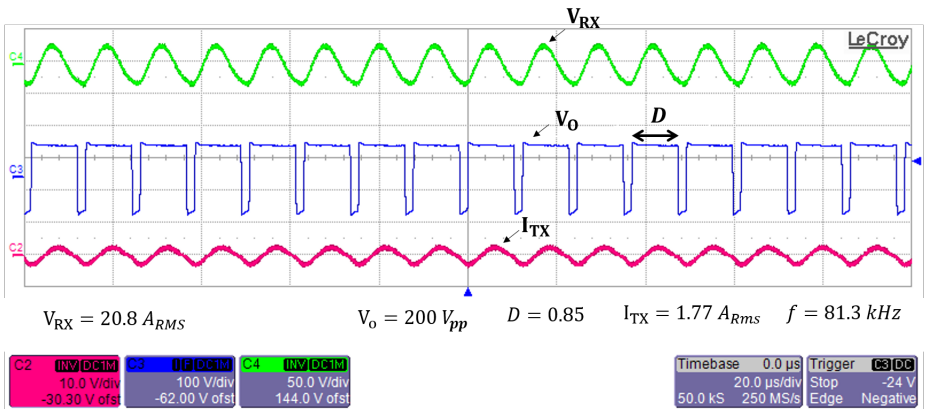

(a) I_{TX}, V_{RX} and V_o for single WPT system operation.

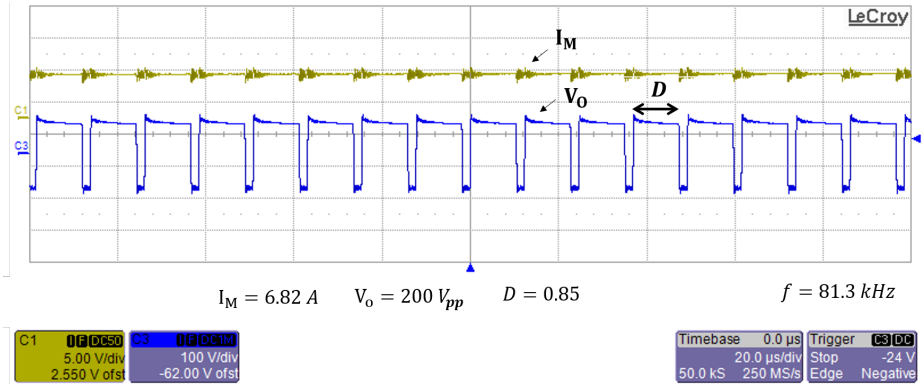

(b) I_M and V_o for single motor operation.

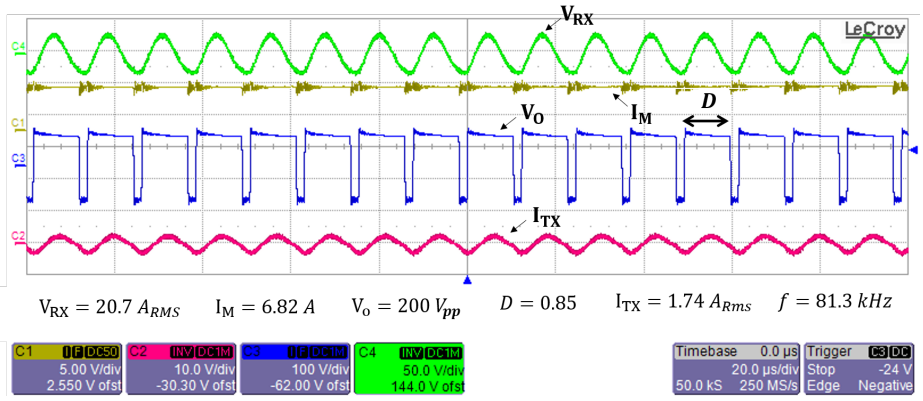

(c) I_{TX}, I_M ,V_{RX} and V_o for simultaneous the WPT system and the motor operations.

Figure 4.10: Experimental results of the concurrent operation of the proposed system. a) 67.6 W input power at operating frequency of 81.3 kHz. b) 457 W input power at operating frequency of 81.3 kHz. c) 522.2 W input power at operating frequency of 81.3 kHz.

Therefore, a calorimeter setup was established, which is explained in detail in [71]. The input powers, driver losses, converter output powers, and efficiencies for stand-alone and concurrent operations were measured, as given in Table 4.5.

Table 4.5: Experimental Results of the Converter's Loss and Efficiency Analysis with a Calorimeter

Operation	**Input Power (W)**	**Drive Losses (W)**	**Converter Ouput Power (W)**	**Efficiency (%)**
Only IPT	67.6	7.3	60.3	89.2
Only Motor	457.1	12.8	444.3	97.2
IPT and Motor	522.2	14.1	508.1	97.3

The drive losses of concurrent operation increase only 10% compared to the only motor operation. The motor drives usually have already been slightly over-designed to stay safe operation. Therefore, the 10% increase is thermally manageable.

4.4.4 The Effect of Transient Load Variations

The effect of transient load changes is investigated under the constant switching frequency and duty cycles. The motor and Rx currents are shown in Fig.4.11, and responses will be explained for each time interval as follows:

- $t_0 - t_1$: The motor is loaded with 105 W (I_m =1.9 A), and the WPT system transmits 35 W (I_{RX} =1.7 A_{RMS}).
- t_1: The power of the motor raises to 171 W.
- $t_1 - t_2$: I_m reaches to 2.9 A while I_{RX} is constant at 1.7 A_{RMS}.
- t_2: The power of the motor reduces to 105 W.
- $t_2 - t_3$: I_m reduces to 1.9 A while I_{RX} is constant at 1.7 A_{RMS}.
- t_3: The WPT system power increases to 63 W.

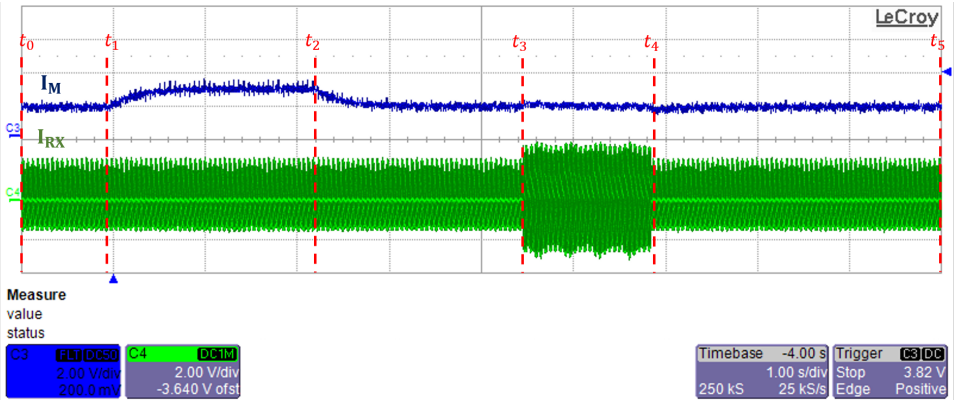

Figure 4.11: Experiment results for transient load variations of the motor and the WPT system.

- $t_3 - t_4$: While I_m is kept constant at 1.9 A, I_{RX} increases to 2.4 A_{RMS}.
- t_4: The WPT power decreases to 35 W.
- $t_4 - t_5$: While I_m is constant at 1.9 A, I_{RX} reduces to 1.7 A_{RMS}.

The transient load changes do not affect the steady-state operation of the motor and WPT system. However, it was observed that the motor is affected transitory where the current slightly changes (by a 5% overshoot or undershoot). Then, it reaches the expected steady-state value in a short time as expected. Therefore, these tests prove the independent and concurrent operation of the motor and WPT system.

4.4.5 Tests Under Different Operating Conditions

The proposed method was tested under seven distinct operation points to validate the concurrent power transfer and independent control. The duty cycles and switching frequency were adjusted to achieve the desired power of the motor and the WPT system. The duty cycles and switching frequency of each operation are given in Table 4.6.

The output power of the WPT system can stay constant by frequency detuning, whereas the duty cycle controls the motor power. These transitions were tested, as shown in Fig 4.12 in transitions from operating conditions of A to B (or C to D). Then, it was

Table 4.6: Concurrent Operation of the proposed CSR system and the Motor under Different Operating Conditions.

	Cases						
	A	**B**	**C**	**D**	**E**	**F**	**G**
Frequency (kHz)	95	90	90	95	90	90	97.5
Duty Cycle	0.6	0.75	0.75	0.6	0.6	0.6	0.5
Load Torque (N.m)	0.24	0.27	0.37	0.21	0.21	0.17	-
Motor Power (W)	125	179	244	109	110	89	-
IPT Power (W)	50	51	51	50	90	90	52.7

- : The load torque and motor power do not exist due to the motor speed being zero at $D = 0.5$.

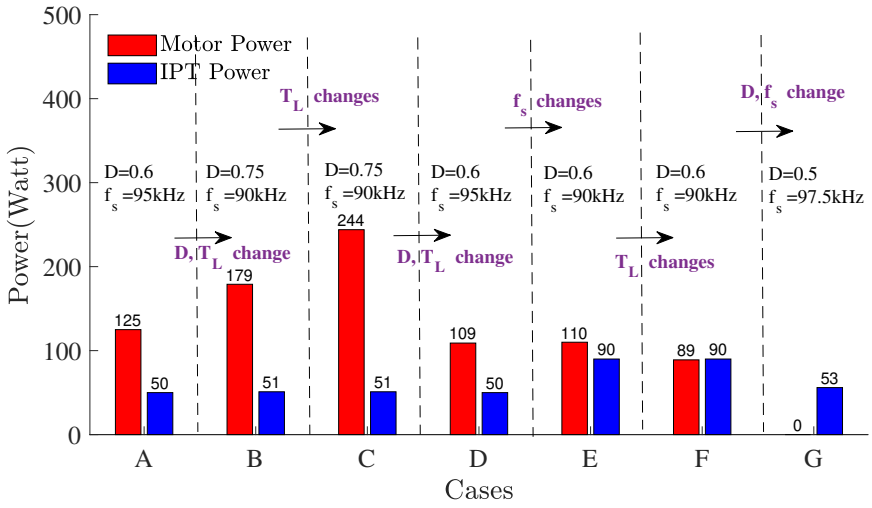

Figure 4.12: The motor power and transmitted WPT-CSR power for different operating conditions.

observed that the power of the WPT system stays the same for a constant duty cycle and switching frequency, while the motor's load torque changes, as shown in transitions of B to C (or E to F). After that, it was acquired that the motor operation does not affect by the switching frequency that controls the power of the WPT system, as given in cases D to E transition. Lastly, even if the motor stops, it was obtained

that the WPT system still delivers the desired output power using frequency detuning, as given in cases F to G transition. To conclude, using frequency detuning control, the power of the proposed CSR can deliver the rated output power under any motor operation.

4.5 Discussion on the Soft-switching Conditions

The high-frequency current drawn by the WPT system can affect the switch stress. They create additional losses, divided into two main parts: conduction and switching losses. The additional stress due to the conduction losses is negligible since the RMS value of the WPT system's current is less than the motor current. However, the effect of the high-frequency current on the switching conditions should be investigated. The equivalent circuit schematic of the motor drive is given in Fig. 4.13. The motor can be considered as a constant current source or inductive load. If the load current is positive, the drain-source capacitors (of SA' and SB) discharge during the dead time, and SA' and SB make zero voltage switching (ZVS) at the turn-on. In the same way, if the load current is negative, SA and SB' make ZVS. Therefore, in a DC motor drive, two of four switches always make ZVS.

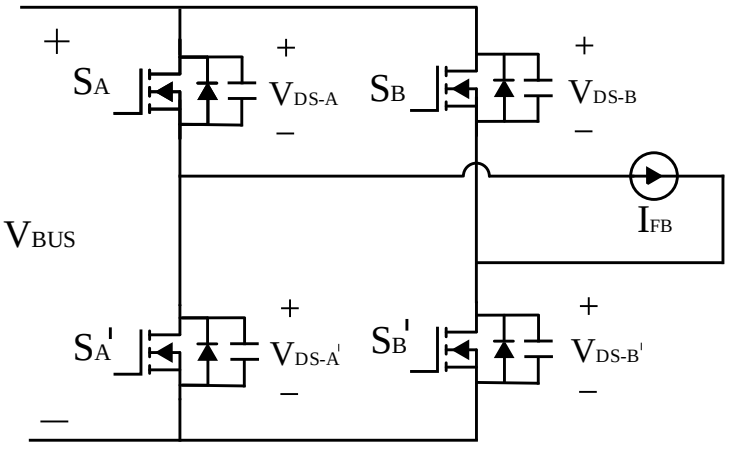

Figure 4.13: The circuit diagram of FB converter with inductive load.

However, the addition of the WPT system's high-frequency current may alter the current's direction or increase/decrease the converter current at the switching time. Therefore, the ZVS conditions may change, and it should be investigated considering the high-frequency current. There are two main situations: the peak current of the Tx coil ($\hat{I}_{TX}$) is greater or less than the motor current (I_M).

4.5.1 The motor current is greater than the peak current of the Tx coil ($I_M > \hat{I}_{TX}$)

When the I_M is greater than $\hat{I}_{TX}$, the converter current's direction does not alter. Therefore, in this condition, two of four switches still make ZVS like in only motor operation. In order to observe the ZVS conditions, gate-source and drain-source voltage are given for leg A and the positive motor current. Thus, SA (and so S_B) make ZVS.

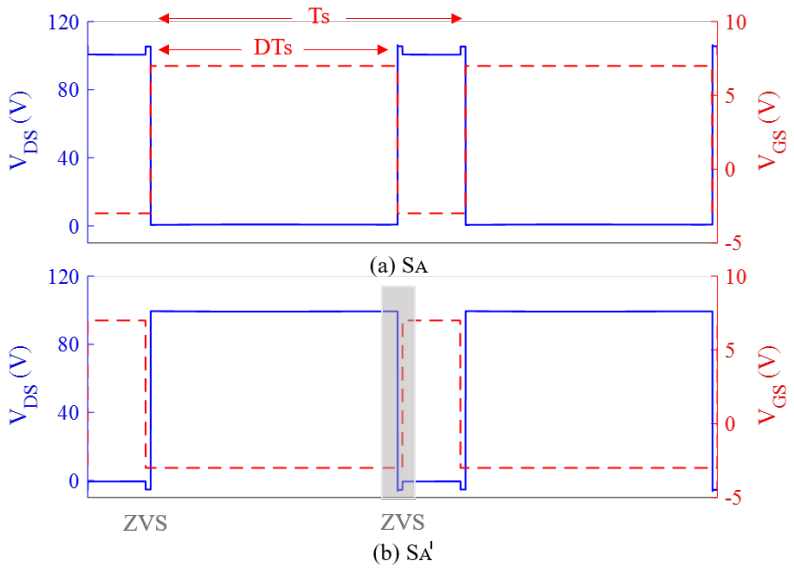

Figure 4.14: Drain-source and gate-source voltage waveforms at $D = 0.8$ and $f = 80kHz$ for dominant motor current conditions. ZVS regions are colored in gray.

4.5.2 The motor current is less than the peak current of the Tx coil ($I_M < \hat{I}_{TX}$)

When the $\hat{I}_{TX}$ is greater than I_M, the converter current's direction alters in a switching period. This condition behaves like the operation of a regular WPT system, and all switches may make ZVS at turn-on transition. An example of the ZVS condition is presented in Fig. 4.15 for S_A and $S_{A'}$ switches.

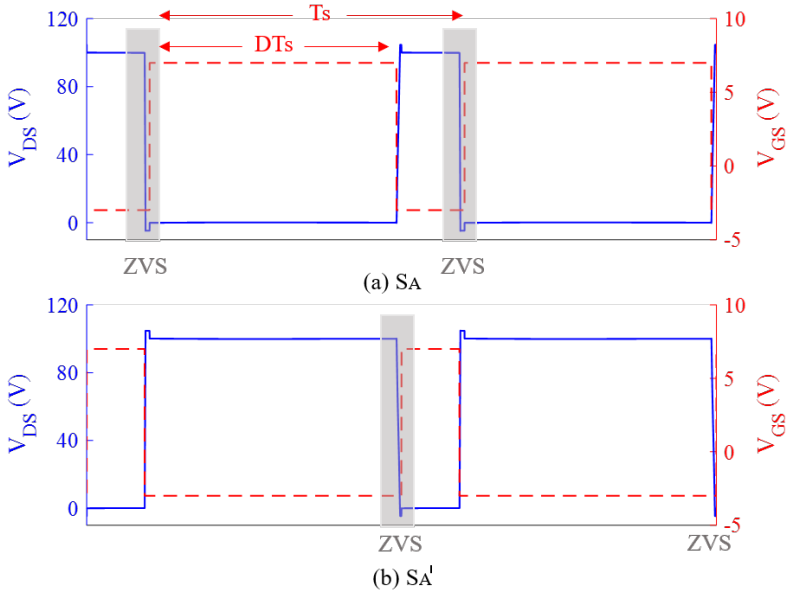

Figure 4.15: Drain-source and gate-source voltage waveforms at $D = 0.8$ and $f = 80kHz$ for dominant WPT-CSR current conditions. ZVS regions are colored in gray.

To conclude, when the I_M is dominant, the soft-switching conditions do not change due to the addition of I_{TX}. However, the system can sustain a ZVS on both legs when $\hat{I}_{TX}$ is greater than the I_M.

4.6 The Stress on the DC-link Capacitor

The DC-link capacitor of the motor drive meets the sudden current requirements at the switching transients. With the introduction of the WPT system, an additional high-frequency current exists, which will create stress on the DC-link capacitor. The increase in the DC-link current should be analyzed to show the feasibility of the proposed CSR's implementation into a conventional drive.

Firstly, the DC-link capacitor current, (I_{CAP}), is expressed as in (4.9) using switching functions (S_A and S_B), motor current, Tx coil current and input current.

$$I_{CAP} = S_A(I_M + I_{TX}) - S_B(I_M + I_{TX}) - I_{in} \tag{4.9}$$

Then, the switching harmonics of the motor current can be ignored (I_{Mdc}), and the first harmonic approximation (FHA) can be applied to the WPT current (I_{TXf}) as shown in (4.10).

$$\begin{aligned} I_M &= I_{Mdc} \\ I_{TX} &= I_{TXf} cos(2\pi f_s t - \Phi) \end{aligned} \tag{4.10}$$

Thus, the DC-link current harmonic distribution can be obtained as in (4.11) and (4.12).

$$I_{capM} = \sum_{k=1}^{\infty} \frac{4I_{Mdc}}{k\pi} sin(k\pi D) cos(2\pi k f_s t) \tag{4.11}$$

$$\begin{aligned} \mathrm{I_{capTX}} = &- I_{TX} cos(2\pi f_s t - \Phi) \\ &+ \sum_{k=1}^{\infty} \frac{2I_{TX}}{k\pi} sin(k\pi D) cos(2\pi (k+1) f_s t - \Phi) \\ &+ \sum_{k=2}^{\infty} \frac{2I_{TX}}{k\pi} sin(k\pi D) cos(2\pi (k-1) f_s t + \Phi) \end{aligned} \tag{4.12}$$

Since the capacitor current is affected by the I_M and D, a worst-case scenario is analyzed for simplicity. In this scenario, the motor power is initially zero at $D = 0.5$, and the motor power is linearly increased to achieve 500 W at $D = 0.85$.

For all these operations, I_M is at the rated value. When the motor is connected, the DC-link current can be calculated as in (4.11). Then, the WPT system is connected parallel to the motor. The WPT system supplies continuous 50W power while the D varies between 0.15 and 0.85. Therefore, the capacitor current, which stems from the WPT system, is calculated using (4.12). As a result, the capacitor currents for stand-alone and concurrent operation modes are shown in Fig. 4.16.

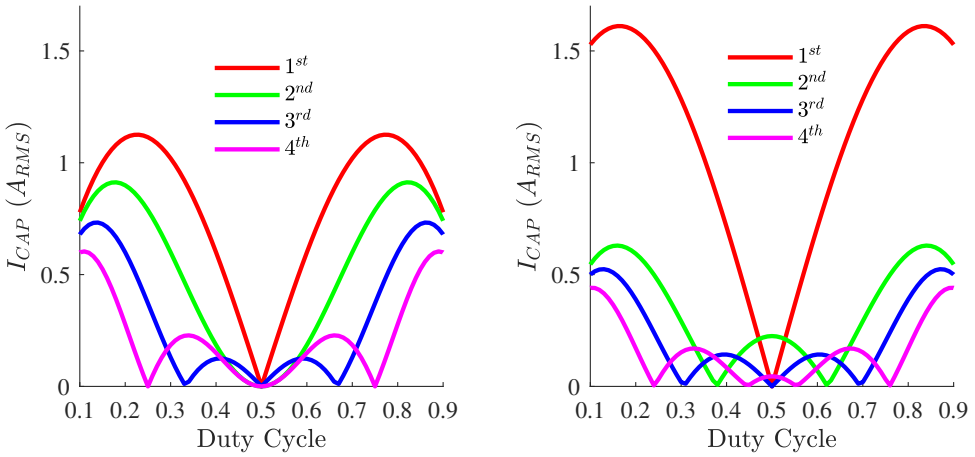

(a) DC-link current under single motor operation. (b) DC-link current under concurrent motor and WPT-CSR operation.

Figure 4.16: First, second, third and fourth harmonics of the DC link currents as a function of duty cycle.

It is observed that the capacitor current increases from 1.45 $\mathrm{A_{RMS}}$ to 1.8 $\mathrm{A_{RMS}}$, resulting in a 24% rise. A conventional motor drive can still overcome this rise with its slightly over-designed DC-link capacitance for safe operation. Even so, this may require minor capacitance modifications to avoid reducing the drive's lifetime. Moreover, the type of the capacitor may be required to change since high-frequency current ripples are increased. Film or ceramic capacitors have lower parasitics (ESR and ESL); therefore, their high-frequency ripple capability is better than the electrolytic capacitors. If the majority of capacitors in the motor drive are electrolytic, they may be altered to their film or ceramic counterparts.

4.7 Conclusion

In this chapter, the proposed CSR is implemented with a DC motor drive. Unlike conventional systems, the proposed method does not require an extra converter, and the existing motor driver is used to run the motor and transfer wireless power concurrently. Hence, the complexity and cost are decreased. However, implementing the system with a conventional drive is challenging due to choosing a proper switching frequency. Whereas a higher switching frequency increases the drive losses, a lower switching frequency increases the coil sizes and cost. Thanks to the development of wide band-gap devices such as GaN and SiC, a sweet spot in the switching frequency could be found, satisfying both requirements. Thus, the wide band-gap-based motor drives can be used as a single converter to drive the motor and transfer wireless power concurrently.

In order to validate the proposed system, an experimental setup was established with a GaN-based motor drive. A bipolar- PWM technique was employed, and the variable switching frequency was utilized in addition to the PWM technique. Firstly, the motor drive operated with and without the WPT system, and it was observed that it does not affect the motor operation. Then, in order to control the powers of the WPT system and the motor separately, variable duty cycle and switching frequency were engaged. Under any motor operation, the rated output power of the WPT system was achieved by adjusting the proper switching frequency. Besides, the transient variations of the motor or WPT system's load were performed, and it was acquired that the load variation does not affect steady-state operation. Furthermore, a calorimeter setup was established to examine the effect of the additional WPT system's current on the motor drive in a thermal manner. The loss increase of the motor drive was measured as a 10% increase of the loss of only motor at rated operation. Therefore, the increase is manageable since the system is already designed with a safety limit in such a range.

Furthermore, soft-switching conditions are analyzed. According to the loading conditions of the motor and the WPT system, it was concluded that the motor drive could make soft-switching at turn-on time. Then, the increase in the DC-link capacitor stress due to the additional WPT system's current was analyzed, and it was con-

cluded that the proposed CSR could be implemented with any wide band-gap-based conventional motor drive with maybe a slight modification of the DC-link capacitance. Although the proposed system was tested on a separately excited DC motor with bipolar- PWM technique, it can be expanded systematically to other DC motors and PWM techniques. Besides, the proposed CSR can be implemented with AC motor drives, which will be explained in detail in the following chapter as mentioned in this chapter.

CHAPTER 5

THE IMPLEMENTATION OF THE PROPOSED METHOD WITH AC MOTOR DRIVES

AC motors are more commonly used in the industry than DC motors; therefore, implementing the proposed CSR method with an AC motor drive creates a more impact. This chapter investigates implementing the proposed CSR method with a conventional AC motor drive, similar to the implementation with DC motor drives discussed in the previous chapter.

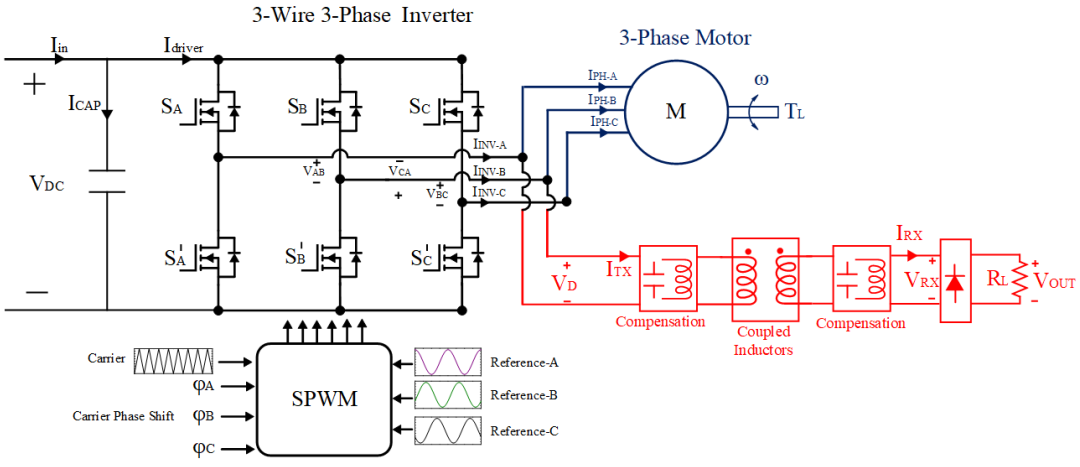

(a)

Figure 5.1: The circuit diagram of a single inverter system, which drives concurrently $3W$-3Φ motor and WPT system.

In this chapter, an experimental setup with a 3-wire 3-phase GaN-based inverter where sinusoidal-PWM (SPWM) is established. The electrical equivalent circuit diagram of the setup is given in Fig. 5.1. The proposed system is connected between any

two legs of the inverter, and its power is controlled by introducing the carrier phase shift (CPS) between them. In this setup, an induction machine (IM) and auxiliary rotating electric loads (placed over the shaft), such as sensors, and radars, are driven concurrently. In such systems, the loads usually require constant voltage, whereas their power demand changes in time. Therefore, the WPT system has variable output resistance. The design of the WPT system will be made to have a constant output voltage under variable output resistance. Since the WPT system is connected to any two legs of the motor drive, an unbalance of current distribution is revealed. However, the WPT system rated current is less than the motor rated current, and this unbalance can be disregarded.

5.1 The Motor Drive System and Experimental Validation of the SPWM with Carrier-Phase-Shift

The motor drive consists of a GaN-based 3-wire 3-phase converter, whose half-bridges are the same as in Chapter III. In AC motor drives, the frequency detuning control is not exploited to adjust WPT system power. Instead, a carrier-phase shift, previously explained in Chapter III, is introduced. For CPS method, the normalized magnitude ($\frac{\hat{V}_{ll}}{V_{dc}}$) of the fundamental frequency, switching frequency, and its sidebands is calculated as given in (5.1 to 5.4).

$$V_f(m_a) = \frac{\sqrt{3}}{2} m_a \tag{5.1}$$

$$V_{sl}(m_a) = \frac{2}{\pi} J_2\left(m_a \frac{\pi}{2}\right) \sqrt{1 - cos(\phi_{CPS} + 120^o)} \tag{5.2}$$

$$V_s(m_a) = \frac{2}{\pi} J_o\left(m_a \frac{\pi}{2}\right) \sqrt{1 - cos(\phi_{CPS})} \tag{5.3}$$

$$V_{sh}(m_a) = \frac{2}{\pi} J_2\left(m_a \frac{\pi}{2}\right) \sqrt{1 - cos(\phi_{CPS} - 120^o)} \tag{5.4}$$

Experimental measurements were taken to validate the CPS method with SPWM. The variation in the magnitudes of the fundamental frequency, switching frequency, and its sidebands are investigated. The inverter output voltages are shown in Fig. 5.2 for the phase shift of $\phi_B = 0^o$ and $\phi_B = 47.5^o$. The normalized inverter output voltages, achieved by theoretical and experimental results, are compared in Table 5.1. The experimental results agree well with the theoretical results with less than 10% error. It was verified that the CPS method controls the magnitude of the switching frequency component and its sidebands while the modulation index controls the magnitude of the fundamental component.

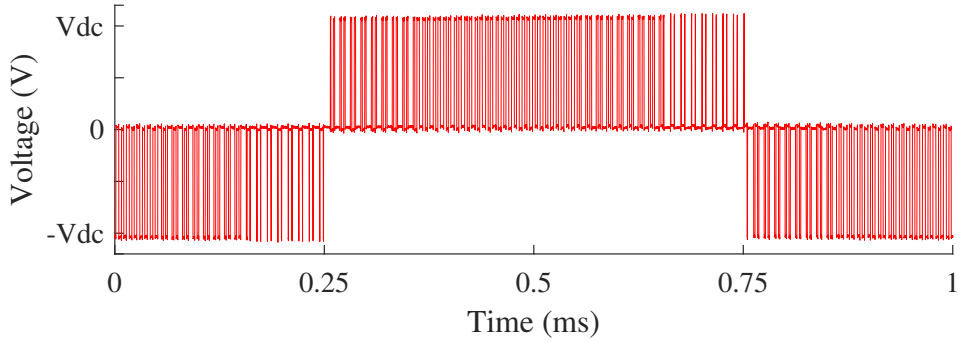

(a) $\phi_{CPS} = 0^o$

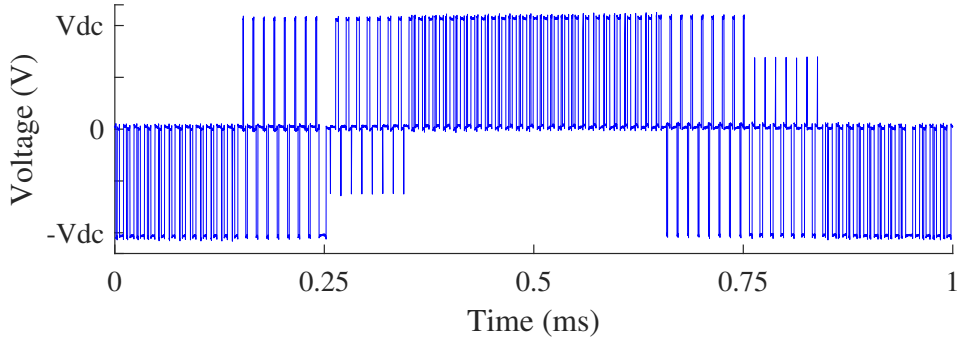

(b) $\phi_{CPS} = 47.5^o$

Figure 5.2: Inverter output voltage (V_{l-l}) (or called as drive voltage V_D) at $m_a = 0.6$ for $\phi_{CPS} = 0^o$ and $\phi_{CPS} = 47.5^o$.

Table 5.1: Theoretical and Experimental Results of Inverter Output Harmonic Distribution for $\phi_{CPS} = 0^o$ and $\phi_{CPS} = 47.5^o$

		A_{INV} ($\hat{V}_{ll}/V_{dc}$)			
		at $\mathbf{f_o}$	at $\mathbf{f_l}$	at $\mathbf{f_s}$	at $\mathbf{f_h}$
$\mathbf{m_a = 0.6}$ $\phi_{\mathbf{CPS}} = \mathbf{0}$	**Theoretical**	0.519	0.113	0	0.113
	Experimental	0.532	0.110	0.011	0.115
	Error	2.5%	2.6%	-	1.7%
$\mathbf{m_a = 0.6}$ $\phi_{\mathbf{CPS}} = \mathbf{47.5^o}$	**Theoretical**	0.519	0.130	0.405	0.077
	Experimental	0.537	0.127	0.414	0.084
	Error	3.4%	2.3%	2.2%	9.1%

5.2 Induction Motor with Auxiliary Rotating Electric Loads

In industrial applications, induction motors are used thanks to their robust and simple structures. The auxiliary rotating loads (such as IoT devices, surveillance cameras, robotic actuators, radars, and sensors) are frequently delivered by a contactless slip ring over the shaft of this motor. In this section, an setup is established with a 3-wire 3-phase IM and a WPT system for an auxiliary rotating load. The circuit diagram of the system and the expected voltage and current waveforms are shown in Fig. 5.3 where the SPWM with CPS is utilized. The input-output specifications of this system are given in Table 5.2.

Table 5.2: The Input-Output Specifications of the WPT System

Ratings	
DC-link voltage (V_{DC})	100 V
Modulation index (m_a)	$0 - 1$
Motor rated power (P_{motor})	500 W
Carrier-phase-shift range (Φ_{CPS})	$30^{\text{o}} - 60^{\text{o}}$
WPT-CSR output voltage (V_{OUT})	15 V_{RMS}
WPT-CSR input voltage (V_D)	30 V_{RMS}
WPT-CSR rated power ($P_{WPT-CSR}$)	24 W

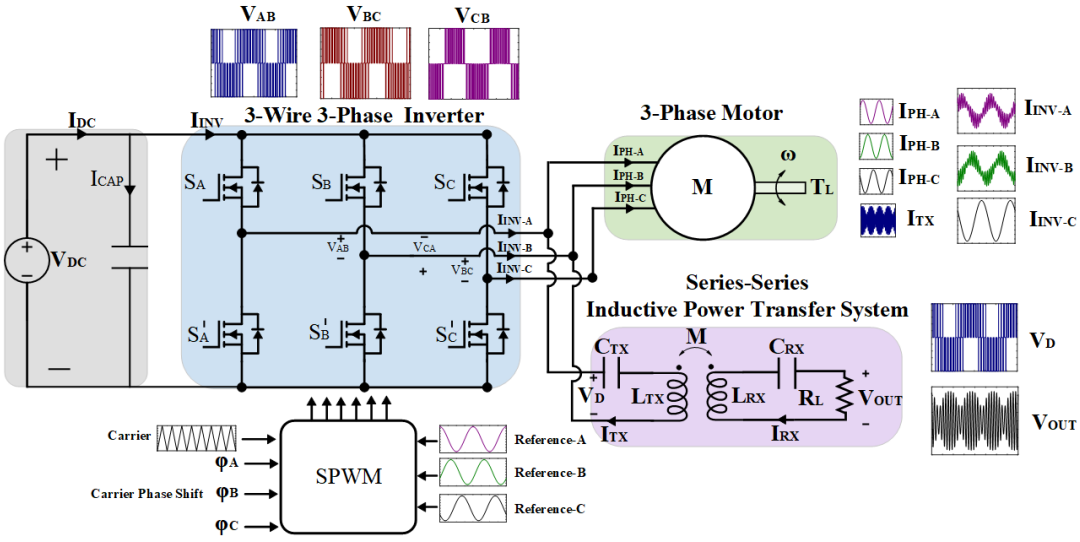

(a)

Figure 5.3: The circuit diagram of a single inverter system, which drives concurrently $3W$-3Φ motor and WPT system.

The control range of the CPS is selected between 30^o and 60^o since this range provides constant/continuous excitation voltage at the switching frequency under any modulation index, as can be presented in Fig. 5.4. In this range of CPS, the normalized input voltage of the WPT system varies between 0.25 and 0.45. In this setup, the normalized excitation voltage is selected as 0.3, which gives 30 V_{RMS} for a 100 V DC-link.

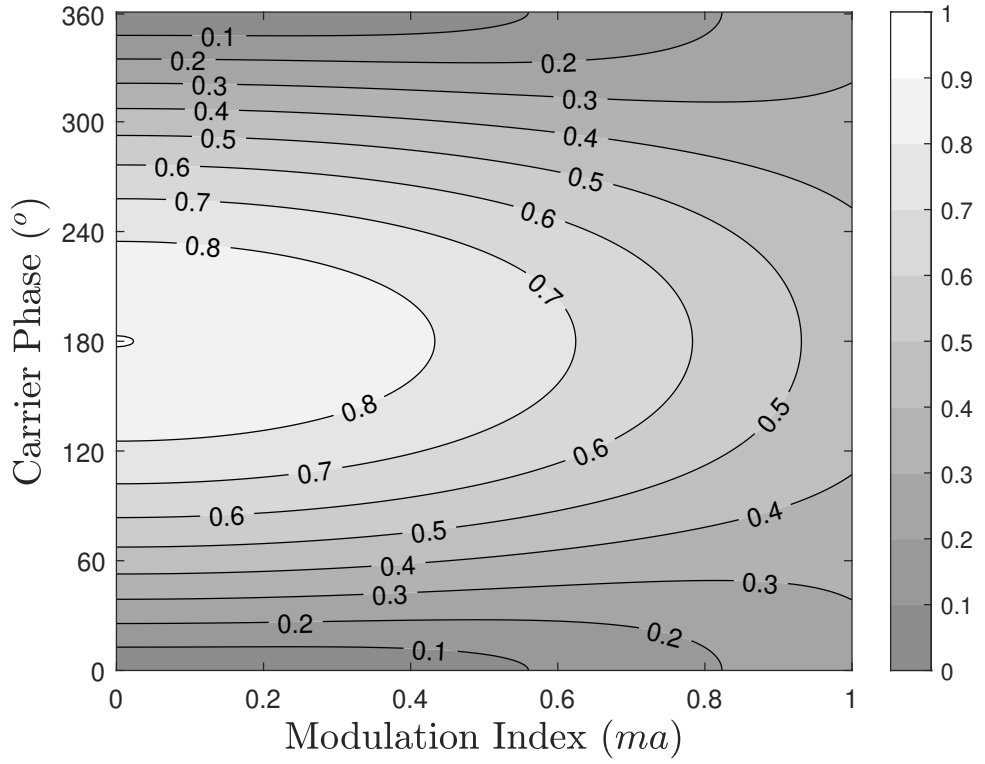

Figure 5.4: Normalized inverter output voltages $|\frac{V_{l-l}}{V_{DC}}|$ using the center harmonic approach.

5.2.1 WPT System Parameters Specification

The WPT system is series-series (SS) compensated, the circuit diagram of which is shown in Fig. 5.5, and the operating frequency is selected between 85 kHz.

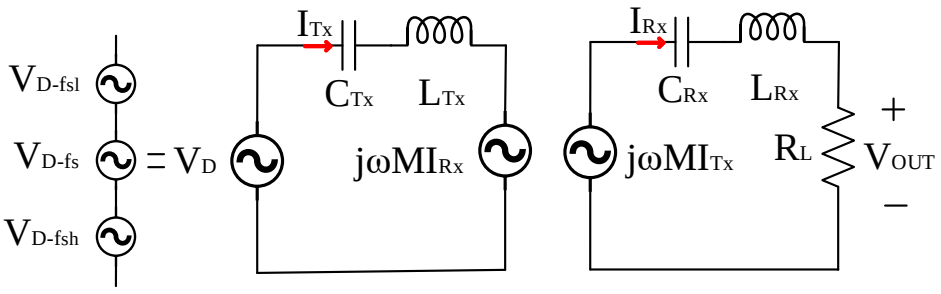

Figure 5.5: The first harmonic approach circuit diagram of the WPT system.

In general, auxiliary systems such as sensors and IoT devices have varying loads with a constant voltage (CV). Thus, the WPT system is designed to supply CV output with variable resistive loads. In SS compensation, CV operation can be achieved at two frequencies, which are called lower and higher resonant frequencies (ω_{rl}, ω_{rh}).

Firstly, the output voltage (V_{OUT}) and voltage gain (A_{WPT}) system are calculated as in (5.5) and (5.6).

$$\begin{aligned} V_{OUT} =& \frac{j\omega M I_{Tx}}{Z_{Rx}} R_L \\ =& \frac{j\omega M}{Z_{Rx}} \left(\frac{V_{IN}}{\frac{\omega^2 M^2}{Z_{Rx}} + Z_{Tx}} \right) R_L \\ =& \frac{j\omega M V_{IN}}{\omega^2 M^2 + Z_{Tx} Z_{Rx}} R_L \end{aligned} \tag{5.5}$$

$$\begin{aligned} A_{WPT} =& \left| \frac{V_{OUT}}{V_{IN}} \right| \\ =& \frac{\omega M}{\omega^2 M^2 + Z_{TX} Z_{RX}} R_L \end{aligned} \tag{5.6}$$

The frequencies providing a load-independent voltage gain can be found by equating the load resistance derivative of the voltage gain, which is presented in (5.7), to zero.

$$\frac{dA_{WPT}}{dR_L} = 0 \tag{5.7}$$

Then, the frequencies (in radian/sec) are calculated in (5.8) as a function of the coupling factor (k) and angular resonant frequency w_r.

$$\begin{aligned} \omega_{rl} =& \omega_r \sqrt{\frac{1}{1+k}} \\ \omega_{rh} =& \omega_r \sqrt{\frac{1}{1-k}} \end{aligned} \tag{5.8}$$

The minimum load resistance that delivers the rated power can be calculated as in (5.9).

$$R_L = \frac{V_{OUT}^2}{P_{rated}} \tag{5.9}$$

The operating frequency is selected as w_{rh}. Receiver inductance is calculated using the load resistance and the chosen quality factor of Rx (Q_{Rx}) (at this operating frequency) as provided in (5.10).

$$\begin{aligned} Q_{Rx} &= \frac{\omega_{rh} L_{Rx}}{R_L} \\ L_{Rx} &= \frac{Q_{Rx} R_L}{\omega_{rh}} \end{aligned} \tag{5.10}$$

The voltage gain of the WPT system is given in (5.11), and adjusted by Tx inductance. Thus, Tx inductance is selected using (5.12).

$$A_{WPT(\omega_{rh})} = \left| \sqrt{\frac{L_{Rx}}{L_{Tx}}} \right| \tag{5.11}$$

$$L_{Tx} = \frac{L_{Rx}}{A^2_{WPT(\omega_{rh})}} \tag{5.12}$$

Then, the mutual inductance is calculated as given in (5.13).

$$M = k\sqrt{L_{Tx} L_{Rx}} \tag{5.13}$$

Finally, the compensation capacitances are adjusted as given in (5.14).

$$\begin{aligned} C_{Tx} &= \frac{1}{\omega_r^2 L_{Tx}} \\ C_{Rx} &= \frac{1}{\omega_r^2 L_{Rx}} \end{aligned} \tag{5.14}$$

The initial/chosen and derived parameters are presented in Table 5.3. The voltage gain-frequency graphs of the designed WPT system for different load resistances are shown in Fig. 5.6.

Table 5.3: WPT System Parameters

Initial/Choosen Parameters	Values	Derived Parameters	Values
P_{rated}	24 W	A_{WPT}	0.5
V_D	30 V_{RMS}	R_L	9.3 Ω
V_{out}	15 V_{RMS}	L_{Rx}	50 μH
f_{rh}	85 kHz	L_{Tx}	200 μH
Q_{Rx}	2.9	M	40 μH
k	0.4	f_r	65.85 kHz
		C_{Tx}	29.2 nF
		C_{Rx}	117 nF

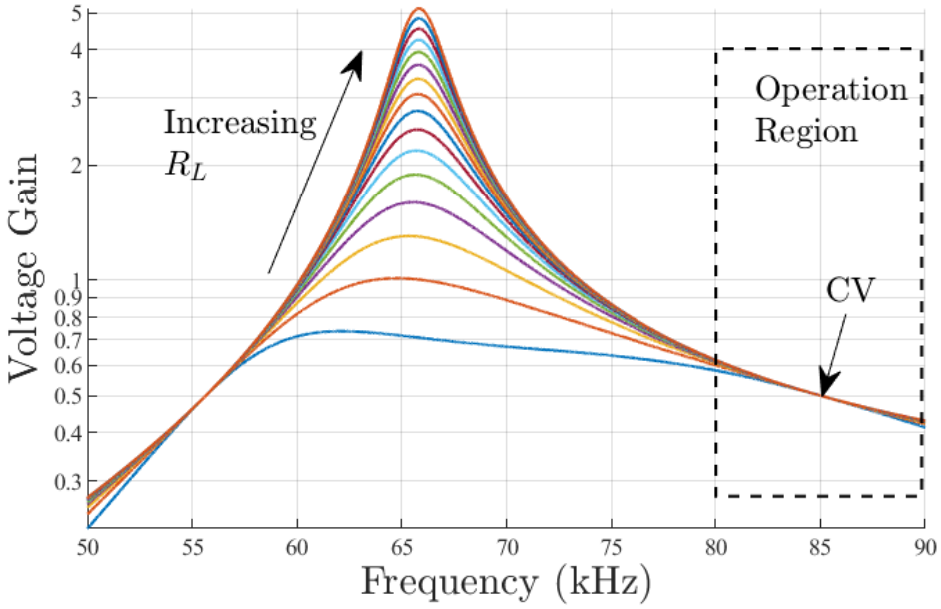

Figure 5.6: The voltage gain of the WPT system for different load resistances.

5.2.2 Experimental Validation

The experimental setup is shown in Fig. 5.7. The AC motor is loaded using a DC generator. The WPT system is connected to the motor's shaft, and load resistances are placed on the rotating Rx side.

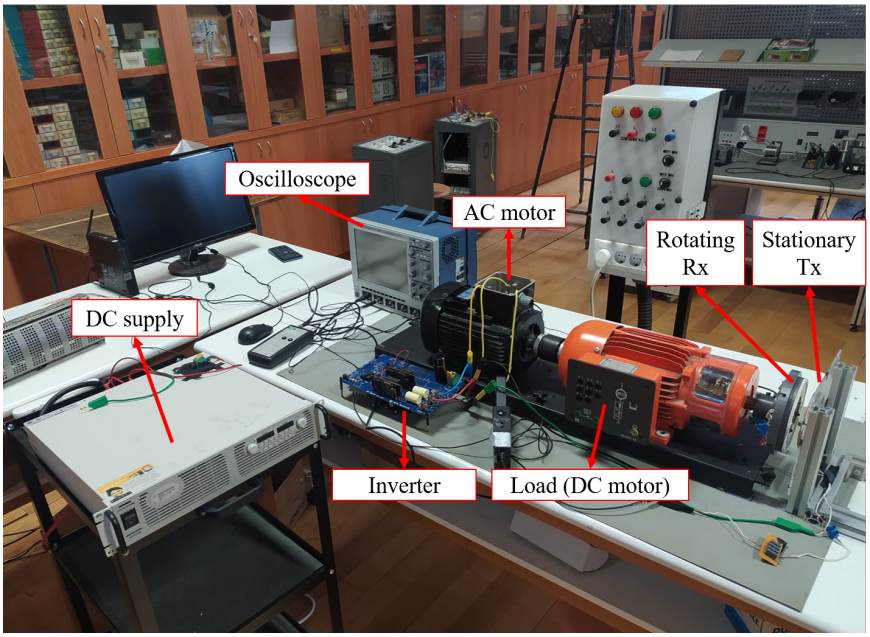

Figure 5.7: Experimental Setup.

5.2.2.1 Stand-alone and Concurrent Operations of the Motor and the WPT System

In order to confirm the concurrent operation, the WPT system and the motor operated respectively stand-alone and simultaneously. Carrier phase shift was adjusted to 40^o with $m_a = 0.8$, and they were kept the same for three operations. The I_M and I_{Tx} are plotted in Fig. 5.8 for these operations. Firstly, for stand-alone motor operation, the motor current was measured as ~ 1.75 A. Then, the WPT system is connected to the motor drive and draws ~ 0.35 A. Finally, the inverter runs the motor and WPT system concurrently. It was observed that the systems draw almost the same current for the identical m_a and ϕ_{CPS}.

5.2.2.2 Control Method Validation

The motor's speed and torque are controlled by SPWM that adjusts fundamental frequency via m_a. However, changing m_a varies the WPT system's output voltage under a constant ϕ_{CPS}. Therefore, in order to keep output voltage constant, variable ϕ_{CPS} should be applied.

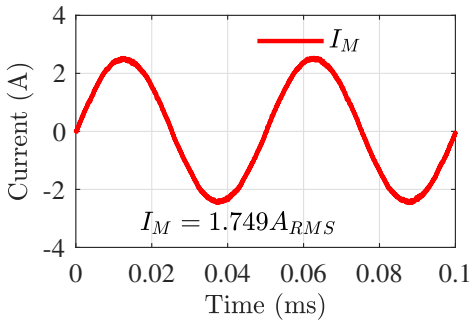

(a) Only motor operation.

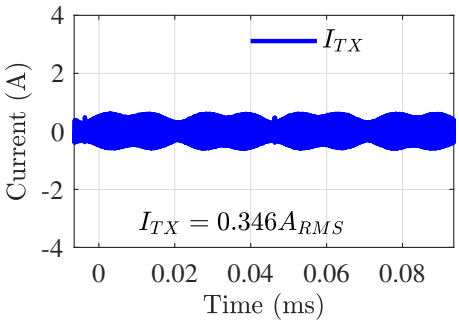

(b) Only WPT operation.

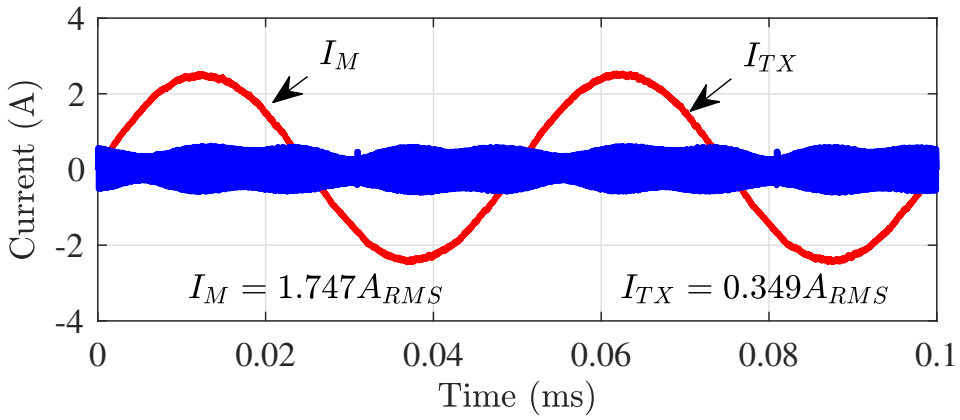

(c) Concurrent operation of motor and WPT.

Figure 5.8: The motor phase and the WPT system's Tx currents.

The normalized power was experimentally acquired for constant and variable ϕ_{CPS}, which are shown in Fig. 5.9. If the normalized power reduces due to the change in m_a, ϕ_{CPS} should be increased to reach the desired power. Likewise, if the normalized power rises due to the change in m_a, ϕ_{CPS} should be reduced to reach the desired power. Further, ϕ_{CPS} used in the experimental setup to keep constant power are compared with theoretical calculations in Table 5.4, and the error stays below 4%.

Table 5.4: Carrier Phase Shift Requirements for Different Modulation Indexes.

Modulation index (m_a)	**0**	**0.1**	**0.2**	**0.3**	**0.4**	**0.5**	**0.6**	**0.7**	**0.8**	**0.9**	**1**
Phase shift ($\theta_{\mathbf{an}}$) (Theoretical)	41	41	41.2	42.4	44.1	46.0	48.2	50.3	51.9	52.0	46
Phase shift ($\theta_{\mathbf{exp}}$) (Experimental)	41	41.2	41.8	42.7	44	45.7	47.5	49	50	51	46
Error	0%	-0.5%	-1.4%	-0.7%	0.2%	0.6%	1.4%	2.5%	3.6%	1.92%	0%

Error = $|\frac{\theta_{\mathbf{an}} - \theta_{\mathbf{exp}}}{\theta_{\mathbf{an}}} 100|$

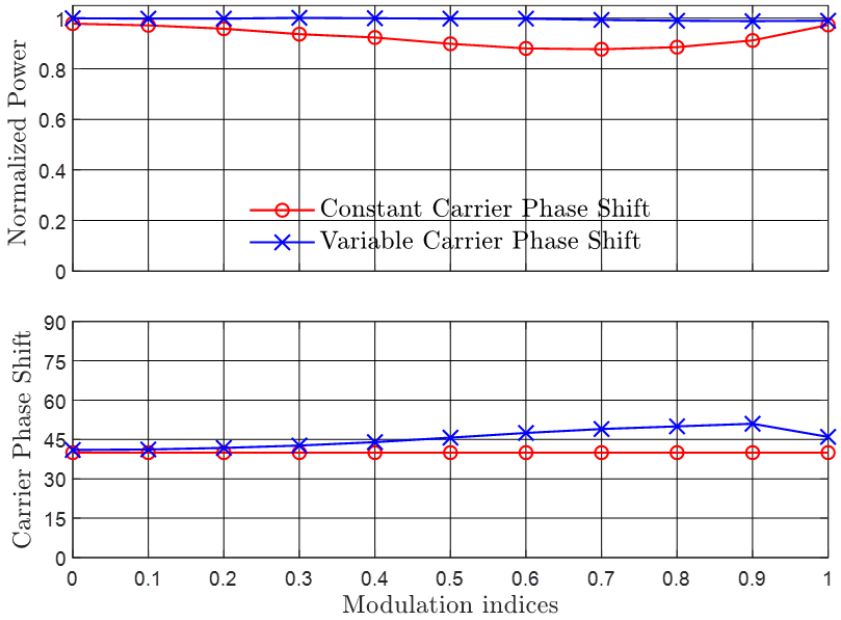

Figure 5.9: Powers of the WPT system for constant and variable carrier phase shift.

5.2.2.3 Transient Load Changes of Motor and the WPT System

The effect of transient load changes is analyzed under the constant control parameters such as m_a and ϕ_{CPS}. The I_M and I_{Tx} are shown in Fig 5.10. Firstly, the motor load torque is changed while control parameters are kept constant. It was observed that the WPT system is not disturbed by the transient load changes of the motor, as shown in Fig 5.10.a. Then, the WPT load resistance is altered using the same procedure. As expected, the motor phase currents do not change, as shown in Fig. 5.10.b.

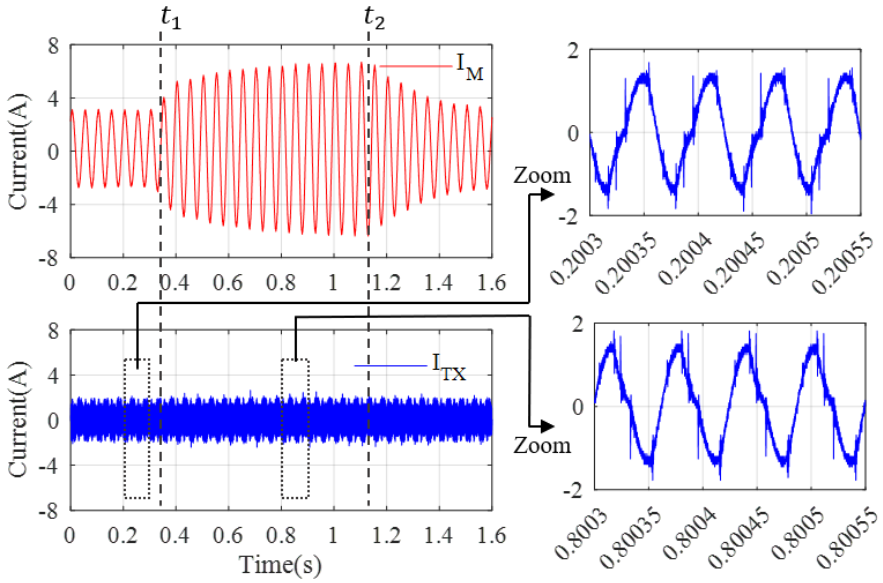

(a) At t_1, the motor load torque is increased, and at t_2, the motor load torque returns to the former value.

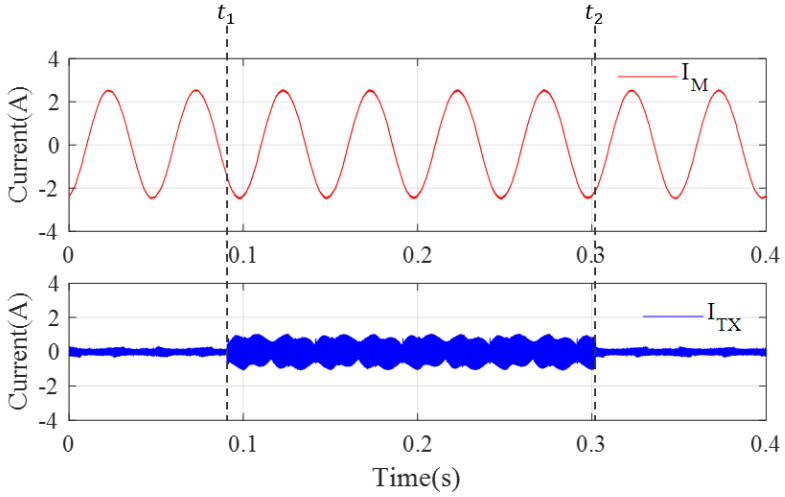

(b) At t_1, The WPT load resistance is decreased, and at t_2, WPT load resistance returns to the former value.

Figure 5.10: Transient load changes. a) Motor load changes. b) WPT system's load changes.

5.3 Conclusion

In this chapter, the proposed CSR was implemented with an AC motor drive. As similar to DC motor drives, a wide band-gap-based motor drive should be used to

reduce coil size with lower switching losses; therefore, a 3-wire 3-phase GaN-based inverter was used. An experimental setup was established where the motor drive is governed by SPWM with a carrier phase shift. Firstly, the harmonic distribution of SPWM is experimentally acquired and compared with theoretical calculations. It was observed that introducing a CPS controls the switching components while the modulation index adjusts the fundamental frequency. Secondly, an setup is established for induction machines with auxiliary rotating electric loads. A WPT system with constant output voltage was designed, and concurrent operation of the proposed CSR was procured. Then, the system was tested under various modulation indices, and the power of the proposed CSR was kept constant using the proposed CPS method. After that, the transient variations of the motor or WPT system's load were performed, and it was acquired that the load variation does not affect steady-state operation. Consequently, with the CPS method, the proposed CSR has been verified for induction machines driven by SPWM. It can be expanded systematically to other AC motors and PWM techniques by applying similar design steps as mentioned in this chapter. In the following chapter, the proposed CSR will be implemented in a synchronous motor to excite its field winding.

CHAPTER 6

IMPLEMENTATION OF THE PROPOSED METHOD FOR THE FIELD EXCITATION OF SYNCHRONOUS MOTORS

In recent years, electric vehicle (EV) applications have become widespread since they give more efficient and clean energy. The main part of EVs is the traction system, which is based on electric machines (EMs); therefore, an efficient, reliable, sustainable, and cost-effective system design of EMs is significant. Permanent magnet synchronous machines (PMS) have been frequently preferred in traction systems since they provide high torque density and high efficiency compared to their contenders, such as induction motors (IMs), switched reluctance motors (SRMs), and wound-field synchronous motors (WFSMs)[72]. However, rare-earth magnet materials such as neodymium (Nd) and samarium (Sm) used in PM motors have high prices and an unstable supply chain due to the monopoly of China. Therefore, literature and industry have addressed less-PM or no-PM motors, so they turned back to mature technologies, especially WFSMs [73, 74, 75]. Although WFSMs have lower-torque density and lower efficiency than PM machines, they decrease the total cost and increase control schemes such as loss minimization by externally exciting fields [76]. Moreover, demagnetization due to thermal issues is out of the question in WFSMs, increasing reliability. However, the power transfer to WFSMs' field winding is challenging, and contactless slip rings should be used. In this study, the proposed CSR is implemented to excite the field winding of WFSMs. Thus, a cost-efficient and simple solution is proposed as an alternative to PM traction motors.

6.1 Small-Scale Prototyping

A small-scale experimental prototype is established to validate the field excitation by the proposed CSR. The block diagram of the proposed system is presented in Fig. 6.1.

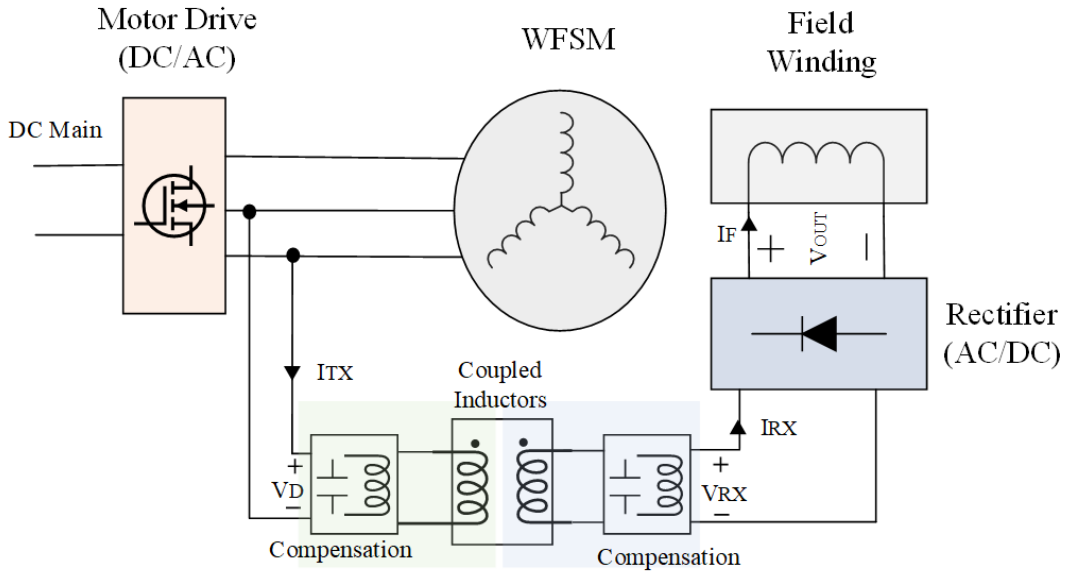

Figure 6.1: Block diagram of the proposed CSR based on WPT system for field excitation of WFSMs.

The same inverter described before is used, and SPWM with carrier phase shift is employed. In this setup, the normalized input voltage is selected as 0.40, which gives 40 V_{RMS} for a 100 V DC-link. The synchronous motor specifications are presented in Table 6.1.

Table 6.1: The Input-Output Specifications of the SM

Ratings	
DC-link voltage (V_{DC})	100 V
Modulation index (m_a)	$0-1$
Field current (I_f)	5 A
Field resistance (R_L)	1.2Ω
The WPT system's rated output voltage (V_{OUT})	6 V
The WPT system's input voltage (V_D)	40 V_{RMS}
The WPT system's rated power ($P_{WPT-CSR}$)	30 W
Switching frequency (f_s)	60 kHz

6.2 The Design of the Wireless Power Transfer System

The WPT system is series-none (SN) compensated to reduce the weight of the rotating side. The transformer modeling of the SN-WPT is shown in Fig. 6.2.

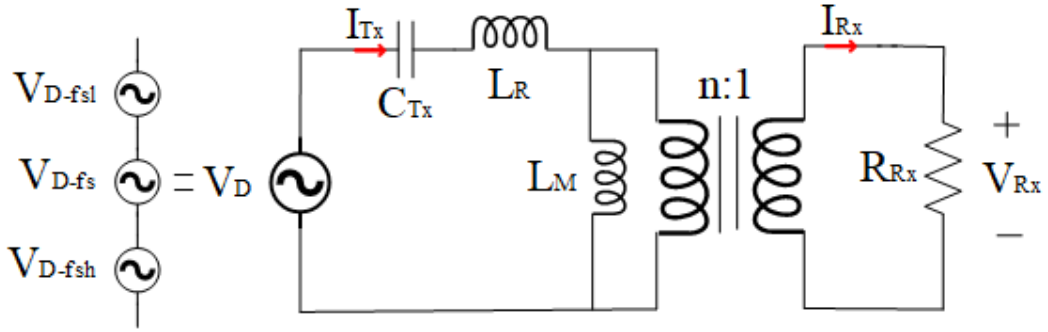

Figure 6.2: The first harmonic approach circuit diagram of the WPT system.

The field resistance is reflected from the diode rectifier, and receiver side resistance (R_{Rx}) and voltage (V_{Rx}) can be calculated as given in (6.1,6.2).

$$V_{Rx} = \frac{2\sqrt{2}}{\pi} V_{OUT} \tag{6.1}$$

$$R_{Rx} = \frac{8}{\pi^2} R_L \tag{6.2}$$

Then, the transformer turns ratio can be calculated using the voltage gain as given in (6.3).

$$n = \frac{V_D}{V_{Rx}} \tag{6.3}$$

The turns ratio depends on the Tx/Rx inductances, and coupling factor (k) between them, presented in (6.4) where $L_{Tx} = \frac{L_R}{1-k^2}$.

$$n = k\sqrt{\frac{L_{Tx}}{L_{Rx}}} \tag{6.4}$$

The Rx inductance is selected using the quality factor (Q), R_{Rx} and resonant angular frequency (ω_r), as given in (6.5).

$$L_{Rx} = Q\frac{R_{Rx}}{\omega_r} \tag{6.5}$$

Then, the Tx inductance is calculated using the required n, selected k, and L_{Rx}, as presented in (6.6).

$$L_{Tx} = \frac{n^2}{k^2}L_{Rx} \tag{6.6}$$

After that, the Tx compensation capacitance (C_{Tx}) is tuned as given in (6.7).

$$C_{Tx} = \frac{1}{\sqrt{\omega_r^2 L_R}} \tag{6.7}$$

The initial/chosen and derived parameters are shown in Table 6.2.

Table 6.2: WPT System Parameters

Initial/Choosen Parameters	**Values**	**Derived Parameters**	**Values**	**Experimental Measurements**
P_{rated}	30 W	V_{Rx}	5.4	-
V_D	40 V_{RMS}	R_{Rx}	0.97 Ω	-
V_{OUT}	6 V_{DC}	n	7.4	-
f_{rh}	65 kHz	L_{Tx}	1500 μH	1510 μH
Q_{Rx}	2.75	L_{Rx}	6.5 μH	6.5 μH
k	0.485	M	47.8 μH	48 μH
R_L	1.2 Ω	C_{Tx}	6.11 nF	5.9 nF

6.3 Experimental Validation

The experimental setup is shown in Fig. 6.3.

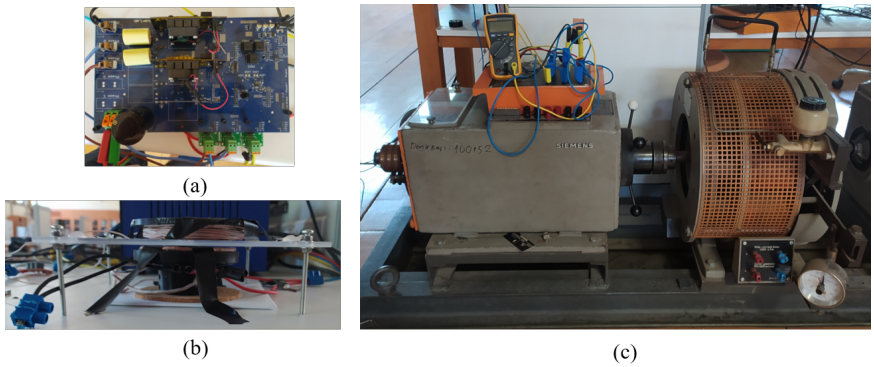

Figure 6.3: Experimental Setup. a) Motor drive. b) WPT coils. c) Synchronous machine.

In order to confirm concurrent operations, the WPT system is connected in parallel to the synchronous motor to excite the field winding. Firstly, ϕ_{CPS} was adjusted to 55^o with $m_a = 0$. The motor phase and field currents are shown in Fig. 6.4.a for this operating point. Then, m_a and ϕ_{CPS} were brought to 0.3 and 58^o. It was observed in Fig. 6.4.b that while the motor phase current increases, the field current stays the same. After that, m_a and ϕ_{CPS} were brought to 0.5 and 64^o.

It was observed in Fig. 6.4.c that while the motor phase current increases, the field current stays the same. Since no speed and the current controller are applied, increasing the modulation index also speeds up the motor. Thus, the fundamental frequencies at $m_a = 0.3$ and $m_a = 0.5$ are different, but it does not affect the carrier-phase-shift algorithm and the mean value of the field current. Moreover, it was observed that the field current has a low-frequency ripple, and the magnitude of the ripple becomes more dominant while increasing the modulation index. Thus, ripple at rectified sideband harmonics has twice the frequency of the fundamental frequency. The low-frequency ripples (with the subtracted mean value) are plotted in Fig. 6.5.

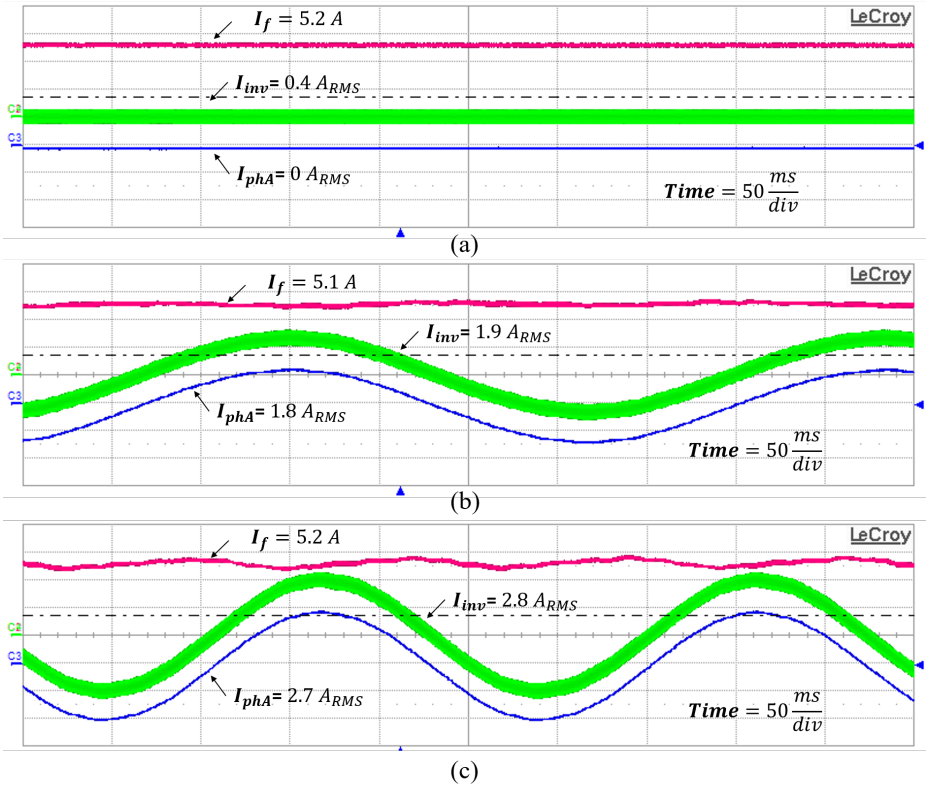

Figure 6.4: Concurrent operation of the synchronous motor's phases and field winding for different modulation index. a) $m_a = 0$ b) $m_a = 0.3$ at 185 RPM. c) $m_a = 0.5$ at 246 RPM.

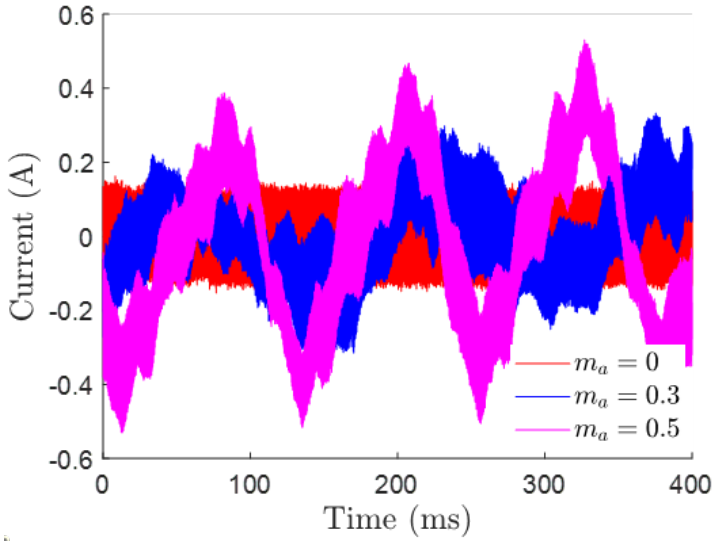

Figure 6.5: Low frequency field current fluctuations. a) $m_a = 0$ b) $m_a = 0.3$ at 185 RPM. c) $m_a = 0.5$ at 246 RPM.

6.4 A New Algorithm to Minimize the Current Fluctuation

The low-frequency ripple at the field current should be mitigated since it may cause torque ripples and speed oscillation, which can be critical in some applications. The low-frequency current fluctuation stems from the rectified sideband harmonics, and for a larger modulation index, the sideband harmonics become considerable, and the fluctuation increases. The fluctuation can be reduced by increasing the output capacitance. However, increasing capacitance causes a rise in weight and creates an extra point of failure. It also can be reduced by active control methods, which take the field current and update the carrier phase shift values. However, the field current lags due to field inductance, so a phase compensation is required. Besides, the control bandwidth hits a boundary of the wireless data transfer systems because the field is on the rotating side. Thus, controlling the carrier phase shift via current feedback is challenging. This section proposes a new algorithm that controls the switching harmonics and side bands in the modulation step. Therefore, the sideband harmonics can be eliminated even before they are created. Accordingly, additional circuits or passive filters on the rotating side or digital filters are not required, reducing the system's weight and cost.

6.4.1 Harmonic Investigation for a Switching Interval

For each switching interval, the duty cycle of the motor phases varies, and their average values equal the corresponding reference voltages at each time interval. An example of SPWM with reference, carrier, and PWM signals is shown in Fig. 6.6.

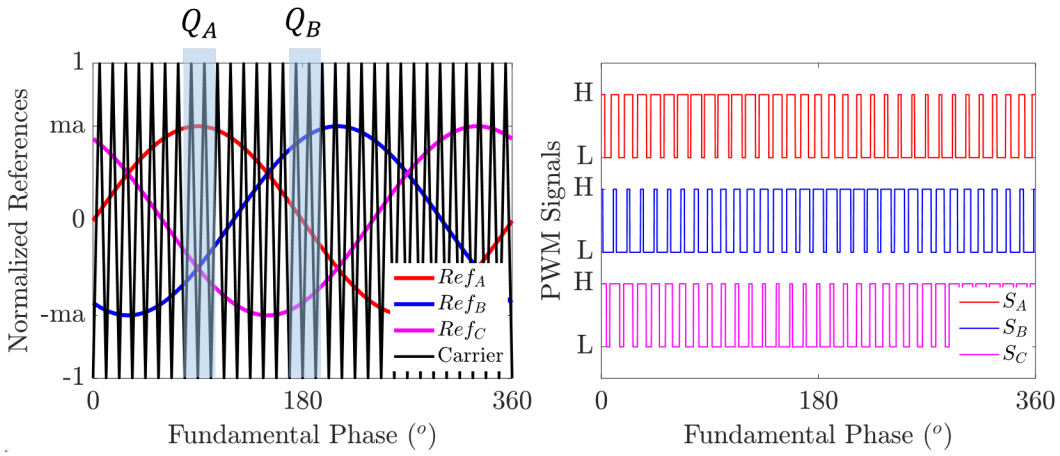

Figure 6.6: Sinusoidal-PWM along with a fundamental frequency. For visual clarity, the switching frequency is decreased.

Thus, varying duty cycles follow a reference signal. However, the change causes a fluctuation in the magnitude of the switching component. Therefore, due to this fluctuation, the input voltage of the WPT system changes over the fundamental period. PWM signals for a switching interval are given for two operation points (Q_A and Q_B), as given in Fig. 6.7. Using the Fourier series at the switching interval, the harmonic distribution is calculated as given in (6.8) where k is the harmonic order, D is the duty cycle, f_s is the switching frequency, ϕ_C is the phase angle of the carrier signal.

$$S(t) = \mathrm{D} + \sum_{\mathrm{k}=1}^{\infty} \frac{2}{\mathrm{k}\pi} \sin(\mathrm{k}\pi\mathrm{D})\cos(2\pi\mathrm{k}\mathrm{f_s}\mathrm{t} + \mathrm{k}\phi_\mathrm{C}) \tag{6.8}$$

The duty cycle follows the reference signals and can be calculated as given in (6.9).

$$\begin{aligned} D_A &= \frac{1 + m_a sin(\theta_f)}{2} \\ D_B &= \frac{1 + m_a sin(\theta_f - 120)}{2} \\ D_C &= \frac{1 + m_a sin(\theta_f + 120)}{2} \end{aligned} \tag{6.9}$$

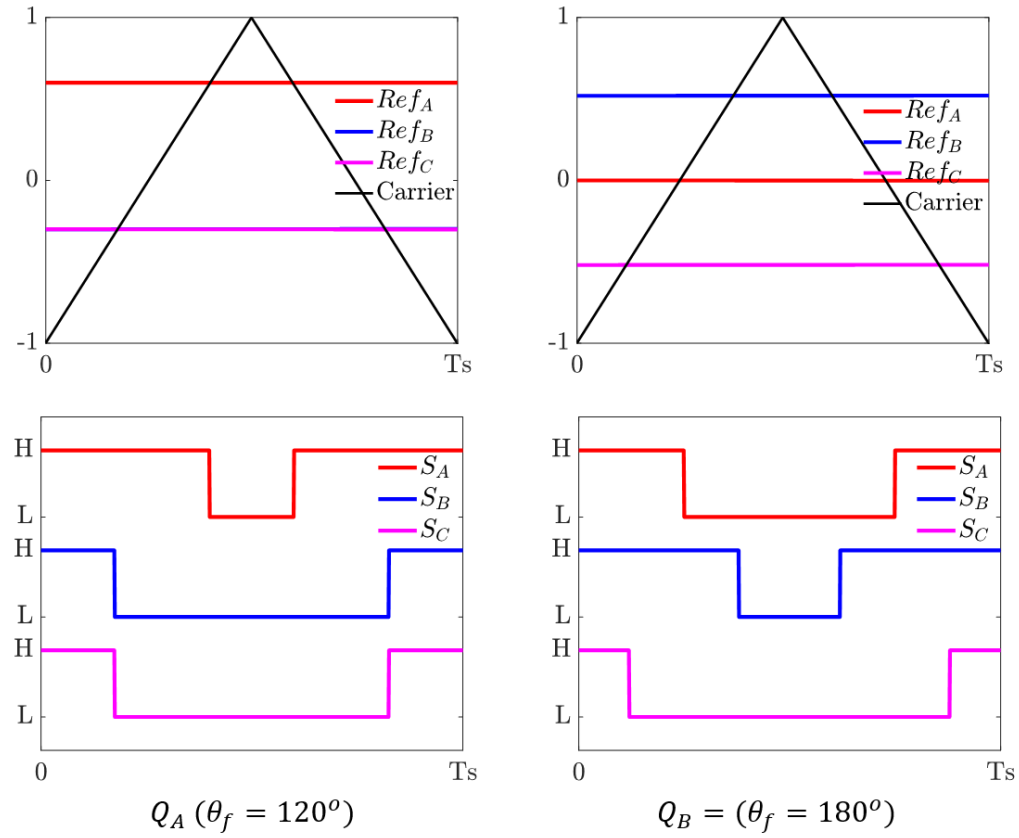

Figure 6.7: Reference and PWM signals for Q_A and Q_B.

Then, the switching harmonic can be calculated as presented in (6.10) where ϕ_{C-A}, ϕ_{C-B} and ϕ_{C-C} are the carrier phase angles of each reference signal.

$$\begin{aligned} S_A(t)^{f_s} &= \frac{2}{\pi} sin(\pi D_A) cos(2\pi f_s t + \phi_{C-A}) \\ S_B(t)^{f_s} &= \frac{2}{\pi} sin(\pi D_B) cos(2\pi f_s t + \phi_{C-B}) \\ S_C(t)^{f_s} &= \frac{2}{\pi} sin(\pi D_C) cos(2\pi f_s t + \phi_{C-C}) \end{aligned} \tag{6.10}$$

Conventionally, only one carrier signal is used to compare the reference signals, except in phase-split machines and modular motor drives, the carrier signals are given as a phase-shifted (or named interleaved) to reduce the input/output current ripples and capacitor stress. Using one carrier signal in the system causes voltage fluctuations at the switching harmonics, as shown in Fig. 6.8.

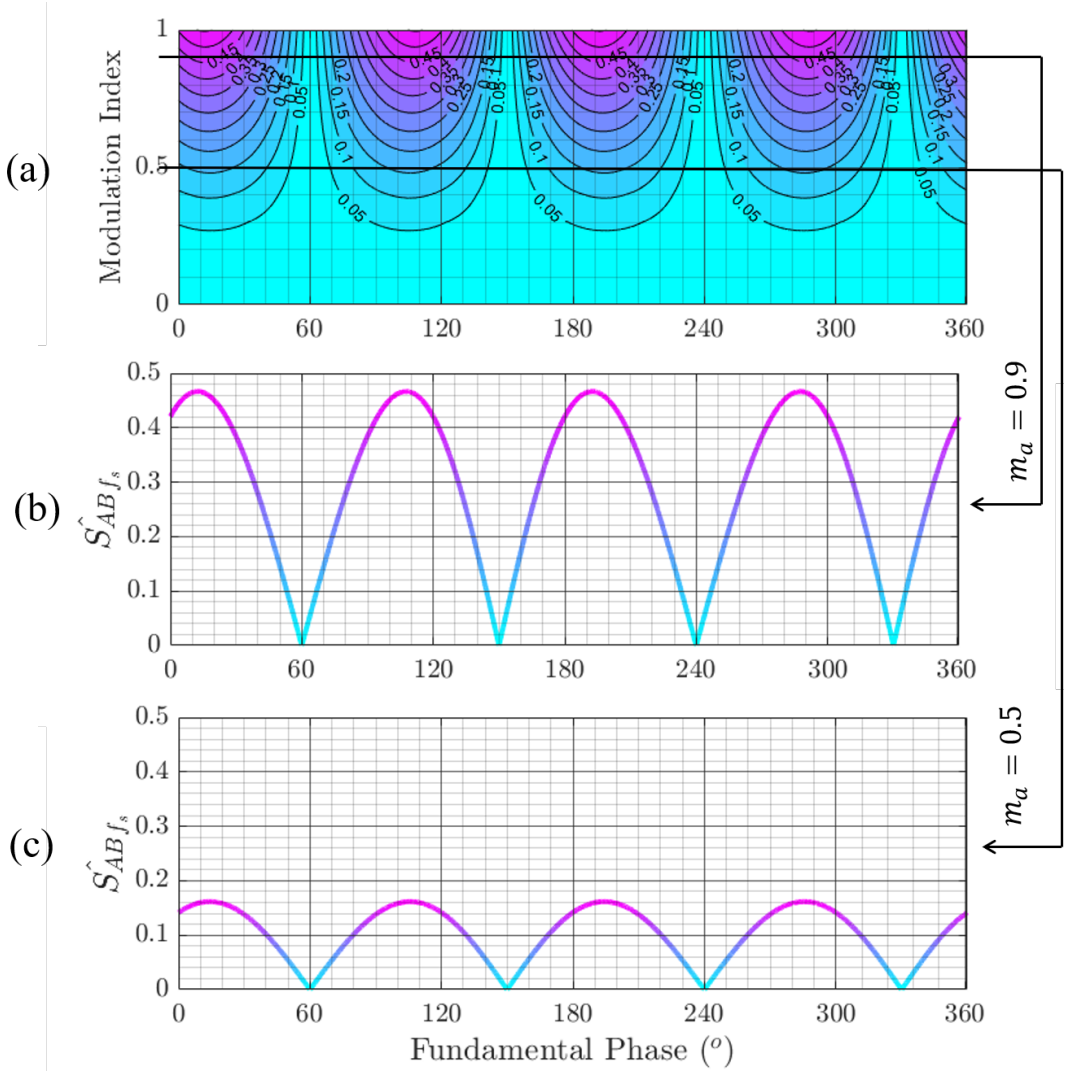

Figure 6.8: The magnitude of the switching components (between phase-A and phase-B) for different modulation indexes and fundamental phase angles. a) Contour of the magnitude of the switching component for a fundamental period and modulation index. b) The magnitude of the switching component over a fundamental period at that the modulation index is 0.9. c) The magnitude of the switching component over a fundamental period at that the modulation index is 0.5.

The magnitude of the switching component is calculated as given in (6.11).

$$\begin{aligned} S_{AB}(t)^{f_s} =& S_A(t)^{f_s} - S_B(t)^{f_s} \\ =& \frac{2}{\pi} sin(\pi D_A) cos(2\pi f_s t + \phi_{C-A}) \\ & - \frac{2}{\pi} sin(\pi D_B) cos(2\pi f_s t + \phi_{C-B}) \end{aligned} \tag{6.11}$$

Since the carriers are the same, a scalar subtraction can be applied, and the peak value of the switching harmonic is calculated as presented in (6.12).

$$\hat{S}_{AB_{f_s}} = \frac{2}{\pi}\Big(sin(\pi D_A) - sin(\pi D_B)\Big) \tag{6.12}$$

On the one hand, as discussed before, for all modulation indexes and all phase angles, a constant voltage (and so constant power) is not achieved without carrier phase shift. On the other hand, finding carrier phase shift using the frequency domain to achieve constant voltage also cause a low-frequency fluctuation. Instead of using the frequency domain, it is proposed that the carrier phase-shift can be calculated for each switching period; therefore, side-bands, created by the magnitude variations of the switching harmonic over a fundamental period, are eliminated. This solution does not affect the average value, which follows the reference signal while regulating the switching harmonic.

While a carrier phase shift is introduced, a phasor sum is required to calculate the peak value of the switching harmonic. Considering (6.11), it is calculated as given in (6.13).

$$\hat{S}_{AB_{f_s}} = \frac{2}{\pi}\sqrt{\begin{array}{c} sin(\pi D_A)^2 + sin(\pi D_B)^2 \\ -2(sin(\pi D_A)(sin(\pi D_B) cos(\phi_A - \phi_B) \end{array}} \tag{6.13}$$

Concerning the phase shift between carrier signals, it is clear that the magnitude can be adjusted. However, the maximum and minimum values of the magnitude are calculated by triangle inequality, as can be found by (6.14).

$$\begin{aligned} \frac{2}{\pi}|sin(\pi D_A) - sin(\pi D_B)| < & \hat{S}_{AB_{f_s}} \\ & < \frac{2}{\pi}|sin(\pi D_A) + sin(\pi D_B)| \end{aligned} \tag{6.14}$$

The maximum and minimum values are plotted for different modulation indexes, as shown in Fig. 6.9. The maximum value over a fundamental period is decreased while increasing the modulation index, whereas the minimum value increases. At some fundamental phase angles, the maximum value becomes less than the minimum value.

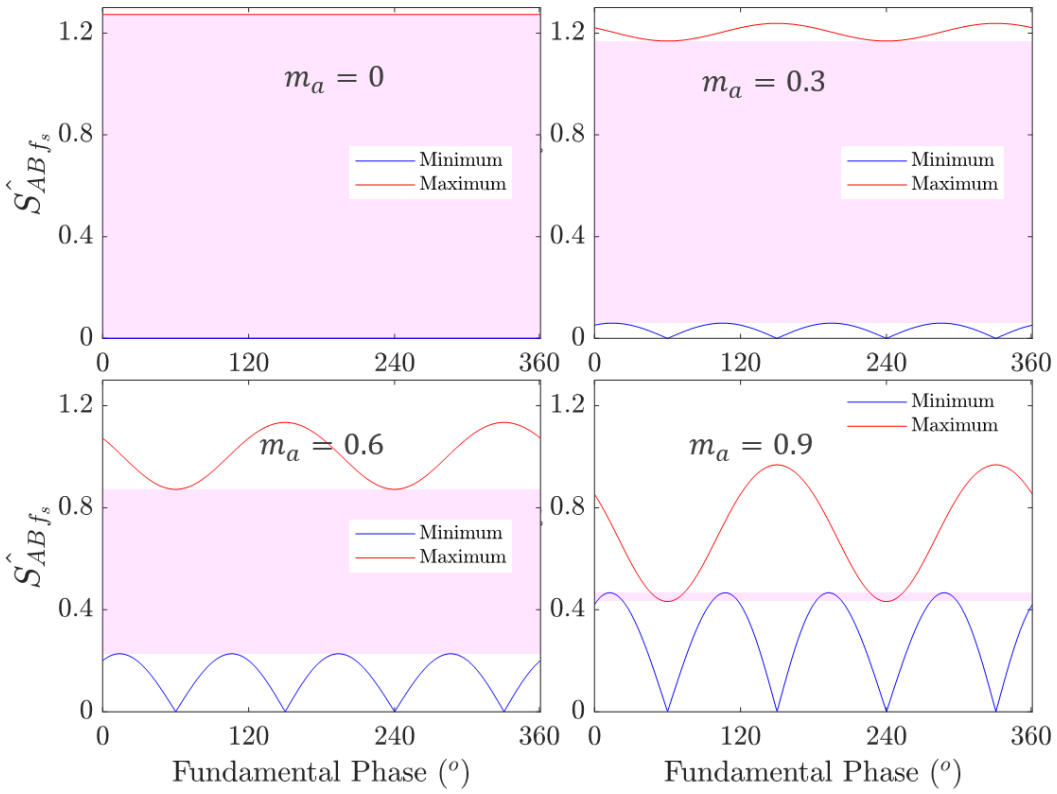

Figure 6.9: Minimum and maximum values of the magnitude of the switching frequency and allowed operating regions for different modulation indexes.

At this condition, a triangle inequality breaks down, which means that a constant value cannot be achieved over a fundamental period. The limit of the modulation index, which can give a constant voltage, is found that 0.85. Above the m_a is 0.85, the maximum value alters to the minimum value, so a constant voltage is not achieved over a fundamental period. Still, it can continue transferring desired power, but a low-frequency fluctuation exists in this condition. Thus, in order to apply the proposed system to achieve a constant voltage at the switching harmonic, the modulation index is restricted to 0.85. Although this decreases the DC-link utilization rate, conventional motor drives can also have modulation restrictions.

A WPT system is connected between phase-A and phase-B. To keep $\hat{S}_{AB_{f_s}}$ a constant value, the required carrier-phase-shit is calculated using (6.11), and found as given in (6.15).

$$\phi_{C-A} - \phi_{C-B} = acos\left[\frac{sin(\pi D_A)^2 + sin(\pi D_B)^2 - (\frac{\pi}{2}\hat{S}_{AB_{f_s}})^2}{2sin(\pi D_A)sin(\pi D_B)}\right] \tag{6.15}$$

$\hat{S}_{AB_{f_s}}$ should be selected as 0.43, which is guaranteed any modulation under 0.85. Therefore, we have a constant voltage at the switching harmonic. The proposed system does not regulate the WPT system output voltage; it just keeps the input voltage constant. If output voltage regulation is required, frequency-detuning can be used.

6.4.2 Experimental Verification

The same WPT system is used in this experimental setup, and the field current decreases to 3.3 A. The input voltage (of the WPT system) at the switching harmonic has a 0.43 (peak) gain over DC-link, which creates 30 V_{RMS}; however, the WPT system is designed for 40 V_{RMS} before. The change in the field current does not affect the proposed system's operation, but the motor's speed becomes different for the same modulation index. Firstly, m_a is brought to 0, and the carrier phase shift is given by calculating for each switching interval to give $\hat{S}_{AB_{f_s}} = 0.43$. The motor phase and field currents are shown in Fig. 6.10.a for this operating point. Then, m_a is brought to 0.3, and the carrier phase shift is updated in real-time. It was observed in Fig. 6.10.b that while the motor phase current increases, the field current stays the same. After that, m_a is brought to 0.5 as well. It was observed in Fig. 6.10.c that while the motor phase current increases, the field current stays the same. Since no speed and current controllers are established, increasing the modulation index also speeds up the motor. Thus, the fundamental frequencies at $m_a = 0.3$ and $m_a = 0.5$ are different. Moreover, as expected, the fluctuation stemming from the rectified sidebands is remarkably reduced concerning the former system. Only low-frequency ripples (with the subtracted mean value) are plotted in Fig. 6.5. The peak value decreases by the quart at $m_a = 0.5$.

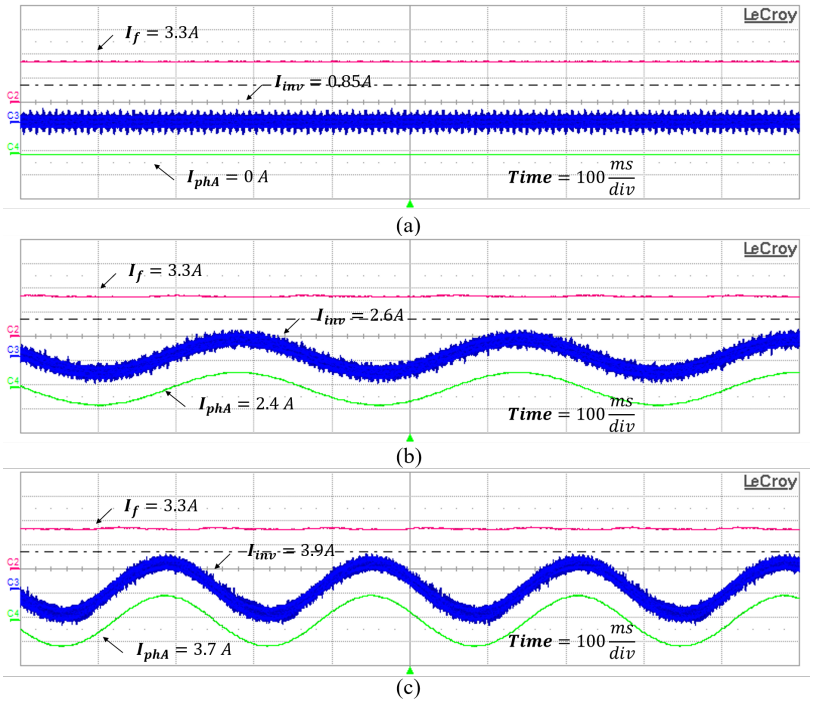

Figure 6.10: Concurrent operation of the synchronous motor's phases and field winding for different modulation index. a) $m_a = 0$ b) $m_a = 0.3$ at 200 RPM. c) $m_a = 0.5$ at 230 RPM.

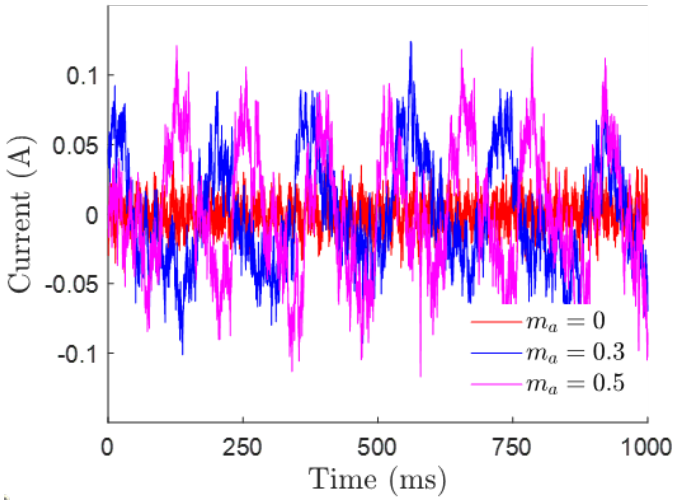

Figure 6.11: Low frequency field current fluctuations. a) $m_a = 0$ b) $m_a = 0.3$ at 200 RPM.. c) $m_a = 0.5$ at 230 RPM.

6.5 Conclusion

In this chapter, the proposed CSR was implemented with a synchronous motor drive to excite the field current. A 3-wire 3-phase GaN-based inverter was used, and an experimental setup was established where SPWM governs the motor drive with a carrier phase shift. In order to reduce the weight of the rotating frames, secondary compensation is eliminated, and the SN-WPT system is established. Firstly, the same carrier-phase-shift method explained in Chapter IV is applied; however, a low-frequency ripple is observed in the field current, which may torque ripple that is not desired. If the rotating side is wanted to be light-weight, the low-frequency ripple is not filtered out by increasing DC-link capacitance at the output. Since the low-frequency ripple stems from the sidebands, it can be eliminated during modulation. The sidebands are the magnitude fluctuation of the switching harmonic over a fundamental period. Therefore, if the magnitude of the switching harmonic is kept constant during each switching interval, the low-frequency ripple is diminished. Secondly, a real-time algorithm is developed to calculate the carrier phase shift, which brings the magnitude of the switching harmonic to the desired value and does not disturb the reference signal. However, for each modulation, the same constant value is not achieved. For SPWM, it is observed that the normalized (over DC-link voltage) magnitude of the switching harmonic is kept at 0.43 while m_a is below 0.9. The disadvantage of the proposed system is to reduce the DC-link utilization rate. The proposed CSR with the real-time algorithm is utilized to excite the field winding of WFSM, which has gained popularity with the growth of EVs and wind turbines. While the proposed system led to the constant voltage WPT system, additional frequency-detuning control is added to regulate the field current.

CHAPTER 7

CONCLUSION

In this thesis, a novel, cost-effective, and simple-to-implement CSR system is proposed. The system fits to energize rotating loads such as IoT devices, surveillance cameras, or sensors or excite the field windings of the wound-field synchronous motors. An extra high-frequency converter is not required as in conventional systems, and the converter of the motor drive is utilized as a single converter with multi-frequency outputs. Although multi-frequency approaches are studied in the literature on WPT systems, the conventional PWM techniques should govern the converter in CSR applications. The reason is that motors require dynamic and fast control, which these multi-frequency approaches could not provide. However, conventional PWM methods should be supported with an independent control parameter to concurrently control the CSR power and torque-speed of the motor. The switching frequency and carrier-phase shift are introduced as independent control parameters for DC and AC motor drives. Although an independent and concurrent power control is guaranteed using these parameters with conventional PWM techniques, other concerns, such as physical dimensions and practical implementation, should be considered. The operating frequency, or the switching frequency, directly affects the coil sizes of the WPT system. However, in conventional Si-based motor drives, the switching frequency is around 20 kHz, which makes the WPT system bulky. Recently, with the development of wide-bandgap devices, the switching frequency of the motor drives increased up to 100 kHz, so the proposed system became feasible. Consequently, the system can be applied to conventional motor drives with conventional PWM techniques, making the proposed CSR cost-efficient and simple to implement.

7.1 Implementation with DC Motor Drives

There are some considerations and consequences of implementing the proposed CSR with DC motor drives. Firstly, it is significant to use a wide-bandgap-based DC motor drive since the WPT system of the CSR becomes feasible for higher switching frequency. Secondly, the WPT system is connected in parallel to the motor and uses the switching harmonic of the motor drive. The duty cycle (or phase-shift) controls the motor's power by adjusting DC voltage. However, the duty cycle variation with required motor operations also affects the magnitude of the switching harmonic, which changes the WPT system's power. In order to achieve an independent power control of motor operations, frequency-detuning can be applied to adjust the WPT system's power. Since the switching frequency variation does not influence the motor operation, it can be used as an independent control parameter. Thus, the concurrent operation of the WPT system and motor is achieved, and they do not disturb each other operation by applying an appropriate duty cycle and switching frequency. Thirdly, transient load changes of the WPT system and motor can occur. In these conditions, it is observed that there is no change in the steady-state operation since the output of the voltage source converter is independent of loading conditions. Fourthly, connecting the WPT system in parallel to the motor affects the drive losses. Although the current of the WPT system is much less than the motor current, it creates an additional conduction loss. Besides, it also changes the switching conditions, and it is achieved that the high-frequency current can decrease the switching losses by giving rise to soft-switching. Consequently, it is deduced that the proposed CSR method is a cost-effective and simple-to-implement alternative to conventional CSRs and can be applied to conventional wide-bandgap-based DC motor drives. However, there are also a few concerns. The first concern is a restriction of duty cycles. The WPT system's power decreases to zero while the duty cycle approaches 0 or 1. Therefore, the range of duty cycles should be restricted, but it also reduces the utilization rate of the DC-link voltage. Another concern is the additional stress on the DC-link capacitance due to the high-frequency current. In order to reduce the stress, capacitor types can be altered to film or ceramic capacitors, and the capacitance can be increased.

7.2 Implementation with AC Motor Drives

There are some considerations and consequences of implementing the proposed CSR with AC motor drives. Firstly, it is significant to use a wide-bandgap-based AC motor drive since the WPT system of the CSR becomes feasible for higher switching frequency. Secondly, the WPT system is connected in parallel to the motor with any two phases (legs) of the motor drive and uses the switching harmonic of the motor drive. An SPWM (or other PWMs: SV-PWM, DPWM, etc.) controls the motor's power by adjusting fundamental frequency and magnitude. However, the magnitude of the switching harmonic varies over a fundamental period due to the SPWM. In order to control a WPT system's power independent of motor operations, a carrier phase shift is applied between motor drive phases (legs). Since the carrier phase shift does not influence the motor operation, it can be used as an independent control parameter. Thus, the concurrent operation of the WPT system and motor is achieved, and they do not disturb each other operation by applying an appropriate SPWM and carrier-phase shift. Thirdly, transient load changes of the WPT system and motor can occur. In these conditions, it is observed that there is no change in the steady-state operation since the output of the voltage source converter is independent of loading conditions. Consequently, it is deduced that the proposed CSR method is a cost-effective and simple-to-implement alternative to conventional CSRs and can be applied to conventional wide-bandgap-based AC motor drives. However, a low-frequency ripple exists in the rectified voltage of the WPT system due to the sideband harmonics. The low-frequency ripple can reveal a problem in applications such as synchronous motor's field winding excitation, where this ripple causes speed and torque fluctuation. Therefore, a novel real-time algorithm is developed to keep the switching frequency component at a constant value for each switching interval to avoid low-frequency fluctuation. In this way, the proposed CSR method utilizing the real-time algorithm can be used in WFSMs, which have become alternatives to PM machines.

7.3 Comparison with Existing Studies in the Literature and Contributions of the Proposed System

Performance comparisons of the conventional slip rings are presented in Table 7.1. Due to the maintenance requirements, the literature focuses on brushless topologies rather than slip rings. Although brushless exciters do not require regular maintenance, their size is large, which may not be feasible to place. Besides, they are inappropriate for variable speed applications since their power transfer capability changes with the rotation speed. Therefore, the trend passes to inductive and capacitive couplers. As inductive couplers, rotary transformer (RT) and inductive power transfer (IPT) systems are used. The capacitive power transfer (CPT) systems are used as capacitive couplers. Such systems require external power sources, which increases the system cost and complexity. The proposed system eliminates the external AC source using a novel multi-frequency approach with a motor drive system.

Table 7.1: The Performance Comparison of the Proposed System and Conventional Counterparts.

Performance Metrics	**Retrieved from [77]**				**The Proposed System**
	Slip Rings	**Brushless Exciters**	**Inductive Couplers**	**Capacitive Coupler**	
Maintenance	Yes	No	No	No	No
Speed Sensitivity	Yes	Possible	No	Possible	No
Scalability	Diffucult	Easy	Possible	Possible	Difficult
Power Output	DC	DC	AC	AC	AC
Power Source	External DC	Shaft	External AC	External AC	Internal AC
Size	Small	Large	Medium	Medium	Medium

Various studies of brushless systems in the literature are compared in Table 7.2. RTs are used to transfer power for small airgaps (below 1 mm), but they have some

drawbacks such as converter losses, lower switching frequencies, and bulky systems [78, 79]. CPTs are suitable to transfer power with higher frequency, and medium power requirements over an even shorter airgap [77, 21]. IPTs can be used in a broad range of air gaps between 2mm to 70mm and can provide power ratings from 10W to 3kW[20, 22, 23, 24, 69, 25, 80]. In summary, such systems have a wide range of frequency, power, airgap, and size regarding the applications, and they usually have transfer efficiencies higher than 80%. However, such systems always require an additional converter (external AC source) to create high-frequency AC excitation. In the proposed system, the main advantage is utilizing the already existing motor drive for wireless power transfer, and it is shown that the frequency, power, and air gap range are comparable with the existing studies.

Furthermore, the proposed system utilizes a new multi-frequency approach; therefore, existing multi-frequency studies for WPT systems should be compared. The multi-frequency studies are given in Table 7.3. The proposed method provides independent control of the dual-band output voltage. Unlike [42], offline calculations are not required where it is impossible to apply dynamic applications like motor drive systems. In addition, the operating frequency of the WPT system is matched with the switching frequency compared to [43, 44]. If WPT operates at the modulated frequency rather than the switching frequency, the switching losses increase to achieve the same coil sizes. Thus, directly utilizing the switching frequency is significant to make the system feasible. Furthermore, a single converter is presented rather than using two separate converters as in [41], which helps to reduce the system cost and complexity.

Table 7.3: Comparison with Existing Studies in the Literature.

	Transfer Channels	**Converter Numbers (Tx)**	**Offline Algortihm**	**Operating Frequency**
[40]	1	1	Not Required	$\geq f_s$
[41]	2	2	Not Required	f_s
[42]	2	1	Required	$\leq f_s$
[44]	4	1	Not Required	$< f_s$
This work	2	1	Not Required	$= f_s$

Table 7.2: Comparison with Existing Studies in the Literature.

	[78]	**[77]**	**[20]**	**[79]**	**[21]**	**[22]**	**[23]**	**[24]**	**[69]**	**[25]**	**[80]**	**This work**
Frequency (kHz)	5	>650	250	100	848	50	1000	50	82.6	50	585	65
Power (W)	300	340	300	1000	100	231	10	500	3000	1000	10	50
Topology	RT	CPT	IPT	RT	CPT	IPT	IPT	IPT	IPT	IPT	IPT	IPT
Airgap (mm)	0.5	0.081	18	< 2	0.125	70	2	-	10	0.6	10	10
Diameter (mm)	171	76.2	120	-	160	95	46	100	100	-	50	110
Efficiency (%)	85	85	92-95	90	94	>82	80	>80	92	>95	81	89
Additional converter	Yes	Yes	Yes	Yes	Yes	Yes	Yes	Yes	Yes	Yes	Yes	**No**

The main contributions of the proposed system to the literature are listed as follows:

- A cost-efficient and simple-to-implement contactless slip ring is introduced.
- For DC motor drives, a novel multi-frequency approach is presented to implement with a conventional DC motor PWM technique.
- A new independent control scheme, which comprises frequency and duty cycle control, is proposed for concurrent DC and high-frequency AC power transfer to the motor and rotating loads, respectively.
- For AC motor drives, a novel multi-frequency approach is presented to implement with a conventional AC motor PWM technique.
- A new independent control scheme, which comprises carrier phase shift and modulation index control, is proposed for concurrent low-frequency AC and high-frequency AC power transfer to the motor and slip rings.
- For field excitation of the synchronous motors, a new contactless slip ring is proposed, which can be integrated into the motor drive.
- A novel real-time carrier-phase-shift calculation algorithm embedded in the motor control loop is developed. Thus, the low-frequency ripple stemming from the sideband harmonics is avoided, which reduces the DC-link capacitance at the output and so the weight.

7.4 Possible Improvements and Future Works

7.4.1 Coil Design

In the coil design, there are several parameters that affect inner/outer diameters, weight, coupling factor, and losses, such as core shapes and types, coil shapes and types, turn ratio, and current density. The proposed system's coil is not optimized and is designed with a face-to-face shape using ferrite strips. However, ferrite strips and coil shapes can be optimized to achieve smaller sizes and coil losses. Besides, the coil is wound via the Litz wires to minimize eddy current losses. In order to achieve

an easy-manufacturing, PCB coils can be designed. Moreover, the system can be designed to use off-the-shelf coils, making the implementation simple.

7.4.2 Mass Reduction at the Rotating Side

In the proposed system, the SN compensation topology is used to excite the field winding. This topology requires a capacitive output filter. In order to reduce mass on the rotating frame, the capacitive output filter could be eliminated using different compensation methods, which allow inductive filtering. In this situation, an extra inductance is not required since the field winding already has a high inductance.

7.4.3 Multi-phase WPT systems

In the proposed system, the first harmonic of the switching frequency is used to excite the WPT system. The higher order harmonics can be used to achieve multi-output WPT systems. Moreover, the system is connected between two lines in AC motor drives. These connections can be changed. For example, three-phase coils of the Tx side can be utilized to increase power capability. Besides, two Tx coils can be connected to a different combination of the phases. Thus, a two-independent carrier-phase shift can be applied, and a two-output system can be achieved with independent regulations. Moreover, the connections can be used to avoid the limitation of the modulation index.

7.4.4 Analytical Modelling

In AC motor drives, frequency domain and time domain analysis are used to investigate the switching frequency and its sideband harmonics. The effect of dead-time and parasitic elements of the motor drives are ignored, and the limitation of the WPT system's input voltage can be recalculated considering the parasitic effects. Moreover, analytical modeling is developed for a single-Tx system. It can also be expanded for multi-phase WPT systems.

7.4.5 Challenge in Control Algorithms

In this thesis, open-loop DQ frame voltage references were directly given to the motor. Therefore, the speed and current of the motor are not regulated. The closed-loop speed and current control can be established in future works, and its effect on the field current can be investigated. Also, the field current was measured by a mechanical slip-ring for experimental verification. The field current can be calculated by the power factor of the motor and phase currents, or an estimation algorithm can be employed by only measuring the Tx-current.

REFERENCES

[1] J. Zhang, X. Ma, B. Cheng, and Y. Zhao, "Storage life modeling and analysis for contacting slip ring based on physics of failure," *IEEE Transactions on Components, Packaging and Manufacturing Technology*, vol. 7, no. 12, pp. 1969–1980, 2017.

[2] J. K. Nøland, F. Evestedt, J. J. Pérez-Loya, J. Abrahamsson, and U. Lundin, "Testing of active rectification topologies on a six-phase rotating brushless outer pole pm exciter," *IEEE Transactions on Energy Conversion*, vol. 33, no. 1, pp. 59–67, 2018.

[3] A. Abdolkhani, A. P. Hu, and N.-K. C. Nair, "A double stator through-hole type contactless slipring for rotary wireless power transfer applications," *IEEE Transactions on Energy Conversion*, vol. 29, no. 2, pp. 426–434, 2014.

[4] G. Peterson, "Mit witricity - not so original after all," *asme.org. http://www.tfcbooks.com/articles/witricity.htm. (accessed Sep. 12, 2022).*

[5] S. Pendharkar, "Finding the right power supply technology for your design," *edn.com. https://www.edn.com/finding-the-right-power-supply-technology-for-your-design/ (accessed Sep. 12, 2022).*

[6] G. He, Q. Chen, X. Ren, S.-C. Wong, and Z. Zhang, "Modeling and design of contactless sliprings for rotary applications," *IEEE Transactions on Industrial Electronics*, vol. 66, no. 5, pp. 4130–4140, 2019.

[7] G. Lee, H. Gwak, Y.-S. Kim, and W.-S. Park, "Wireless power transfer system for diagnostic sensor on rotating spindle," in *2013 IEEE Wireless Power Transfer (WPT)*, pp. 100–102, 2013.

[8] G. He, Q. Chen, X. Ren, S. Wong, and Z. Zhang, "Modeling and design of contactless sliprings for rotary applications," *IEEE Transactions on Industrial Electronics*, vol. 66, no. 5, pp. 4130–4140, 2019.

[9] M. Markiewicz, M. Wielgosz, M. Bocheski, W. Tabaczyski, T. Konieczny, and L. Kowalczyk, "Predictive maintenance of induction motors using ultra-low power wireless sensors and compressed recurrent neural networks," *IEEE Access*, vol. 7, pp. 178891–178902, 2019.

[10] M. Maier and N. Parspour, "Operation of an electrical excited synchronous machine by contactless energy transfer to the rotor," *IEEE Transactions on Industry Applications*, vol. 54, no. 4, pp. 3217–3225, 2018.

[11] J. K. Skjølberg, H. F. Ohma, and M. Runde, "Wear rates and current distribution of carbon brushes on steel slip rings," *IEEE Transactions on Energy Conversion*, vol. 24, no. 4, pp. 835–840, 2009.

[12] D. C. Ludois, J. K. Reed, and K. Hanson, "Capacitive power transfer for rotor field current in synchronous machines," *IEEE Transactions on Power Electronics*, vol. 27, no. 11, pp. 4638–4645, 2012.

[13] J. Dai, S. Hagen, D. C. Ludois, and I. P. Brown, "Synchronous generator brushless field excitation and voltage regulation via capacitive coupling through journal bearings," *IEEE Transactions on Industry Applications*, vol. 53, no. 4, pp. 3317–3326, 2017.

[14] R. M. J. D. J. P. F. A. Kurs, A. Karalis and M. Solijacic, "Wireless power transfer via strongly coupled magnetic resonances," *Science*, vol. 317, no. 5834, pp. 83–86, 2007.

[15] S. Hui and W. Ho, "A new generation of universal contactless battery charging platform for portable consumer electronic equipment," in *2004 IEEE 35th Annual Power Electronics Specialists Conference (IEEE Cat. No.04CH37551)*, vol. 1, pp. 638–644 Vol.1, 2004.

[16] O. Knecht, R. Bosshard, and J. W. Kolar, "High-efficiency transcutaneous energy transfer for implantable mechanical heart support systems," *IEEE Transactions on Power Electronics*, vol. 30, no. 11, pp. 6221–6236, 2015.

[17] D. Patil, M. K. McDonough, J. M. Miller, B. Fahimi, and P. T. Balsara, "Wireless power transfer for vehicular applications: Overview and challenges," *IEEE Transactions on Transportation Electrification*, vol. 4, no. 1, pp. 3–37, 2018.

[18] Y. Jang and M. Jovanovic, "A contactless electrical energy transmission system for portable-telephone battery chargers," in *INTELEC. Twenty-Second International Telecommunications Energy Conference (Cat. No.00CH37131)*, pp. 726–732, 2000.

[19] M. Etemadrezaei, "22 - wireless power transfer," in *Power Electronics Handbook (Fourth Edition)* (M. H. Rashid, ed.), pp. 711–722, Butterworth-Heinemann, fourth edition ed., 2018.

[20] D. Maier, J. Kurz, and N. Parspour, "Contactless energy transfer for inductive electrically excited synchronous machines," in *2019 IEEE PELS Workshop on Emerging Technologies: Wireless Power Transfer (WoW)*, pp. 191–195, 2019.

[21] D. C. Ludois, M. J. Erickson, and J. K. Reed, "Aerodynamic fluid bearings for translational and rotating capacitors in noncontact capacitive power transfer systems," *IEEE Transactions on Industry Applications*, vol. 50, no. 2, pp. 1025–1033, 2014.

[22] W. Zhou, "Design and analysis of decoupled tetra-polar ring-coils for wireless power transfer in rotary mechanism applications," *IET Electric Power Applications*, vol. 14, pp. 1766–1773(7), October 2020.

[23] L. Sun, J. Kang, Y. Liu, Z. Mao, and Z. Zhong, "Wireless power transfer based contactless excitation of electrically excited synchronous motor," in *2020 IEEE 9th International Power Electronics and Motion Control Conference (IPEMC2020-ECCE Asia)*, pp. 1091–1097, 2020.

[24] X. Feng, Z. Fu, G. Hao, K. Wang, and Y. Weng, "Modeling and implementation of a new non-contact slip ring for wireless power transfer," in *2020 IEEE 9th International Power Electronics and Motion Control Conference (IPEMC2020-ECCE Asia)*, pp. 106–111, 2020.

[25] R. Trevisan and A. Costanzo, "A 1-kw contactless energy transfer system based on a rotary transformer for sealing rollers," *IEEE Transactions on Industrial Electronics*, vol. 61, no. 11, pp. 6337–6345, 2014.

[26] H. Polat, E. Ayaz, O. Altun, and O. Keysan, "Balancing of common dc-bus parallel-connected modular inductive power transfer systems," *IEEE Journal of*

Emerging and Selected Topics in Power Electronics, vol. 10, no. 2, pp. 1587–1596, 2022.

[27] H. Hao, G. A. Covic, and J. T. Boys, "A parallel topology for inductive power transfer power supplies," *IEEE Transactions on Power Electronics*, vol. 29, no. 3, pp. 1140–1151, 2014.

[28] H. H. Wu, A. Gilchrist, K. D. Sealy, and D. Bronson, "A high efficiency 5 kw inductive charger for evs using dual side control," *IEEE Transactions on Industrial Informatics*, vol. 8, no. 3, pp. 585–595, 2012.

[29] Y. H. Sohn, B. H. Choi, E. S. Lee, G. C. Lim, G. Cho, and C. T. Rim, "General unified analyses of two-capacitor inductive power transfer systems: Equivalence of current-source ss and sp compensations," *IEEE Transactions on Power Electronics*, vol. 30, no. 11, pp. 6030–6045, 2015.

[30] J. Zeng, G. Zhang, S. S. Yu, B. Zhang, and Y. Zhang, "Llc resonant converter topologies and industrial applications a review," *Chinese Journal of Electrical Engineering*, vol. 6, no. 3, pp. 73–84, 2020.

[31] X. Qu, H. Chu, S. Wong, and C. K. Tse, "An ipt battery charger with near unity power factor and load-independent constant output combating design constraints of input voltage and transformer parameters," *IEEE Transactions on Power Electronics*, vol. 34, no. 8, pp. 7719–7727, 2019.

[32] Y. Wang, M. Wang, and D. Lin, "The duality of inductive power transfer and capacitive power transfer," in *2020 8th International Conference on Power Electronics Systems and Applications (PESA)*, pp. 1–5, 2020.

[33] T. W. Ching and Y. S. Wong, "Review of wireless charging technologies for electric vehicles," in *2013 5th International Conference on Power Electronics Systems and Applications(PESA)*, pp. 1–4, 2013.

[34] V. Shevchenko, O. Husev, R. Strzelecki, B. Pakhaliuk, N. Poliakov, and N. Strzelecka, "Compensation topologies in ipt systems: Standards, requirements, classification, analysis, comparison and application," *IEEE Access*, vol. 7, pp. 120559–120580, 2019.

[35] A. Safaee and K. Woronowicz, "Time-domain analysis of voltage-driven seriesseries compensated inductive power transfer topology," *IEEE Transactions on Power Electronics*, vol. 32, no. 7, pp. 4981–5003, 2017.

[36] L. H. Chan, Y. Yang, and K.-W. E. Cheng, "Comparative studies on the primary-side frequency and phase shift control for series-series compensated inductive power transfer," in *2020 8th International Conference on Power Electronics Systems and Applications (PESA)*, pp. 1–5, 2020.

[37] C.-S. Wang, G. Covic, and O. Stielau, "Power transfer capability and bifurcation phenomena of loosely coupled inductive power transfer systems," *IEEE Transactions on Industrial Electronics*, vol. 51, no. 1, pp. 148–157, 2004.

[38] K. Aditya and S. S. Williamson, "Design guidelines to avoid bifurcation in a seriesseries compensated inductive power transfer system," *IEEE Transactions on Industrial Electronics*, vol. 66, no. 5, pp. 3973–3982, 2019.

[39] J. Liu, Q. Deng, D. Czarkowski, M. K. Kazimierczuk, H. Zhou, and W. Hu, "Frequency optimization for inductive power transfer based on ac resistance evaluation in litz-wire coil," *IEEE Transactions on Power Electronics*, vol. 34, no. 3, pp. 2355–2363, 2019.

[40] Z. Pantic, K. Lee, and S. M. Lukic, "Multifrequency inductive power transfer," *IEEE Transactions on Power Electronics*, vol. 29, no. 11, pp. 5995–6005, 2014.

[41] D. Ahn and P. P. Mercier, "Wireless power transfer with concurrent 200-khz and 6.78-mhz operation in a single-transmitter device," *IEEE Transactions on Power Electronics*, vol. 31, no. 7, pp. 5018–5029, 2016.

[42] C. Zhao and D. Costinett, "Gan-based dual-mode wireless power transfer using multifrequency programmed pulse width modulation," *IEEE Transactions on Industrial Electronics*, vol. 64, no. 11, pp. 9165–9176, 2017.

[43] C. Xia, N. Wei, H. Zhang, S. Zhao, Z. Li, and Z. Liao, "Multifrequency and multiload mcr-wpt system using hybrid modulation waves spwm control method," *IEEE Transactions on Power Electronics*, vol. 36, no. 11, pp. 12400–12412, 2021.

[44] J. Wu, L. Bie, W. Kong, P. Gao, and Y. Wang, "Multi-frequency multi-amplitude superposition modulation method with phase shift optimization for single inverter of wireless power transfer system," *IEEE Transactions on Circuits and Systems I: Regular Papers*, vol. 68, no. 5, pp. 2271–2279, 2021.

[45] Y. Cao and J. A. A. Qahouq, "Analysis and evaluation of a dual-variable closed-loop control of power converter with wireless and nonwireless power transfer," *IEEE Transactions on Industrial Electronics*, vol. 66, no. 4, pp. 2668–2679, 2019.

[46] Q. Deng, Y. Cheng, F. Chen, D. Czarkowski, M. K. Kazimierczuk, H. Zhou, and W. Hu, "Wired/wireless hybrid charging system for electrical vehicles with minimum rated power requirement for dc module," *IEEE Transactions on Vehicular Technology*, vol. 69, no. 10, pp. 10889–10898, 2020.

[47] M. R. Barzegaran, H. Zargarzadeh, and O. A. Mohammed, "Wireless power transfer for electric vehicle using an adaptive robot," *IEEE Transactions on Magnetics*, vol. 53, no. 6, pp. 1–4, 2017.

[48] H. Polat, E. Ayaz, O. Altun, and O. Keysan, "Fault tolerant modular inductive power transfer system design using resonator coil," *TechRxiv. Preprint. https://doi.org/10.36227/techrxiv.14370617.v1*, Apr 2021.

[49] P. Tomaszuk, A. ukowska, M. Reko, and K. Dzicrzck, "Integrated drive system of robotic arm joint used in a mobile robot," in *2018 23rd International Conference on Methods Models in Automation Robotics (MMAR)*, pp. 509–514, 2018.

[50] Y.-S. Lai, W.-T. Lee, Y.-K. Lin, and J.-F. Tsai, "Integrated inverter/converter circuit and control technique of motor drives with dual-mode control for ev/hev applications," *IEEE Transactions on Power Electronics*, vol. 29, no. 3, pp. 1358–1365, 2014.

[51] R. Nair and G. Narayanan, "Emulation of wind turbine system using vector controlled induction motor drive," *IEEE Transactions on Industry Applications*, vol. 56, no. 4, pp. 4124–4133, 2020.

[52] R. A. Torres, H. Dai, W. Lee, T. M. Jahns, and B. Sarlioglu, "Current-source inverters for integrated motor drives using wide-bandgap power switches," in *2018 IEEE Transportation Electrification Conference and Expo (ITEC)*, pp. 1002–1008, 2018.

[53] I. Okoro and C. Enwerem, "Model-based speed control of a dc motor using a combined control scheme," in *2019 IEEE PES/IAS PowerAfrica*, pp. 1–6, 2019.

[54] K. Saad, K. Abdellah, and T. B. Ali, "Advanced fault-tolerant control of multiphase induction motor drives in ev," in *2019 1st International Conference on Sustainable Renewable Energy Systems and Applications (ICSRESA)*, pp. 1–5, 2019.

[55] H. Liu, L. Xu, M. Shangguan, and W. N. Fu, "Finite element analysis of 1 mw high speed wound-rotor synchronous machine," *IEEE Transactions on Magnetics*, vol. 48, no. 11, pp. 4650–4653, 2012.

[56] X. Lu, C. Rogers, and F. Z. Peng, "A double fourier analysis development of thd for pwm inverters: A theoretical method for motor loss minimization," in *2010 IEEE Energy Conversion Congress and Exposition*, pp. 1505–1510, 2010.

[57] A. Hava, R. Kerkman, and T. Lipo, "A high-performance generalized discontinuous pwm algorithm," *IEEE Transactions on Industry Applications*, vol. 34, no. 5, pp. 1059–1071, 1998.

[58] S. Tiwari, O. . Midtgård, and T. M. Undeland, "Sic mosfets for future motor drive applications," in *2016 18th European Conference on Power Electronics and Applications (EPE'16 ECCE Europe)*, pp. 1–10, 2016.

[59] V. Shevchenko, O. Husev, R. Strzelecki, B. Pakhaliuk, N. Poliakov, and N. Strzelecka, "Compensation topologies in ipt systems: Standards, requirements, classification, analysis, comparison and application," *IEEE Access*, vol. 7, pp. 120559–120580, 2019.

[60] A. K. Morya, M. C. Gardner, B. Anvari, L. Liu, A. G. Yepes, J. Doval-Gandoy, and H. A. Toliyat, "Wide bandgap devices in ac electric drives: Opportunities and challenges," *IEEE Transactions on Transportation Electrification*, vol. 5, no. 1, pp. 3–20, 2019.

[61] W. Lee, S. Li, D. Han, B. Sarlioglu, T. A. Minav, and M. Pietola, "A review of integrated motor drive and wide-bandgap power electronics for high-performance electro-hydrostatic actuators," *IEEE Transactions on Transportation Electrification*, vol. 4, no. 3, pp. 684–693, 2018.

[62] E. A. Jones, F. F. Wang, and D. Costinett, "Review of commercial gan power devices and gan-based converter design challenges," *IEEE Journal of Emerging and Selected Topics in Power Electronics*, vol. 4, no. 3, pp. 707–719, 2016.

[63] F. Karakaya, O. S. Alemdar, and O. Keysan, "Layout Based Ultra-Fast Short-Circuit Protection Technique for Parallel Connected GaN HEMTs," *IEEE Journal of Emerging and Selected Topics in Power Electronics*, pp. 1–1, 2021.

[64] G. A. Covic and J. T. Boys, "Modern trends in inductive power transfer for transportation applications," *IEEE Journal of Emerging and Selected Topics in Power Electronics*, vol. 1, no. 1, pp. 28–41, 2013.

[65] M. Budhia, J. T. Boys, G. A. Covic, and C.-Y. Huang, "Development of a single-sided flux magnetic coupler for electric vehicle ipt charging systems," *IEEE Transactions on Industrial Electronics*, vol. 60, no. 1, pp. 318–328, 2013.

[66] S. Y. Choi, J. Huh, W. Y. Lee, and C. T. Rim, "Asymmetric coil sets for wireless stationary ev chargers with large lateral tolerance by dominant field analysis," *IEEE Transactions on Power Electronics*, vol. 29, no. 12, pp. 6406–6420, 2014.

[67] Z. Zhang and K. T. Chau, "Homogeneous wireless power transfer for move-and-charge," *IEEE Transactions on Power Electronics*, vol. 30, no. 11, pp. 6213–6220, 2015.

[68] A. Zaheer, G. A. Covic, and D. Kacprzak, "A bipolar pad in a 10-khz 300-w distributed ipt system for agv applications," *IEEE Transactions on Industrial Electronics*, vol. 61, no. 7, pp. 3288–3301, 2014.

[69] K. Song, B. Ma, G. Yang, J. Jiang, R. Wei, H. Zhang, and C. Zhu, "A rotation-lightweight wireless power transfer system for solar wing driving," *IEEE Transactions on Power Electronics*, vol. 34, no. 9, pp. 8816–8830, 2019.

[70] A. H. A. Abdolkhani and N. Nair, "Modelling and parameters identification of through-hole type wind turbine contactless sliprings," *Scientific Research Engineering*, vol. 4, no. 5, pp. 272–283, 2012.

[71] D. Christen, U. Badstuebner, J. Biela, and J. W. Kolar, "Calorimetric power loss measurement for highly efficient converters," in *The 2010 International Power Electronics Conference - ECCE ASIA -*, pp. 1438–1445, 2010.

[72] A. Naina, S. Paryani, and S. S. N. Jani, "Comparison between surface-mounted and interior pm motor for ev application," in *2021 International Conference on Intelligent Technologies (CONIT)*, pp. 1–6, 2021.

[73] D. G. Dorrell, "Are wound-rotor synchronous motors suitable for use in high efficiency torque-dense automotive drives?," in *IECON 2012 - 38th Annual Conference on IEEE Industrial Electronics Society*, pp. 4880–4885, 2012.

[74] I. Boldea, L. N. Tutelea, L. Parsa, and D. Dorrell, "Automotive electric propulsion systems with reduced or no permanent magnets: An overview," *IEEE Transactions on Industrial Electronics*, vol. 61, no. 10, pp. 5696–5711, 2014.

[75] F. Graffeo, S. Vaschetto, M. Cossale, M. Kerschbaumer, E. C. Bortoni, and A. Cavagnino, "Cylindrical wound-rotor synchronous machines for traction applications," in *2020 International Conference on Electrical Machines (ICEM)*, vol. 1, pp. 1736–1742, 2020.

[76] A. Di Gioia, I. P. Brown, Y. Nie, R. Knippel, D. C. Ludois, J. Dai, S. Hagen, and C. Alteheld, "Design and demonstration of a wound field synchronous machine for electric vehicle traction with brushless capacitive field excitation," *IEEE Transactions on Industry Applications*, vol. 54, no. 2, pp. 1390–1403, 2018.

[77] J. Dai, S. Hagen, D. C. Ludois, and I. P. Brown, "Synchronous generator brushless field excitation and voltage regulation via capacitive coupling through journal bearings," *IEEE Transactions on Industry Applications*, vol. 53, no. 4, pp. 3317–3326, 2017.

[78] J.-N. Weber, A. Rehfeldt, S.-A. Vip, and B. Ponick, "Rotary transformer with electrical steel core for brushless excitation of synchronous machines," in *2016*

XXII International Conference on Electrical Machines (ICEM), pp. 884–889, 2016.

[79] K. D. Papastergiou and D. E. Macpherson, "An airborne radar power supply with contactless transfer of energypart i: Rotating transformer," *IEEE Transactions on Industrial Electronics*, vol. 54, no. 5, pp. 2874–2884, 2007.

[80] C. Zhang, D. Lin, and S. Y. R. Hui, "Ball-joint wireless power transfer systems," *IEEE Transactions on Power Electronics*, vol. 33, no. 1, pp. 65–72, 2018.

APPENDIX A

LIST OF PUBLICATIONS

- E. Ayaz, O. Altun, H. Polat, F. Karakaya and O. Keysan, "Concurrent Wireless Power Transfer and Motor Drive System With a Single Converter," in IEEE Journal of Emerging and Selected Topics in Industrial Electronics, 2022, doi: 10.1109/JESTIE.2022.3182592.

- E. Ayaz, O. Altun, H. Polat and O. Keysan, "Generalized Model of Modular Two Element Compensated IPT Systems with Common DC-Bus," 2022 Wireless Power Week (WPW), 2022, pp. 260-265,
  doi: 10.1109/WPW54272.2022.9853857.

- E. Ayaz, O. Altun, and O. Keysan, "Carrier Phase Shift Method of SPWM for Concurrent Wired and Wireless Power Transfer Systems," Submitted to IEEE Transactions on Industrial Electronics, Under revision.

- E. Ayaz, O. Altun, H. Polat, and O. Keysan, Fault tolerant multi-tx/multi-rx inductive power transfer system with a resonator coil, Submitted to IEEE Journal of Emerging and Selected Topics in Power Electronics, Under revision.